Dipl.-Ing. Christian Pock, Bakk.techn.

Low Earth Orbit Determination for GNSS Radio Occultation with Aspects of Uncertainty Estimation

MASTER'S THESIS

to achieve the university degree of

Diplom-Ingenieur

Master's degree programme: Space Sciences and Earth from Space

submitted to

Graz University of Technology

Supervised by:

Univ.-Prof. Mag. Dr.rer.nat. Gottfried Kirchengast

Uni Graz - Wegener Center for Climate and Global Change

Univ.-Prof. Dr.-Ing. Torsten Mayer-Gürr

TU Graz - Institute of Geodesy

Graz, April 2015

Affidavit

I declare that I have authored this thesis independently, that I have not used other than the declared sources/resources, and that I have explicitly indicated all material which has been quoted either literally or by content from the sources used. The text document uploaded to TUGRAZonline is identical to the present master's thesis.

Graz, _____ _____

Date Signature

Danksagung

Ein herzliches Dankeschön an alle, die mich bei der Erstellung dieser Masterarbeit unterstützt haben. Insbesondere möchte ich mich bei meinen beiden Betreuern, Herrn Univ.-Prof. Mag. Dr.rer.nat. Gottfried Kirchengast und Herrn Univ.-Prof. Dr.-Ing. Torsten Mayer-Gürr, bedanken, die stets ein offenes Ohr für meine Fragen und Anliegen hatten und diese universitätsübergreifende Masterarbeit erst ermöglicht haben.

Mein weiterer Dank gilt auch Herrn Dipl.-Ing. Norbert Zehentner, der mir des Öfteren mit seiner Expertise im Bereich der präzisen Orbitbestimmung weiterhelfen konnte.

Ebenfalls erwähnen möchte ich, dass diese Arbeit durch ein Stipendium aus Mitteln des ASAP-9 Projekts OPSCLIMPROP der österreichischen Forschungsförderungsgesellschaft (FFG) unterstützt wurde.

Abstract

This inter-university research between Graz University of Technology and the University of Graz in the frame of NAWI Graz focuses in the first part on a precise orbit determination of Low Earth Orbiting (LEO) satellites. These LEO satellites, namely CHAMP, GRACE-A, FORMOSAT-3/COSMIC and MetOp-A, are very important for various scientific disciplines. In geodesy, for example, these missions are required for highly accurate measurements of the global Earth's gravity field.

In the context of this thesis, these satellite missions are finally used for the GNSS-radio occultation method, which is closely connected to climate research. This method is based on propagating radio signals through the atmosphere. These signals are emitted from GNSS satellites and received by LEOs. Due to the varying atmospheric density, this affects the radio signal and a phase path extension as a function of time occurs. Based on these measurements, other climate relevant parameters such as refractivity and temperature can be determined. To compute the atmospheric excess phase, highly accurate LEO positions and velocities are needed. Therefore, the required processing strategy has to ensure excellent orbit quality independent of the specified LEO mission. This goal has been achieved. An independent validation with data from the established analysis centers CODE, JPL, UCAR and EUMETSAT shows highly consistent results.

The second part of the thesis deals with the issue of position and velocity uncertainty. This includes both the LEO and the GNSS satellites. It is very difficult to quantify these uncertainties because usually the real orbit is unknown. Nevertheless, some ideas are collected to capture the uncertainty. This includes for example how uncertainties of the orbit positions are affecting the satellite velocity. The thesis is rounded off by some investigation concerning different observation intervals, input data and different processing length and is going to serve as pilot study for the upcoming radio occultation excess phase processing at the Wegener Center for Climate and Global Change.

Zusammenfassung

Diese universitätsübergreifende Arbeit zwischen der Technischen Universität Graz und der Universität Graz im Rahmen von NAWI Graz befasst sich im esten Teil mit der präzisen Bahnbestimmung von niedrig fliegenden Satelliten. Die LEO (Low Earth Orbiter) Satelliten wie CHAMP, GRACE-A, FORMOSAT-3/COSMIC und MetOp-A sind für verschiedene Wissenschaftsdisziplinen enorm wichtig. Im Bereich der Geodäsie beispielsweise werden diese Missionen für die hochgenaue Vermessung des globalen Erdschwerefeldes benötigt.

Im Rahmen dieser Masterarbeit wurden diese Satellitenmissionen vor dem Hintergrund der Klimaforschung und hier im speziellen der GNSS-Radio-Okkultation beleuchtet. Bei dieser Methode wird unter Verwendung von sich durch die Atmosphäre ausbreitenden Radiosignalen emittiert von GNSS-Satelliten und empfangen von LEO Satelliten die Phasenwegsverlängerung als Funktion der Zeit bestimmt. Diese ergibt sich durch die variierende atmosphärische Dichte, die das Radiosignal beeinflusst. Aufbauend auf diesen Messungen können weitere klimarelevante Kenngrößen wie beispielsweise Refraktivität und Temperatur bestimmt werden. Zur Bestimmung der Phasenwegsverlängerung werden hoch präzise LEO Positionen und Geschwindigkeiten benötigt. Die dafür nötige Prozessierungsstrategie soll eine kontinuierliche und hochgenaue Orbitqualität, unabhängig von der gewählten LEO Satellitenmission gewährleisten. Dieses Ziel konnte erreicht werden, da eine unabhängige Validierung mit Daten von etablierten Analysezentren wie CODE, JPL, UCAR und EUMETSAT eine hohe Konsistenz der erzielten Resultate zeigte.

Der zweite Teil der Arbeit beschäftigt sich mit der Frage der Unsicherheit der berechneten Satellitenpositionen und Geschwindigkeiten. Dies umfasst sowohl die LEO als auch die GNSS Satelliten. Diese Unsicherheiten zu quantifizieren ist sehr schwierig, da der wahre, fehlerfreie Orbit nicht bekannt ist. Nichtsdestotrotz wurden einige Ideen dazu entwickelt, wie sich beispielsweise Unsicherheiten in den Orbitpositionen auf die Geschwindigkeit auswirken können. Abgerundet wird diese Masterarbeit von einigen Untersuchungen hinsichtlich der Wahl verschiedener Beobachtungsintervalle, Inputdaten oder unterschiedlicher Prozessierungsdauer, da diese Arbeit auch als Pilotstudie für die neue GNSS-RO Prozessierungskette am Wegener Center für Klima und Globalen Wandel dient.

Abbreviations

ASC Advanced Stellar Compass

ASAP Austrian Space Applications Programme

AC Analysis Center

AAR14 Austrian Assessment Report 2014

AIUB Astronomical Institute University of Bern

BPE Bernese Processing Engine

CODE Center for Orbit Determination in Europe

DCB Differential Code Bias

ESA European Space Agency

ERP Earth Rotation Parameter

EUMETSAT European Org. for the Exploitation of Meteorological Satellites

FTR GNSS-RO Fast Track Reference

GUI Graphical User Interface

GPS Global Positioning System

GRAS Global Navigation Satellite System Receiver for Atmospheric Sounding

GNSS Global Navigation Satellite System

GFZ Geo Forschungs Zentrum Potsdam

IGOR Integrated GPS Occultation Receiver

IGS International GNSS Service

IPCC Intergovernmental Panel of Climate Change

CRF Celestial Reference Frame

TRF Terrestrial Reference Frame

ITSG Working Group of Theoretical Geodesy and Satellite Geodesy

IERS International Earth Rotation and Reference Systems Service

JPL Jet Propulsion Laboratory

LEO Low Earth Orbiter

MEO Medium Earth Orbiter

NASA National Aeronautics and Space Administration

NetCDF Network Common Data Format

OPSCLIMPROP Occultation Processing System for Cal/Val and Climate

PCF Process Control File

PTR GNSS-RO Post Track Reference Processing

PRN Pseudo Random Noise

POD Precise Orbit Determination

PCO Phase Center Offset

PCV Phase Center Variation

RD Reduced Dynamic

RO Radio Occultation

rOPS Reference Occultation Processing System

RPR GNSS-RO Re-Processing Reference Track

RMS Root Mean Squares

RINEX Receiver INdependent EXchange Format

SLR Satellite Laser Ranging

SCA Star Camera Assembly

SCS Satellite Coordinate System

SP3 Standard Product 3 Orbit Format

SST Satellite to Satellite Tracking

TAI Temps Atomique International

TOD True of Date

UCAR University Corporation for Atmospheric Research

WGS World Geodetic System

Contents

1 Introduction

GNSS antennas and receivers aboard the LEO satellites provide the possibility for Precise Orbit Determination (POD). This application is important for many scientific disciplines. In geodesy precise orbits are used for the estimation of time variable gravity fields which help to understand the global water cycle and the impact of mass transport on the gravity field. Related to this work, the satellite orbits are deployed within climate research and climatology. Here, they are needed for the computation of the excess phase using the GNSS Radio Occultation (GNSS-RO) technique.

This work is a pilot study and will help to compute orbits and excess phase data within the upcoming orbit and excess phase processing chain of the new Reference Occultation Processing System (rOPS) at the Wegener Center for Climate and Global Change. Currently, orbit and excess phase data provided by external analysis centers are used by the Wegener Center. The order of this introduction is to first highlight a few aspects of the study, afterwards to summarize the research goals (sec. 1.1), and finally provide an overview on the contents of the thesis (sec. 1.2), which is collected in six main chapters (chap. 2 to chap. 7).

To ensure a good basis for the orbit computation LEOs are able to collect extremely precise GNSS measurements with a dense global coverage. For the orbit computation, several techniques have been developed during the last decades which nowadays makes continuous sub-dm orbit computation feasible. The two basic methods of kinematic and reduced-dynamic orbit computation are chosen within this research. On the one hand, the kinematic method can be seen as the pure geometrical approach whereas on the other hand, the reduced-dynamic method is a combination of the GNSS measurements with the introduced dynamic force models.

Due to the very precise GNSS orbit and clock data available these days, all observations are used in a zero-difference mode. Nevertheless, the ionosphere free linear combination is needed to eliminate the atmospheric error source. In order to incorporate only GNSS data of excellent quality, the data screening process is very important. Outliers, data gaps, jumps and cycle slips should be detected in the

carrier phase measurements and fixed before further use of the data. Afterwards, the orbit computation is carried out based on clean data. Note that within this study only GPS data is used.

Another aspect of this work is the orbit uncertainty. This includes the uncertainty coming from the GNSS data as well as the uncertainty from the LEO positions and velocities. In general, it is very difficult to quantify the orbit accuracy because the real orbit is usually not known. Some ideas of capturing the orbit uncertainty nonetheless are presented in this work.

1.1 Goals of the Research

The primary goal of the POD part is to provide orbit position and velocity data on the same or on a better accuracy level compared to the established analysis centers CODE, JPL, UCAR, and EUMETSAT. Another task is to discover possible vulnerabilities in the POD processing chains and provide a stable basis for the 50 Hz GNSS-RO event orbit arc interpolation. In addition, several sensitivity investigations have been carried out. These investigations concern in particular

- Use of different sources of GNSS input data,
- Effect of different sampling rates of GNSS clock data,
- Different processing length and edge effect at the 24h-day transitions,
- Varying LEO navigation tracking data sampling rates,
- Impact of different sampling periods of stochastic parameters,
- Evaluation of different aspects of orbit uncertainty.

The validation of the results with independent data provided by established analysis centers is also part of this work. To achieve competitive results, a proper processing strategy has been developed and this strategy is required to be independent from the specified LEO mission.

1.2 General Overview

This thesis has been carried out in a cooperation of the Institute of Geodesy (TU Graz) and the Wegener Center of Climate and Global Change (Uni Graz) in the frame of NAWI Graz.

In chapter 2 **Investigated Low Earth Orbit Missions**, the focus is on the presentation of the LEO satellites, CHAMP, GRACE-A, FORMOSAT-3/COSMIC, and MetOp-A, and the concept of satellite-to-satellite tracking in high-low mode. The characteristics of the different receivers aboard the satellites are presented, too.

In chapter 3 **Fundamentals of the Global Positioning System**, the basics of the GPS system as one of the GNSS systems are described. This includes the mathematical concept of GPS observations as well as several techniques for building linear combinations of the dual-frequency carrier phase measurements. Furthermore, an overview of the different data provider and analysis centers is given.

In chapter 4 **GNSS Radio Occultation**, the GNSS-RO atmosphere sounding technique is described in more detail. This includes the excess phase computation and the bending angles derived from it. The chapter closes with an overview of the real life impact of climate products.

Chapter 5 **Precise Orbit Determination for Low Earth Orbit Satellites** describes the main part of this work. In a first step, the mathematical concept of least squares adjustment as the backbone of the orbit computation is described. Afterwards, the different types of orbits and force models are presented in more detail. Finally, the processing chain established through this study is shown.

Chapter 6 **Aspects of Orbit Uncertainty Estimation** presents some ideas of quantifying orbit uncertainty. As one of these ideas, the uncertainty from GNSS orbit and clock data is separated from the LEO orbit and clock uncertainty. In general, orbit uncertainty is difficult to quantify. This chapter collects some avenues of capturing the uncertainty nevertheless.

Chapter 7 **Orbit Calculation and Results** demonstrates the capability of the chosen POD processing strategy. Orbit position and velocity data from independent analysis centers are used to validate the quality of the results. The outcome of several sensitivity investigations is presented, too. Finally, the bridge from the computed orbits to the GNSS-RO orbit arcs during occultation events is built.

Conclusion and Outlook finally sum up the achieved results and give perspectives on future work.

2 Investigated Low Earth Orbit Missions

The Low Earth Orbiter (LEO) space segment is defined by satellites with orbit heights below 2.000 km *(Hofmann-Wellenhof et al, 2008)*. This is the typical height of scientific Earth observing satellites. Beyond 2.000 km, up to 36.000 km Medium Earth Orbiters (MEOs) are operating. The Global Positioning System (GPS) is part of these MEOs as well as other Global Navigation Satellite Systems (GNSS) like GLONASS, Galileo or Beidou. LEO satellites are equipped with high rate GNSS receivers which enables them to track GNSS signals. This makes satellite-to-satellite tracking (SST) possible. In Fig. 2.1, the SST concept is shown.

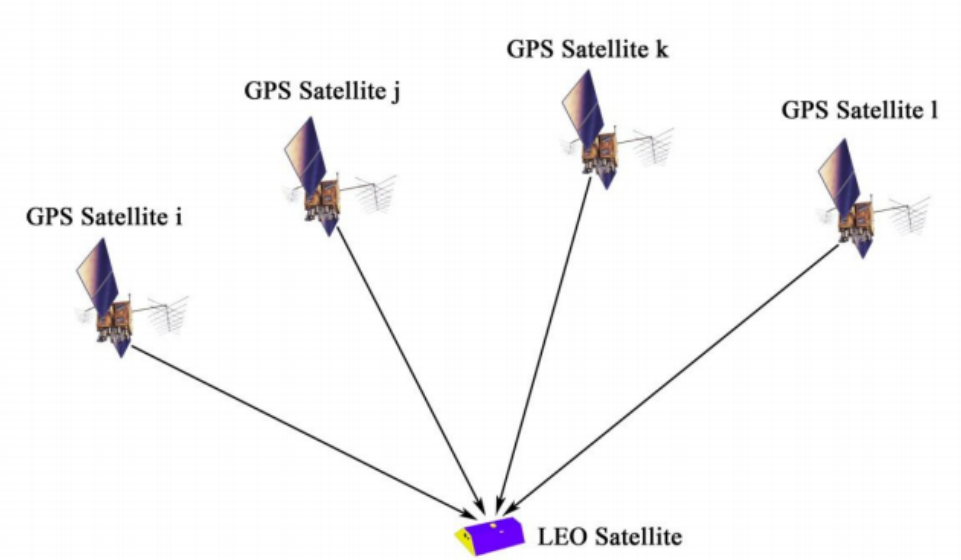

Figure 2.1: *Concept of SST tracking (Swatschina, 2012)*

The possibility to make use of the GNSS for orbit determination was demonstrated for the first time in 1984 on the example of the LANDSAT-4 satellite *(Jäggi, 2007)*. Since then a step-by-step progress in technology has taken place. For the geodetic research and for the climate community, high precise orbit products are of essential interest. Hence, POD and all products belonging to it have become important in the recent past. This thesis focuses on four prominent scientific satellite missions (CHAMP, GRACE, FORMOSAT-3/COSMIC and MetOp-A). These missions are now presented in more detail.

2.1 CHAMP

The German satellite mission CHAllenging Minisatellite Payload (CHAMP) *(Reigber et al, 1999)* was operated by the Geo Forschungs Zentrum (GFZ) Potsdam and was launched on July 15th, 2000 from Plesetsk, Russia into a polar-like orbit. After 10 years of operating, the satellite re-entered Earth atmosphere on September 19th, 2010 and completed its successful mission. The spacecraft was equipped with various highly accurate scientific instruments *(Reigber et al, 2002)*, shown in Fig. 2.2 and 2.3.

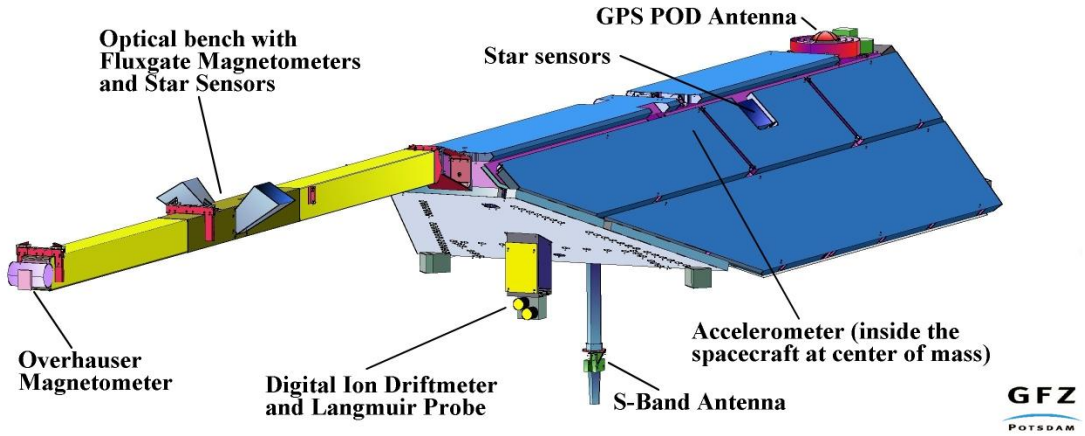

Figure 2.2: *CHAMP front side (courtesy of GFZ Potsdam)*

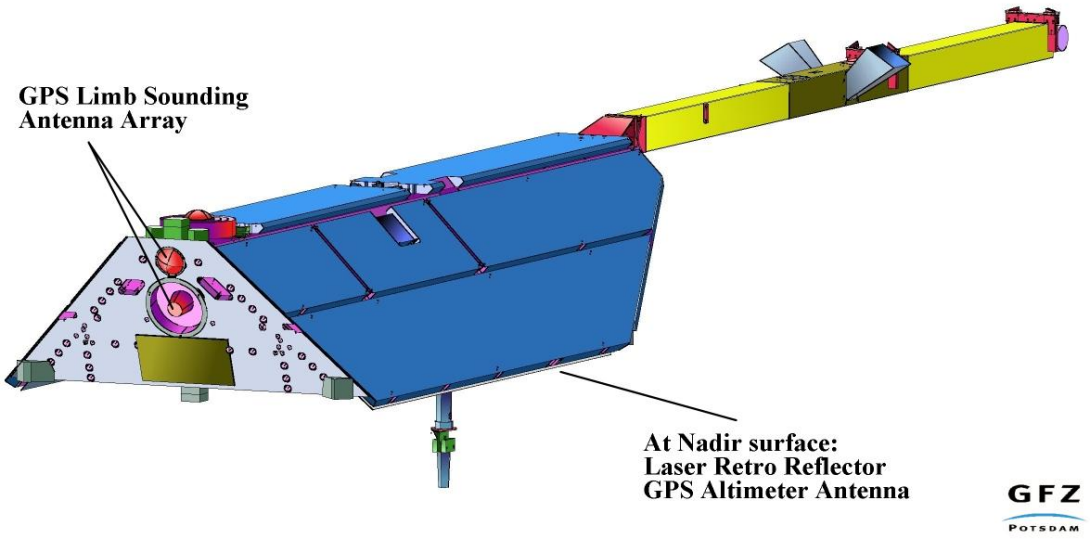

Figure 2.3: *CHAMP rear side (courtesy of GFZ Potsdam)*

The important payload for the POD applications consisted of a BlackJack GPS receiver manufactured by the Jet Propulsion Laboratory (JPL) *(Kuang et al, 2001)* which collects dual-frequency phase and code measurements at a sample rate of 0.1 Hz. The prime navigation GNSS antenna was equipped with a choke ring placed on top of the satellite (see Fig. 2.2). For the study of the physical properties of the troposphere and ionosphere, two limb-viewing antennas were mounted on the rear side of the spacecraft *(Wickert et al, 2005)*.

Orbit maneuvers performed by gas thrusters are necessary to keep the spacecrafts orientation/attitude close to its nominal attitude. CHAMPs attitude was determined by stellar sensors in form of quaternions *(Jorgensen, 1999)*. The attitude data is necessary to transform coordinates from spacecraft frame into inertial frame and vice versa (see sec. 5.8.3). The Advanced Stellar Compass (ASC) provided high accurate attitude data with a precision of approximately 4 arcsec *(Jäggi, 2007)*. For validation purposes, the tracking of the CHAMP satellite by independent Satellite Laser Ranging (SLR) measurements was possible. Therefore, a laser retro-reflector was mounted on the bottom of the satellites body.

2.2 GRACE-A

The satellite mission Gravity Recovery And Climate Experiment (GRACE) *(Tapley and Reigber, 2001)* or *(Case et al, 2002)* is based on a cooperation of the National Aeronautics and Space Administration (NASA) and the German Aerospace Center (DLR). As a direct follow-on to CHAMP the two identical satellites GRACE-A and GRACE-B (Fig. 2.4) were launched on March 17th, 2002 from Plesetsk, Russia chasing each other in a nominal orbit distance of 220 km *(Tapley, 2004)*.

As a resemblance of CHAMP, the scientific payload consists of a BlackJack GPS receiver *(Dunn et al, 2003)* which also collects dual-frequency phase and code measurement with a sample rate of 0.1 Hz and serves the navigation antenna as well as the occultation antenna for atmospheric sounding. The Star Camera Assembly (SCA) provides the satellite attitude with respect to the stars.

Due to the absence of magnetosphere science in the mission design, the requirements for the satellite orientation are less stringent compared to CHAMP. The SCA provides attitude data with a precision of about 25 arcsec *(Dunn et al, 2003)*. The

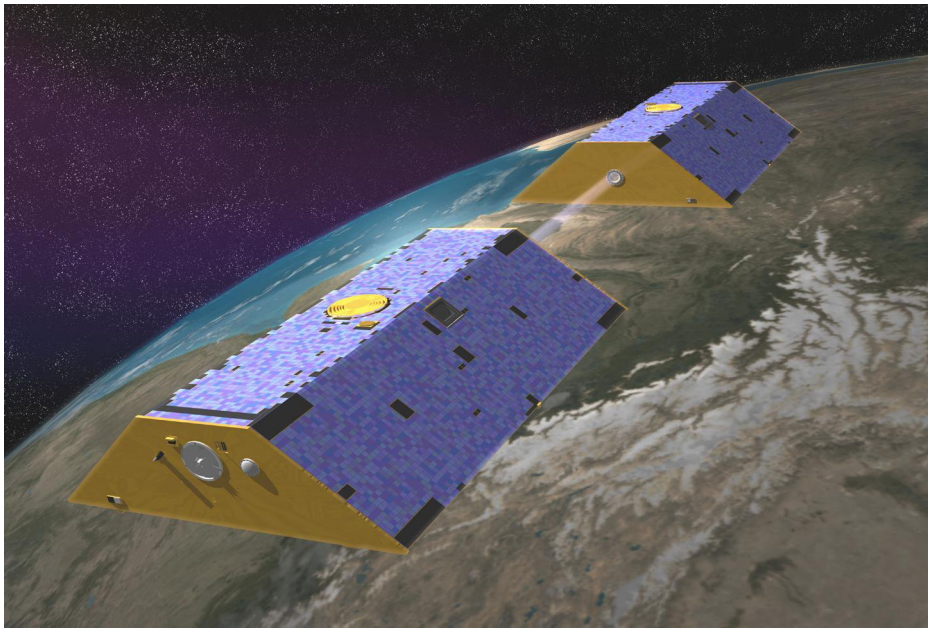

Figure 2.4: *The twin-satellite GRACE mission (courtesy of DLR)*

satellite payload is shown in Fig. 2.5. Note that for GNSS-RO measurements only the GRACE-A satellite is used and the leader-follower satellite constellation has changed since December 10th, 2005.

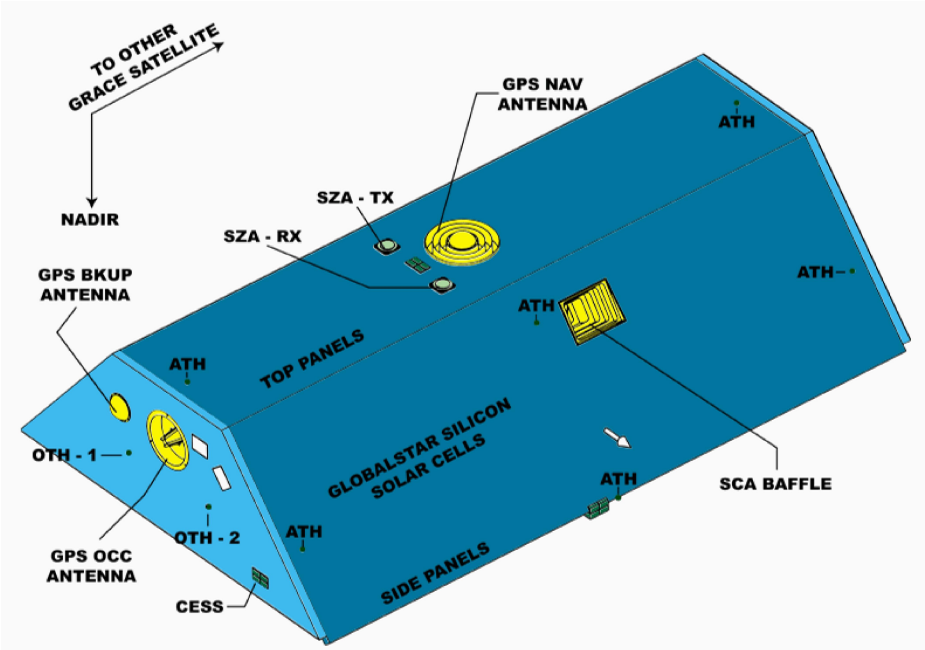

Figure 2.5: *GRACE top side (courtesy of Astrium GmbH)*

2.3 FORMOSAT-3/COSMIC

The Constellation Observing System for Meteorology, Ionosphere, and Climate (COSMIC) *(Wu et al, 2005)* is a joint Taiwan-US mission which nominally consists of 6 microsatellites. They were launched on April 15th, 2006 from Vandenberg, USA. To provide a global coverage it took more than one year to deploy the satellites into separate orbital planes.

Each satellite is equipped with a BlackJack GPS receiver (operating as Integrated GPS Occultation Receiver - IGOR) *(Wu et al, 2005)*, *(Montenbruck et al, 2006)* and is collecting measurements at 1 Hz sampling rate. For POD purposes two single-patch antennas are mounted on the main satellite body (see Fig. 2.7).

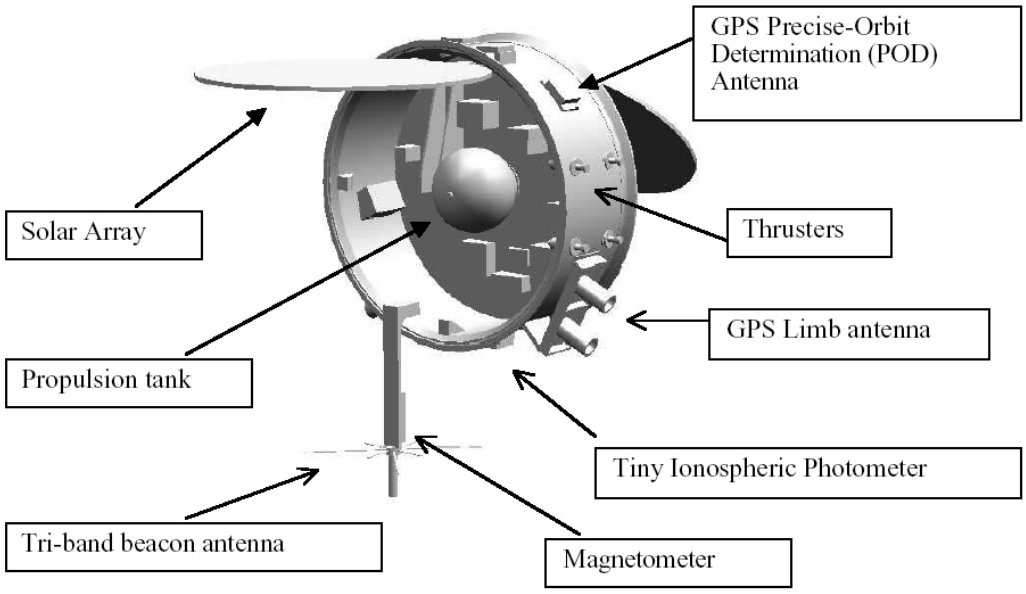

Figure 2.6: *COSMIC top side (courtesy of Taiwan National Space Organization)*

Unlike to CHAMP or GRACE the attitude determination of COSMIC is based on the combination of outputs from a magnetometer, an Earth- and a sun sensor. As investigations have been shown *(Hwang et al, 2009)*, the exertion of the attitude control produces large dynamics of the spacecraft because the satellite mass of approximately 63 kg is rather low. This may lead to degraded GNSS observations and significant coordinate transformation errors.

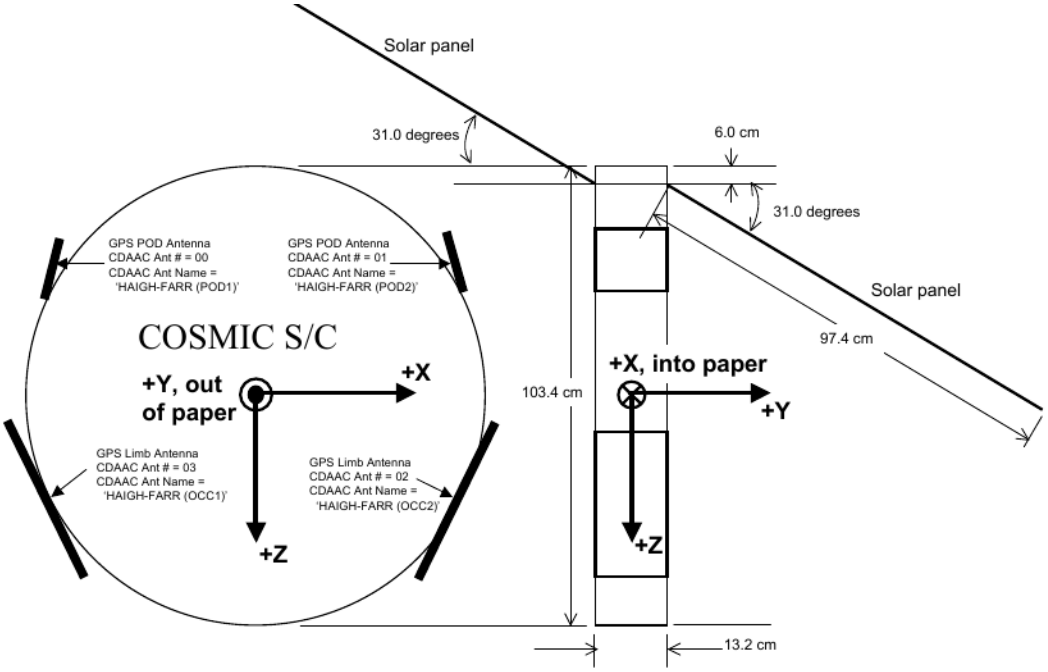

Figure 2.7: *COSMIC spacecraft geometry (courtesy of UCAR)*

For the purpose of POD the user is advised to replace the observed attitudes by nominal attitudes *(Hwang et al, 2009)*. Note that the attitude data provided from the University Corporation for Atmospheric Research (UCAR) are real measurements whereas the reduced-dynamics POD orbits are computed with nominal attitude. This may lead to discrepancies when comparing the solutions.

Currently, only 4 of the 6 satellites remain operational and a further degrading of the mission status is expected. Therefore, the follow-on mission FORMOSAT-7/COSMIC-2 is scheduled to be launched in 2016.

2.4 MetOp-A

The European Meteorological Operational Satellite (MetOp-A) *(Klaes et al, 2007)* is the first in a series of 3 weather satellites providing information for weather prediction and climatology. The mission was launched on October 19th, 2006 from Baikonur, Kazakhstan. The satellite is operated by the European Organization for the Exploitation of Meteorological Satellites (EUMETSAT). Centerpiece of the climate and geodetic research is the Global Navigation Satellite System Receiver for Atmospheric Sounding (GRAS) *(Loiselet et al, 2000)* which was designed by Saab Ericsson Space and supported by the Austrian RUAG Space GmbH.

The GRAS unit provides dual-frequency navigation and occultation measurements from a spaceborne platform *(Montenbruck et al, 2008)*. The measurements from the zenith pointing POD antenna (denoted as GZA) are provided with a sample rate of 1 Hz. The two other occultation antennas (GVA and GAVA) are pointing in velocity and anti-velocity direction. An overview of the payload aboard is given in Fig. 2.8.

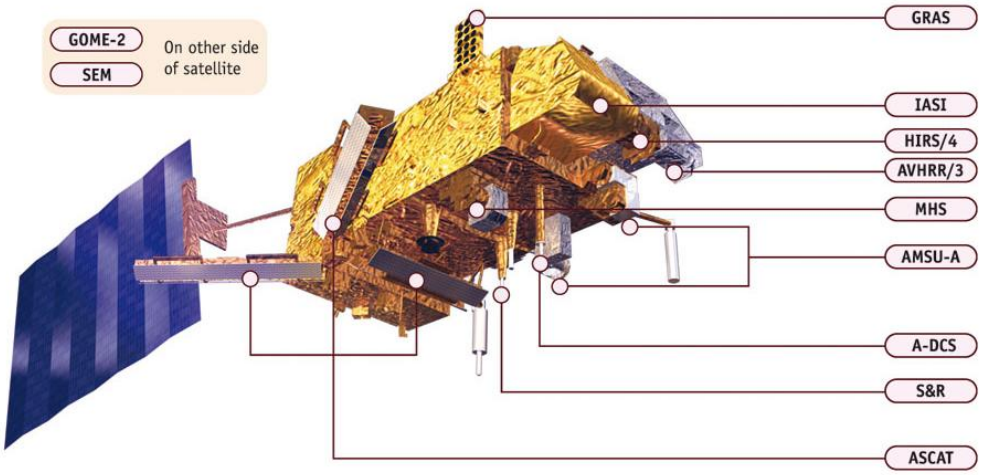

Figure 2.8: *MetOp-A satellite and payload (courtesy of EUMETSAT)*

For MetOp-A the freely available attitude data provided by UCAR is of nominal type. The nominal attitude data consists of the best possible alignment of the satellite axes with respect to along, across and radial direction (see sec. 5.8.3). The access to the real measurements is restricted. A detailed mission description is available on the website of the European Space Agency (ESA)[1]. Note that the follow-on mission MetOp-B was already launched in 2012.

[1] http://www.esa.int/Our_Activities/Observing_the_Earth/The_Living_Planet_Programme/Meteorological_missions/MetOp/

2.5 Spaceborne Receiver Characteristics

The data quality of the collected GNSS measurements is essential for any positioning application. For this purpose, intensive in-flight validation has been carried out to determine a realistic variance level of different observation types *(Montenbruck and Kroes, 2003)*. The used dual-frequency GNSS receivers are individual for every investigated LEO mission. To see the features of different spaceborne receiver types a brief overview of the characteristics is given in Tab. 2.1.

Table 2.1: *Receiver characteristics (Montenbruck, 2003a)*

Receiver	**Chan.**	**Ant.**	**Data**	**Nav. Acc.**	**Mission**
BlackJack (JPL)	16x3	4	C/A,P1,P2,L1,L2	10m SPP	CHAMP, GRACE-A
IGOR (BRE)	16x3	4	C/A,P1,P2,L1,L2	10m SPP	FORMOSAT-3/COSMIC
GRAS (Saab)	12x3	1+2	C/A,P1,P2,L1,L2	20m SPP	MetOp-A

The BlackJack and IGOR technology is very similar because, as a result of license agreements, the Broad Research Engineering Company designed a new receiver based on NASA's top quality device. Note that LEO satellites at altitudes of 400 km have a velocity of approximately 8 km/s. Taking this very high velocity and fast changing observation geometry into account, the achievable errors (sub-cm level) on the receiver phase observation side are remarkable.

3 Fundamentals of the Global Positioning System (GPS)

GPS is one of the best documented GNSS systems. Besides all terrestrial applications it is also suited for spaceborne applications such as POD. As described well by *(Hofmann-Wellenhof et al, 2008)* or *(Leick, 2003)* the GPS satellites are flying in an altitude of approximately 20.200 km and each satellite circles the Earth with a revolution period of 11 hours and 58 minutes. The nominal constellation is of 24 satellites, distributed on 6 orbital planes. In addition, 8 backup satellites are available to ensure the continuous and global coverage 24/7. The GPS orbits are almost circular and inclined by 55° with respect to the equator. In Fig. 3.1 the planes of the satellites in an inertial space fixed system can be seen. This chapter will provide a brief introduction to the GPS system.

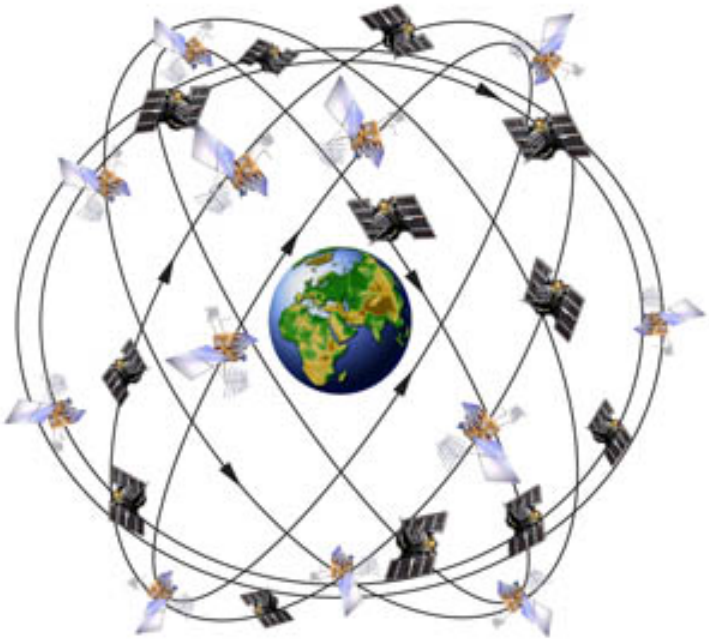

Figure 3.1: *GPS constellation (courtesy of the US Government)*

Since 1995, the GPS system has been fully operational. This means that at least 4 satellites are available for positioning at any place and time all over the world. To be up to date the system is continuously being modernized with new generation

satellites *(Hofmann-Wellenhof et al, 2008)*. These so called blocks are manufactured by different producers. Therefore, they are of different shape and have to be distinguished when applying observation corrections (e.g. solar radiation pressure). For more details see *(Bar-Sever, 1995)* or *(Hugentobler et al, 2003)*. An overview about the different GPS tranches is given in Tab. 3.1.

Table 3.1: *Different tranches of GPS satellites*

Tranche	**Type**	**Time span [years]**
Block I	Navigation development satellites	1978 - 1985
Block II	Operational satellites	1989 - 1990
Block IIA	Operational satellites	1990 - 1997
Block IIR	Replacement operational satellites	1997 - 2005
Block IIR-M	Modernized satellites	2005 - 2010
Block IIF	Follow-on operational satellites	2010 - ongoing
Block III	Third generation	2016 - future

An illustration of the above mentioned GPS tranches is shown in Fig. 3.2.

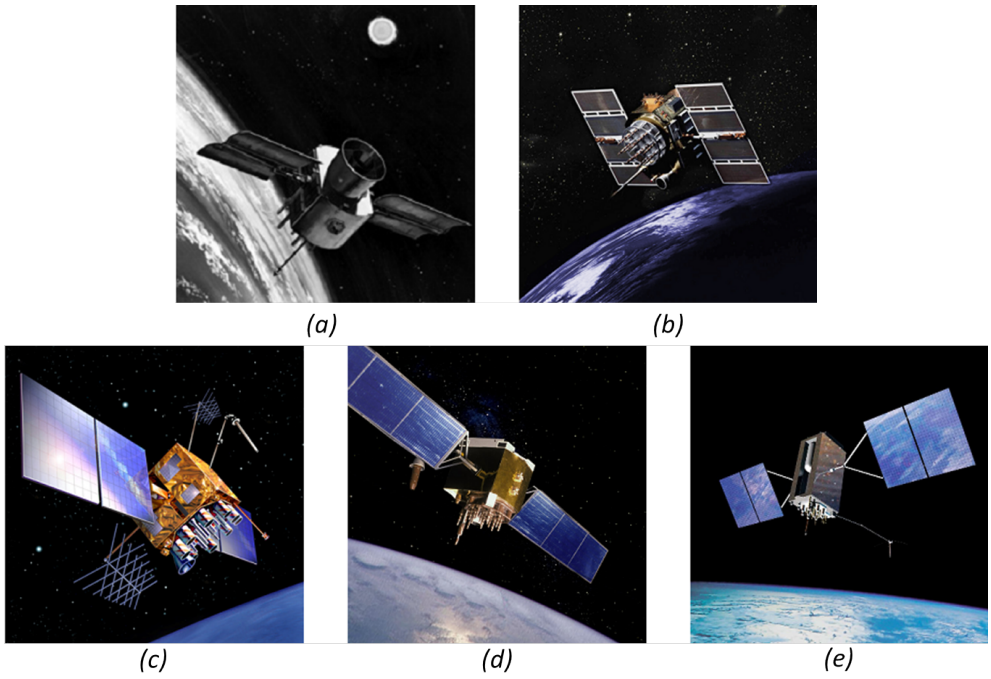

Figure 3.2: *(a) Block I, (b) Block II/IIA, (c) Block IIR/IIR-M, (d) Block IIF, (e) Block III, (courtesy of www.gps.gov)*

3.1 GPS Frequencies

GPS satellites are continuously emitting an electromagnetic wave on two carriers L_1 and L_2 in the microwave L-Band. The two carrier frequencies are obtained from the GPS fundamental frequency f_0 of 10.23 MHz which is controlled by stable and highly precise atomic clocks *(Hofmann-Wellenhof et al, 2008)*. By multiplying the fundamental frequency with 154 and 120 respectively, it follows

$$\begin{aligned} L_1 &= 1575.42\ [MHz] \\ L_2 &= 1227.60\ [MHz] \end{aligned} \tag{3.1}$$

The dual-frequency concept is essential for the elimination of error sources. The wavelength of the signals is determined by

$$\begin{aligned} \lambda_1 = \frac{c}{L_1} &= 19.029367\ [cm] \\ \lambda_2 = \frac{c}{L_2} &= 24.421021\ [cm] \end{aligned} \tag{3.2}$$

where c denotes the speed of light in vacuum ($c = 299792458\ m/s$). The two carriers are modulated with pseudo-random noise (PRN) codes. The Coarse/Acquisition (C/A) code is modulated on the L_1 carrier only. The military precision (P or Y) code is modulated on both carriers L_1 and L_2. These codes are used to compute the pseudoranges from the measured travel time of the signal to the GPS receiver. Additionally, the GPS satellites broadcast a navigation message which contains information about the satellite clock, almanac data, orbit ephemerides, as well as correction data (e.g. ionospheric corrections). The prominent components of the GPS signal are summarized in Tab. 3.2.

For highly precise positioning the accuracy of the provided broadcast orbits and clock data is insufficient in meeting requirements of POD with the chosen zero-difference approach (see chap. 5). Therefore, these data sets are provided by external analysis centers. This is discussed in the following section.

Table 3.2: *Components of the GPS signal (Hofmann-Wellenhof et al, 2008)*

Component	**Frequency or code chipping rate [MHz]**	**Wavelength [m]**
Fundamental frequency	f_0=10.23	29.305225
L_1	$154 \cdot f_0$=1575.42	0.19029367
L_2	$120 \cdot f_0$=1227.60	0.24421021
P-Code	f_0=10.23	29.305225
C/A Code	$\frac{f_0}{10}$=1.023	293.05225
Navigation message	$\frac{f_0}{204600}$=$50 \cdot 10^{-6}$	

3.2 International GNSS Service (IGS)

The IGS is a federation of more than 200 agencies worldwide collecting permanent GNSS station data to generate precise products *(Dow et al, 2009)*. Currently, there are 453 active tracking stations available as shown in Fig. 3.3 and the number of contributors is increasing continuously.

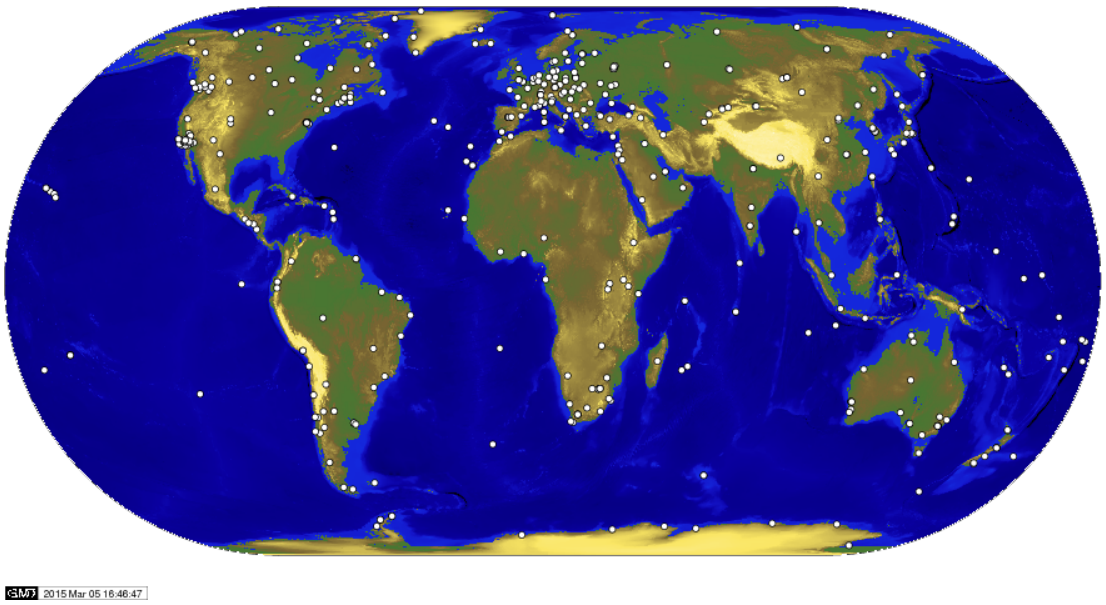

Figure 3.3: *IGS tracking network stations, March 2015, (courtesy of IGS)*

3.2.1 GNSS Orbit and Clock Products

For the POD applications the IGS is providing highly accurate GNSS ephemerides and clock data as well as Earth orientation parameters *(Dow et al, 2005)*. All mentioned data and products are freely available and can be easily downloaded from the IGS website[1]. In addition, a list of all Analysis Centers (ACs) can be found there. These orbits and clock products are computed independently by several ACs beforehand. Afterwards, the IGS output product is generated by suitable weighting between the ACs for each GPS week individually. This is shown in Fig. 3.4.

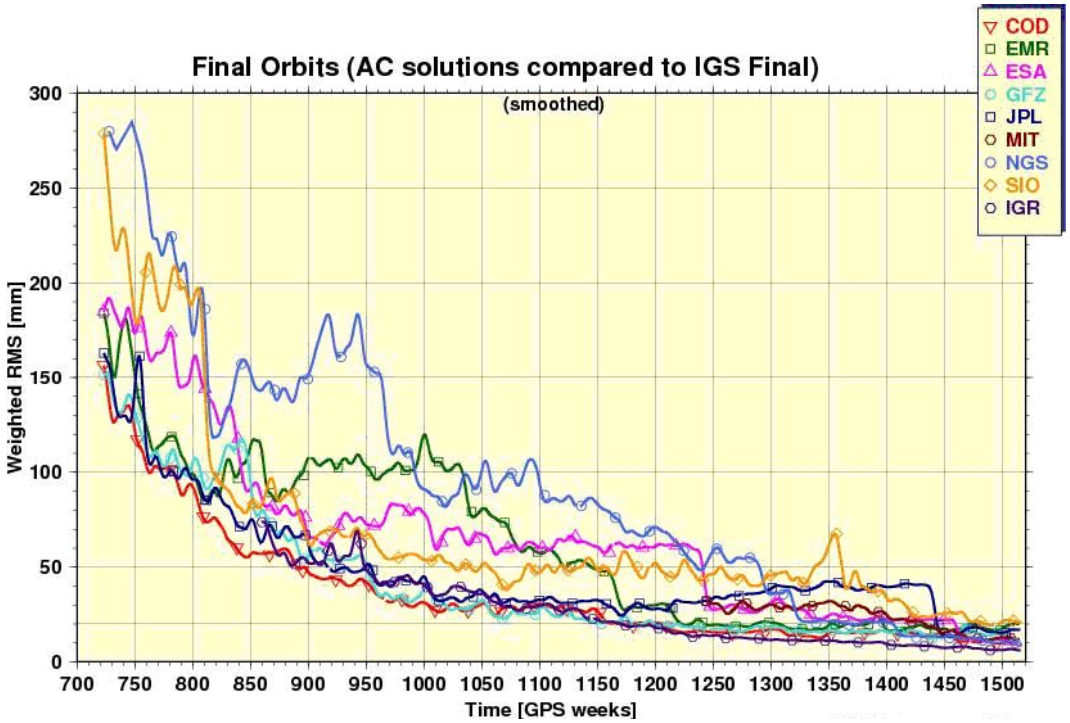

Figure 3.4: *Weighted orbit RMS of the IGS final orbit products and AC final orbit solutions during 1994-2009 (courtesy of IGS)*

Note that GPS weeks start from Jan. 6th 1980, and since GPS week 1129, which corresponds to Sept. 1st 2001, continuous GNSS-RO records are available.

Currently, the accuracy of the final products is of **2.5 cm** for the orbit positions and **75 ps** for the clocks *(Griffiths and Ray, 2009)*. The standard format for the distribution of the orbit solutions is the SP3-c format *(Hilla, 2010)*. The SP3-c file contains position, velocities and clock offsets of the GPS satellites with 15 minutes

[1] http://acc.igs.org/

sampling in an Earth fixed frame. Besides the orbit releases, also precise clock information with 30 seconds sampling in clock-RINEX format version 3.02 *(Ray and Gurtner, 2010)* is provided. This data is needed for POD applications. For more detailed information, *(Dow et al, 2005)* can be consulted.

Quality and Sampling of the Provided Products

For the upcoming orbit and excess phase processing of the Reference Occultation Processing System rOPS *(Kirchengast et al, 2013)* at Wegener Center for Climate and Global Change[2], two types of GNSS satellite ephemerides are of special interest. On the one hand, the final orbit product which is available with a latency of 12-18 days and on the other hand, the rapid ephemerides product available with a latency of 17-41 hours. The latter is used for the so called fast-track (FTR) processing while the former is used for the post-process track (PTR) processing and during re-processing (RPR) of entire radio occultation satellite records *(Kirchengast et al, 2013)*. In Tab. 3.3 all important IGS positioning products are shown. The values are taken from the official website[3].

Table 3.3: *IGS product table for GPS - status April 2015*

GPS orbits and clocks	**Accuracy orbit**	**Accuracy clock**	**Latency**	**Sampling of orbit/clock**
Broadcast ephemerides	100 cm	5 ns	no	daily
Ultra rapid (predicted half)	5 cm	3 ns	no	15 min/(N/A)
Ultra rapid (observed half)	3 cm	150 ps	3-9h	15 min/(N/A)
Rapid - for FTR	2.5 cm	75 ps	17-41h	15min/5min
Final - for PTR/RPR	2.5 cm	75 ps	12-18d	15min/30s

3.2.2 Center for Orbit Determination in Europe (CODE)

The CODE which is located at the University of Bern (AIUB), Switzerland, is one of the 10 ACs of the IGS. With more than 20 years of experience within the field of GNSS research it has made a significant contribution to the IGS output products. Therefore, the provided products from AIUB are computed with the Bernese GNSS software *(Dach et al, 2007)*.

[2]http://wegcenter.uni-graz.at
[3]http://igs.org/products

The latest version of this package (see sec. 5.7) is used to estimate the POD orbits and clock products within this research. For further information about CODE and its strategy see e.g. *(Hugentobler et al, 2004)*. Table 3.4 shows important CODE orbit products, again with the both types selected to be used within the rOPS. The accuracy information for the positions is directly expressed by accuracy codes within the header section of the SP3-c format. According to the SP3-c definition, an accuracy code n denotes a one sigma position accuracy of $\pm$ 2 mm to the power of n for each individual GNSS satellite during the whole period covered by the file. Typical accuracy codes for final products are < 6. The given clock errors are formal errors from the estimation process referring to the orbits from a three days long-arc analysis. For more information the reader is referred to the CODE analysis strategy summary.[4]

Table 3.4: *CODE product table for GPS - status April 2015*

GPS orbits and clocks	**Accuracy orbit**	**Accuracy clock**	**Latency**	**Sampling of orbit/clock**
Ultra rapid	6.4-25.6 cm	N/A	3-9h	15 min/(N/A)
Rapid - for FTR	3.2-6.4 cm	40-60 ps	17-41h	15min/30s
Final - for PTR/RPR	0.8-3.2 cm	40-60 ps	12-18d	15min/30s/5s

3.3 Modeling of GNSS Observations

In general, GNSS observations are ranges derived from measured time or phase differences based on a comparison of received signals and receiver generated signals *(Hofmann-Wellenhof et al, 2008)*. Due to the imperfect synchronization between GNSS satellite clocks and receiver clocks, the ranges are often denoted as pseudoranges. Most receivers have the ability to collect three types of GNSS observations

1. Code
2. Phase
3. Doppler shift or range-rates

[4] ftp://ftp.unibe.ch/aiub/CODE/CODE.ACN

However, the collected military P-code is encrypted (denoted as Y-code) but several techniques e.g. semi-codeless tracking have been developed to make the signal practicable without a decryption key *(Woo, 1999)*. The mathematical basics of the GNSS observations as needed for POD applications will be provided in the following section. The notation used is based on *(Jäggi, 2007)* and *(Hofmann-Wellenhof et al, 2008)*.

3.3.1 Code Observations

The C/A- and P-code is transmitted by a GNSS satellite k at time T^k and registered by a receiver i at time T_i. In general, the code equation reads

$$R_i^k = c\,(T_i - T^k) + \epsilon_i^k\ , \tag{3.3}$$

where R_i^k is the code observation, c is the speed of light in vacuum, T^k is the transmission time of the signal measured by the clock of the GNSS satellite k and T_i is the arrival or observation time measured by the clock of the receiver i. The term ϵ_i^k describes all general residual errors, which contain all effects to be modeled in order to get highly precise results *(Jäggi, 2007)*.

The official GPS terrestrial frame is a three dimensional Earth-centered World Geodetic System with the reference pole and meridian referred to the year 1984 (WGS-84). The GPS system has its own time frame denoted as GPS time *(Rockwell, 1984)*. This time system is related to the International Atomic Time (TAI - from the French name Temps Atomique International) with a constant -19 seconds offset. All GPS satellites are equipped with highly precise cesium or rubidium atomic clocks depending on the GPS tranche (see Tab. 3.1). This ensures a frequency stability between 10^{-13} and 10^{-15} seconds over one hour. However, the receiver clocks aboard the LEO satellites are less accurate but they keep their time closely synchronized with the GPS time *(Jäggi, 2007)*.

To achieve the highest accuracy, several effects have to be considered additionally. The general code equation related to the GPS time reads

$$R_i^k = \rho_i^k + c\Delta t_i + c\Delta t^k + \Delta\rho_{i,ion}^k + \Delta\rho_{i,trop}^k + \Delta\rho_{i,DCB}^k + \Delta\rho_{i,PCO}^k + \Delta\rho_{i,PCV}^k + \Delta\rho_{i,rel}^k \ , \quad (3.4)$$

where

ρ_i^k is the geometrical distance between receiver i and GNSS satellite k,
c is the speed of light,
Δt_i is the receiver clock offset,
Δt^k is the transmitter clock offset,
$\Delta\rho_{i,ion}^k$ is the ionospheric signal delay,
$\Delta\rho_{i,trop}^k$ is the tropospheric signal delay,
$\Delta\rho_{i,DCB}^k$ is the differential code bias,
$\Delta\rho_{i,PCO}^k$ is the phase center offset,
$\Delta\rho_{i,PCV}^k$ is the phase center variation,
$\Delta\rho_{i,rel}^k$ is the relativistic correction.

Hardware delays, and multipath effects as well as thermal measurement noise may be considered in addition *(Kroes et al, 2005)*. Note that for POD the $\Delta\rho_{i,trop}^k$ term cancels out because the troposphere does not exist at LEO altitudes.

3.3.2 Phase Observations

In general, phase observation of the carriers L_1 and L_2 transmitted by a GNSS satellite k at time T^k and registered by a receiver i at time T_i is given by

$$L_i^k = \lambda(\Phi_i - \Phi^k + B_i^k) \ . \quad (3.5)$$

where

L_i^k is the accumulated carrier phase observation,
λ is the wavelength of the carrier,
Φ_i is the reference carrier phase, receiver generated at arrival time T_i,
Φ^k is the carrier phase of the transmitted signal at transmission time T^k,
B_i^k is the initial carrier phase ambiguity.

The phase observation concept is based on a accumulation of the number of full carrier cycles plus the fractional part. The result is multiplied with the corresponding carrier wavelength given in Eq. 3.2. To be more accurate, correction terms may be introduced in analogy to the code observation of Eq. 3.4. The phase observation is now given by

$$L_i^k = \rho_i^k + c\Delta t_i + c\Delta t^k + \lambda N_i^k - \Delta\rho_{i,ion}^k + \Delta\rho_{i,trop}^k + \\ + \Delta\rho_{i,UPB}^k + \Delta\rho_{i,wind-up}^k + \Delta\rho_{i,PCO}^k + \Delta\rho_{i,PCV}^k + \Delta\rho_{i,rel}^k \ , \quad (3.6)$$

where

N_i^k is a constant bias to the initial carrier phase ambiguity B_i^k,
$\Delta\rho_{i,UPB}^k$ is the uncalibrated phase bias,
$\Delta\rho_{i,wind-up}^k$ is the phase wind-up.

Compared to the code observations (see Eq. 3.4) some differences can be identified. The main difference is the constant N_i^k which consists of the constant integer valued initial carrier phase ambiguity B_i^k and a real valued phase difference between Φ_i and Φ^k. In case the receiver gets loss of lock of the GNSS satellite signal, an additional bias denoted as cycle slip has to be set up due to the discontinuity in the accumulated carrier phase observations *(Jäggi, 2007)*. Furthermore, the polarized carrier phase observations are influenced by phase wind-up effects *(Wu et al, 1993)* and the ionospheric delay $\Delta\rho_{i,ion}^k$ has an opposite sign due to physical reasons. For a more detailed discussion on this topic, the reader is referred to *(Seeber, 2003)*. The observation equations are related to the satellite's center of mass. Therefore, the Phase Center Offsets (PCO) and Phase Center Variations (PCV) as well as the center of mass corrections for both the transmitter and the receiver side have been applied as well in Eq. 3.6.

3.3.3 Doppler Observations

The Doppler shift denotes as the difference between the received satellite frequency and the stable frequency emitted by the GNSS satellite *(Luo, 2012)*. Doppler shifts are linearly dependent on the radial velocity. Thus, they are well suited for velocity determination. The Doppler shift, scaled to range rates, is given as

$$D = \dot{L}_i^k = \dot{\rho}_i{}^k + c\ \dot{\Delta}t_i + c\ \dot{\Delta}t^k + \dot{\epsilon}_i^k\ , \tag{3.7}$$

where the time derivatives are indicated with dots. The term ϵ_i^k denotes the residual error including all further terms (see Eq. 3.6). Additional information about range rates can be found in e.g. *(Hofmann-Wellenhof et al, 2008)*.

3.4 Linear Combination of GNSS Observations

Different types of linear combinations can be formed in GNSS data analysis. Based on code or phase measurements on two frequencies these combinations are in particular

- Ionosphere free linear combination (L3),
- Geometry free linear combination (L4),
- Wide-lane linear combination (L5),
- Melbourne-Wübbena linear combination (L6),

where L3-L6 is the short notation. Every single combination is well-suited for a particular purpose and details can be found in *(Dach et al, 2007)*.

The ionosphere free linear combination (L3), which is very important for POD, is needed to eliminate the first order ionospheric refraction. More on this topic can be found in section 3.5. The geometry free linear combination (L4) with $L4 = L_1 - L_2$, is suitable to estimate ionospheric models due to the lack of clock errors on receiver and transmitter side. It is independent from geometry, too. The wide-lane (L5) combination is often used for ambiguity resolution due to the large wavelength of 86 cm. The Melbourne-Wübbena (L6) combination is defined as the difference between the carrier phase wide-lane and the code narrow-lane combinations and is used for data screening *(Seeber, 2003)*.

3.5 The Ionosphere Free Linear Combination

The zero-difference ionosphere free linear combination (L3), is used for LEO POD throughout this thesis. This combination eliminates the first order ionospheric effect and makes highly accurate point positioning and orbit determination possible.

Due to the fact that the ionosphere is a dispersive medium and as a consequence frequency dependent, it can be almost eliminated by using the following common combination for phase observations *(Hofmann-Wellenhof et al, 2008)*

$$L3 = \frac{f_{L1}^2}{f_{L1}^2 - f_{L2}^2} \cdot L_1 - \frac{f_{L2}^2}{f_{L1}^2 - f_{L2}^2} \cdot L_2 \approx 2.546 \cdot L_1 - 1.546 \cdot L_2 \ , \tag{3.8}$$

and code observations respectively,

$$P3 = \frac{f_{L1}^2}{f_{L1}^2 - f_{L2}^2} \cdot P_1 - \frac{f_{L2}^2}{f_{L1}^2 - f_{L2}^2} \cdot P_2 \approx 2.546 \cdot P_1 - 1.546 \cdot P_2 \ . \tag{3.9}$$

Taking the ionosphere free observation model for carrier phase and code observations into account, this leads to the two final observation equations

$$\begin{aligned} L_i^k = \rho_i^k + c\Delta t_i + c\Delta t^k + \lambda N_i^k + \Delta\rho_{i,trop}^k \\ + \Delta\rho_{i,UPB}^k + \Delta\rho_{i,wind-up}^k + \Delta\rho_{i,PCO}^k + \Delta\rho_{i,PCV}^k + \Delta\rho_{i,rel}^k \ , \end{aligned} \tag{3.10}$$

$$\begin{aligned} R_i^k = \rho_i^k + c\Delta t_i + c\Delta t^k + \Delta\rho_{i,trop}^k + \Delta\rho_{i,DCB}^k \\ + \Delta\rho_{i,PCO}^k + \Delta\rho_{i,PCV}^k + \Delta\rho_{i,rel}^k \ . \end{aligned} \tag{3.11}$$

Due to multiplication with real numbered values (see Eq. 3.8), the integer characteristic of the ambiguity is lost. The resulting wavelength of the ionospheric free linear combination λ_3 is of approximately 11 cm but the noise level is roughly three times higher compared to the primary single frequency measurements. For a detailed summary on all mentioned linear combinations and their practical usage in the Bernese GNSS software, the reader is referred to *(Dach et al, 2007)*.

3.6 Influence of Different Error Effects on the Observations

Both the phase and code measurements are affected by systematic errors or biases and random noise *(Hofmann-Wellenhof et al, 2008)*. In case of codes a summary of these effects with regard to code observation for LEO satellites is given in Tab. 3.5.

Table 3.5: *Code effects (Ramos-Bosch, 2008)*

Effect	**Notation**	**Influence**
Geometry	ρ_i^k	$\sim$ 20000 km
Receiver clock offset	$c\ \Delta t_i$	$<$ 300 km
GNSS clock offset	$c\ \Delta t^k$	$<$ 300 km
Relativistic effects	$\Delta\rho_{i,rel}^k$	$<$ 13 m
Ionospheric delay	$\Delta\rho_{i,ion}^k$	$\sim$ 2-5 m
GNSS satellite + LEO receiver hardware delays	$\Delta\rho_{i,delay}^k$	$<$ 2 m
Thermal noise	$\Delta\rho_{i,thermal}$	$\sim$ 1 m
Multipath	$\Delta\rho_{i,mult}$	$\sim$ 5 cm

The overall accuracy of the phase measurements which are much more accurate than the code observations is on the sub-cm level. A summary of effects included in the phase observation equation is shown in Tab. 3.6.

Table 3.6: *Carrier phase observation effects (Ramos-Bosch, 2008)*

Effect	Notation	Influence
Geometry	ρ_i^k	$\sim$ 20000 km
Receiver clock offset	$c\Delta t_i$	$<$ 300 km
GNSS clock offset	$c\Delta t^k$	$<$ 300 km
Ambiguity	λN	$\sim$ 20000 km
Relativistic effects	$\Delta\rho_{i,rel}^k$	$<$ 13 m
Ionospheric delay	$\Delta\rho_{i,ion}^k$	$\sim$ 2-5 m
GNSS satellite + LEO receiver hardware delays	$\Delta\rho_{i,delay}^k$	$<$ 2 m
Phase wind-up	$\Delta\rho_{i,wind-up}^k$	$<$ 20 cm
Multipath	$\Delta\rho_{i,mult}$	$\sim$ 2 cm
Thermal noise	$\Delta\rho_{i,thermal}$	$\sim$ 1 cm

Note that multipath effects depend on the individual shape of the LEO satellite (e.g. solar panels). Small satellites as FORMOSAT-3/COSMIC are not strongly affected by systematic multipath effects *(Rocken et al, 2009)*. This fact is illustrated in Fig. 3.5. The choke-ring antennas as mounted on GRACE or CHAMP satellites minimize this effect but cannot eliminate it.

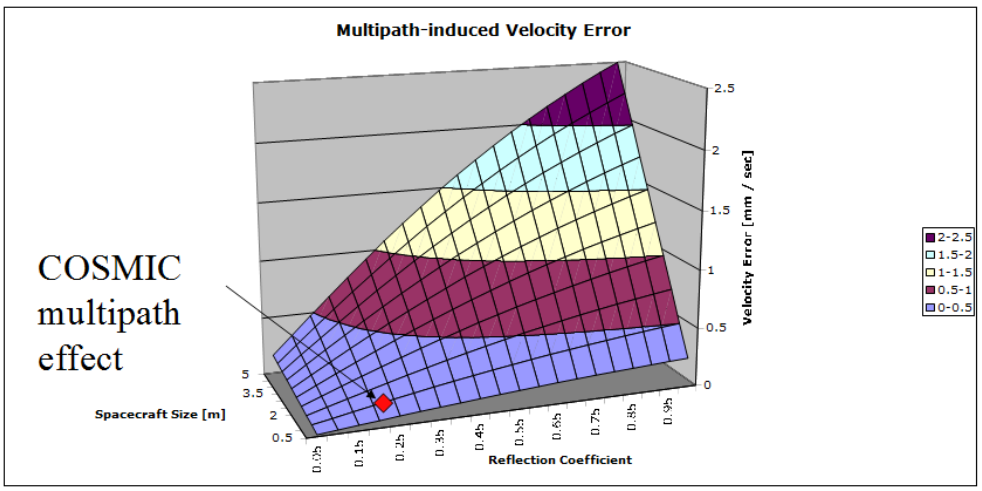

Figure 3.5: *Multipath and its impact on satellite velocity (courtesy of UCAR)*

4 GNSS Radio Occultation (GNSS-RO)

The GNSS-RO is a technique for sounding Earth atmosphere. Various profiles of bending angles, temperatures, refractivity and water vapors are obtained for the purpose of climate monitoring *(Hajj and Romans, 1998)*. GNSS-RO measurements are important for many scientific communities, namely the climatology, ionospheric physics and meteorology.

The first experimental GNSS-RO satellite mission GPS/MET was launched in 1995 in order to proof the concept*(Ware et al, 1996)*. This mission has emerged the radio occultation technique to be a very powerful approach for global atmosphere sounding. An independent validation with external data was carried out, showing a very good agreement with temperature profiles derived from radiosondes and results from Europe Centre for Medium Range Weather Forecast (ECMWF). For more details see *(Kursinski et al, 1996)*, *(Rocken et al, 1997)* or *(Steiner et al, 1999)*.

The successful GPS/MET mission has paved the way for several follow-on missions equipped with occultation payload (see chap. 2). The opportunity of long-term stability, weather independent measurements, high vertical resolution and the ability to penetrate deep into the troposphere are of fundamental importance for the success of GNSS-RO *(Hu et al, 2005)*. The basics of the GNSS-RO method are summarized in this chapter, providing a short introduction to the processing steps and the data derived from occultation measurements.

4.1 Principles of GNSS-RO

The GNSS-RO technique involves a LEO satellite receiving signals from a transmitting GNSS satellite. While the signal passes through the atmosphere it is bent. The magnitude of bending depends on the temperature and greenhouse gas concentration in the atmosphere *(Hajj and Romans, 1998)*. The basic observation constellation is illustrated in Fig. 4.1.

The bending caused the signal to travel a longer path through the atmosphere. This cannot be directly measured by the LEO receiver but it can be calculated

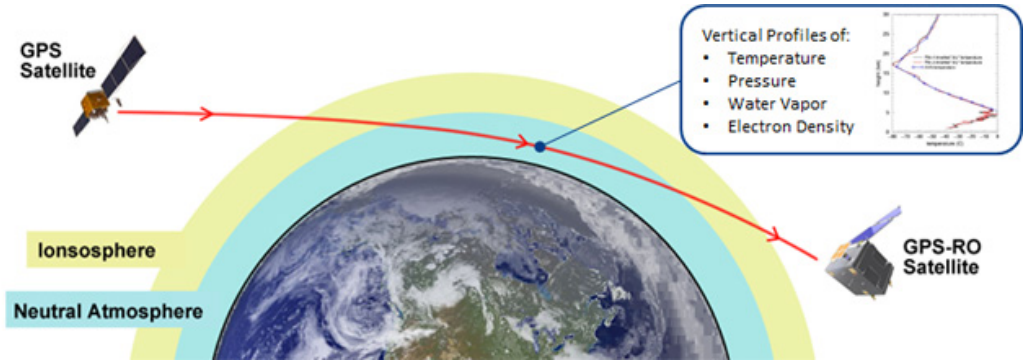

Figure 4.1: *Basic GNSS-RO constellation (courtesy of UCAR)*

from the delay in the signal arrival. In a first step, the raw excess phase is calculated (see sec. 4.3). Based on the computed excess phase, bending angles are derived and can be used to calculate the atmospheric density along the signals pass in order to obtain physical quantities as temperature, pressure, water vapor or electron density. A more detailed description on bending angles can be found in section 4.4. Depending on the movement direction of the LEO with respect to the GNSS satellite, a rising or setting occultation event with a duration of usually 60 to 180 seconds can occur.

4.2 Importance of the Precise Orbit Determination for GNSS-RO

The accurate determination of position and velocity of the LEO satellite is an essential task within the GNSS-RO processing. Basically, the geometrical part of the excess phase can be calculated as vector difference between GNSS and LEO satellite which gives the straight line S_{str} *(Schreiner et al, 2010b)*.

$$S_{str} = |\boldsymbol{r}_1 - \boldsymbol{r}_2|. \tag{4.1}$$

The excess phase can then be computed as the difference between the true ray path S_{true} and the straight line path S_{str}

$$S_{true} - S_{str} = \int ndl - |\boldsymbol{r}_1 - \boldsymbol{r}_2| \ . \tag{4.2}$$

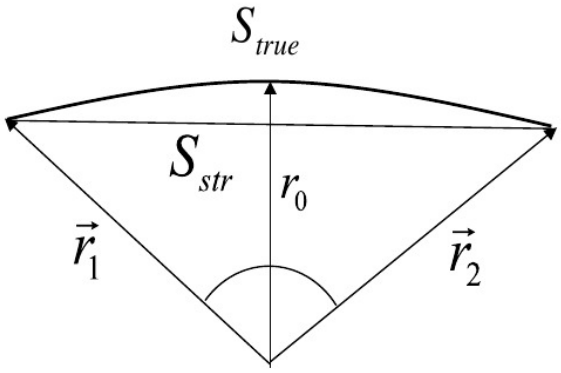

Figure 4.2: *Simplified concept (Schreiner et al, 2010b)*

This is a very simplified representation but it explains the concept in an easy way. The error of LEO positioning and velocity leads to a change in the straight line path and this propagates into further computed quantities.

Another aspect is that satellite missions are developed by different countries and manufacturers. Thus, the receiver characteristics vary (see sec. 2.5) and the quality of the observations is different, which affects the positioning quality. The satellites attitude is a critical point, too (see chap. 5). If the nominal attitude is introduced instead of the real measured satellites orientation, this is a clear indicator for significant errors when accomplishing the transformation from the spacecraft system to the inertial system (see sec. 5.8.3). This is especially the case for the FORMOSAT-3/COSMIC mission.

4.3 Atmospheric Excess Phase Computation

The computation of the atmospheric excess phase is based on high rate 50 Hz GNSS measurements, which are collected from the LEO receiver in combination with the occultation antenna. All further products derived from GNSS-RO are sensitive on the accuracy of the primarily computed excess phase. Therefore, various factors such as antenna offsets, clock drifts, relativistic effects etc. which can affect the GNSS occultation signal have to be considered in the excess phase processing *(Zhang et al, 2013)*. An example of the characteristic of the excess phase during GNSS-RO atmospheric profiling measurements can be seen in Fig. 4.3.

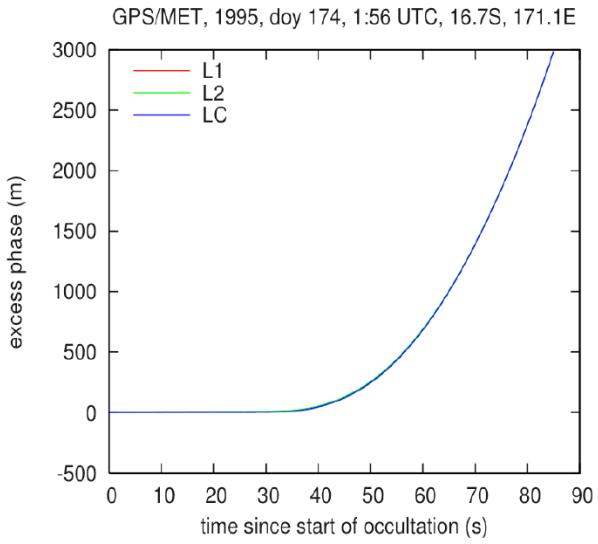

Figure 4.3: *Example of excess phase characteristic during a GNSS-RO event (Schreiner et al, 2010b)*

4.3.1 Quality of GNSS-RO Excess Phase Computation

The quality of the computed excess phase is of essential meaning. In the following, three different methods of eliminating errors in the GNSS signal based on zero, single or double-differencing are described. All methods are based on the ionosphere free linear combination as presented in section 3.5. This well-known approach is used for POD and for the computation of the excess phase. In Fig. 4.4, the three types of differencing are shown.

In general, the processing is based on different antennas. For occultation, the limb viewing antenna with 50 Hz occulting satellite tracking for atmospheric profiling is used. In contrast, the 1 Hz or 0.1 Hz observations made with the navigation antennas are used for POD. The presented approaches describe the computation of the 50 Hz data. The main differences between the three individual methods are the ways in which the effect of the clock errors is removed from the phase data. The zero-difference approach is able to produce excess phase data with a lower noise level compared to single or double-differencing. This potentially works under the condition that the prior estimated LEO and GNSS clock corrections are applied and highly accurate clocks are used aboard the LEO satellite *(Beyerle et al, 2005)*. The single and double-differencing approaches are carried out to eliminate the LEO and ground station clock fluctuations. The following concepts are taken from the UCAR processing scheme based on a publication of *(Schreiner et al, 2010a)*.

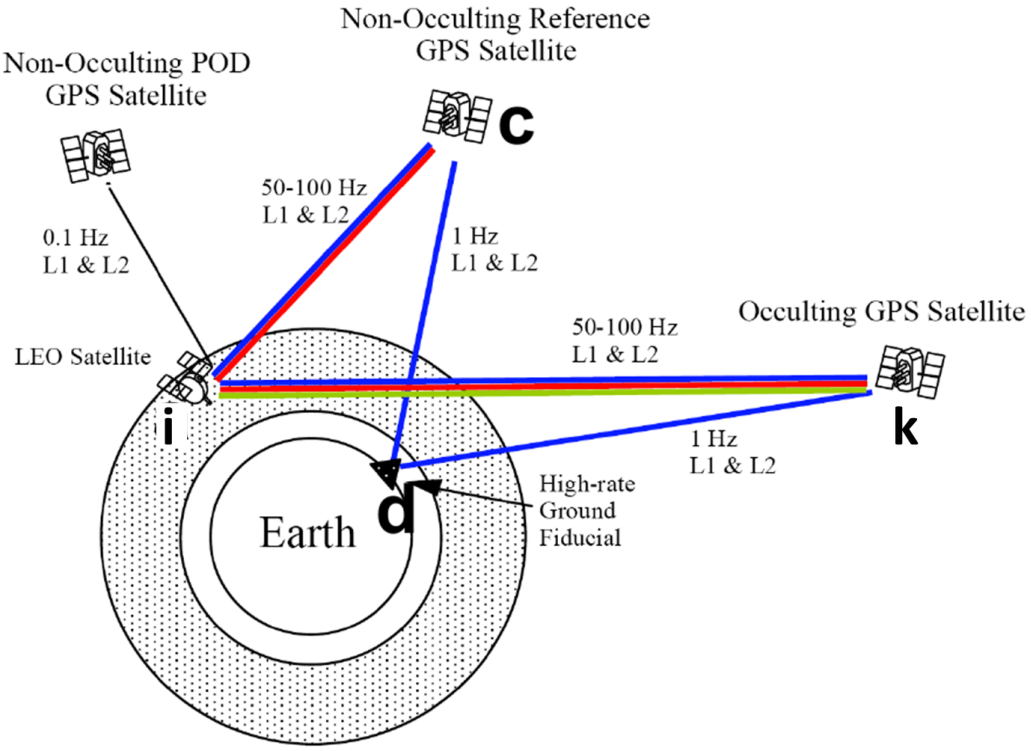

Figure 4.4: *Simplified concepts of differencing, indicated links of zero-differencing (green), single-differencing (red) and double-differencing (blue) (Schreiner et al, 2010a)*

The Wegener Center's rOPS system will employ either zero-differencing or single-differencing, depending on the quality of the LEO clock of any given GNSS-RO satellite mission. In general, GRACE-A and MetOp-A allow for zero-differencing while CHAMP and FORMOSAT-3/COSMIC require single-differencing.

4.3.2 Zero-Difference Approach

The zero-difference approach for excess phase processing assumes perfect clocks which is almost never the case. However, what was shown in *(Beyerle et al, 2005)* on the example of the GRACE mission is: an improved stability of the LEO clock compared to the CHAMP mission allows for zero-differencing due to the absence of periodic clock adjustments. This in turn reduces the noise level caused by the reference link to the non-occulting GNSS satellite. The simplified concept is valid under the constraints that LEO and GNSS satellites are stationary in space, a non existing gravitational potential and perfectly synchronized clocks. Under these circumstances all relativistic effects are vanishing and the different clock

times coincides. For more details, the reader is referred to *(Beyerle et al, 2005)*. However, if all terms in the general observation equation besides $\Delta\ \rho^k_{i,ion}(t_r)$ and $\Delta\ \rho^k_{i,trop}(t_r)$ are known or considered or vanishing, the L_1 excess phase can directly be obtained by

$$L1^k_i(t_r) = \Delta\rho^k_{i,ion}(t_r) + \Delta\rho^k_{i,trop}(t_r)\ . \tag{4.3}$$

4.3.3 Single-Difference Approach

The single-differencing procedure is needed to compute the L_1 and L_2 excess phase as a function of position and time in an Earth Centered Inertial (ECI) system *(Schreiner et al, 2010a)*. As input for the excess phase computation the following data is used

- GNSS and LEO positions, velocities and clock offsets, antenna offsets, PCVs and Earth Rotation Parameters (ERP),
- LEO attitude data,
- 50 Hz L_1 and L_2 measurements to the occulting GNSS satellite,
- 50 Hz L_1 and L_2 measurements to the non-occulting reference GNSS satellite.

The occulting 50 Hz measurements are given at irregular time tags based on an open loop tracking, whereas the non-occulting reference measurements are given at regular 20 ms time tags *(Schreiner et al, 2010a)*.

Following outputs of the single-difference approach are expected

- L_1 and L_2 excess phase,
- GNSS time for occultation events,
- LEO positions and velocities at signal reception time,
- GNSS positions and velocities at signal transmission time.

The excess phase is given between the LEO and GNSS phase centers. The carrier phase measurement for the occultation between receiver i and occulting GNSS satellite k as shown in Fig. 4.4 reads

$$L1_i^k(t_r) = c \cdot \Delta t_i(t_r) + c \cdot \Delta t_{i,rel}(t_r) + \rho_i^k(t_r) + c \cdot \Delta t^k(t_r - \tau_i^k) + c \cdot \Delta t^{k,rel}(t_r - \tau_i^k) + c \cdot \Delta\rho_{i,rel}^k(t_r) + \Delta\rho_{i,ion}^k(t_r) + \Delta\rho_{i,trop}^k(t_r) + \epsilon, \quad (4.4)$$

where t_r is the receiver time tag in GNSS time based on the LEO clock offsets computed in the POD processing using a high order polynomial. In Eq. 4.4 the ambiguities, the thermal noise and other biases are neglected. The excess phase is defined as the signal delay caused by the effects of ionosphere and troposphere. Therefore, the terms $\Delta\ \rho_{i,ion}^k(t_r)$ and $\Delta\ \rho_{i,trop}^k(t_r)$ are to be determined. The remaining terms of Eq. 4.4 are removed by differencing or modeling with the reference link observation.

The light-time equation provides the travel time τ_i^k using the LEO and GNSS orbits. Due to movements of the GNSS and LEO satellites, relativistic effects are occurring. The relativistic effect of the GNSS satellite clock is modeled at transmission time based on *(Ashby and Spilker, 1996)*

$$\Delta t^{k,rel} = -2\frac{\boldsymbol{r}^k \cdot \boldsymbol{v}^k}{c^2}\ , \quad (4.5)$$

where $\boldsymbol{r}^k$ and $\boldsymbol{v}^k$ are the position and velocity vectors of the GNSS satellite. The same equation can be used to calculate the effect for the LEO.

The general relativistic effect is caused by a gravitational delay between GNSS and LEO *(Schreiner et al, 2010a)*. This effect can also be modeled according to *(Ashby and Spilker, 1996)*

$$\Delta\rho_{i,rel}^k = \frac{2GM}{c^2} \ln\left(\frac{r^k + r_i + \rho_i^k}{r^k + r_i + \rho_i^k}\right)\ , \quad (4.6)$$

where GM is the product of gravitational constant with Earth mass and r^k and r_i are GNSS and LEO radial positions at GNSS transmission and LEO receive time.

Applying the single-differencing approach, the receiver clock error $c \cdot \Delta t_i(t_r)$ and $c \cdot \Delta t_{i,rel}(t_r)$ is eliminated using the ionosphere free linear combination in combination with the reference link here denoted as $L3_i^c$ (see sec. 3.5). The atmospheric excess phase as a function of GPS time is computed as

$$L1_i^k(t_r) - L3_i^c(t_r) = \Delta\rho_{i,ion}^k(t_r) + \Delta\rho_{i,trop}^k(t_r) \ . \tag{4.7}$$

This also holds for the L_2 excess phase computation. First the single-differencing approach forms the observables and removes the LEO clock errors afterwards. Note that the reference non-occulting GNSS satellite should be in near-zenith direction to the LEO satellite to minimize the noise of the reference link.

4.3.4 Double-Difference Approach

The double-difference processing is based on similar input as the single-differencing. Additionally, GNSS ground data for the occulting GNSS satellite and the non-occulting reference satellite as well as zenith total delay information is needed. After interpolation of the ground receiver time tags to GPS time tags using the known clock offset information, this data is in turn spline interpolated to the LEO occulting GPS time tags *(Schreiner et al, 2010a)*. Afterwards, all effects are removed except the GNSS clock offsets. The ionosphere free single-difference equation for the ground station reads

$$L3_d^b(t_r) - L3_d^c(t_r) = -c \cdot \Delta t_d^b(t_r - \tau_d^b) + c \cdot \Delta t_d^c(t_r - \tau_d^c) \ , \tag{4.8}$$

where the ground based ionosphere free phase observations are formed with the traditional approach (see sec. 3.5). By forming single-differences, the GNSS clock offsets are not completely eliminated as shown in Eq. 4.9

$$L1_i^k(t_r) - L3_i^c(t_r) = \Delta\rho_{i,ion}^k(t_r) + \Delta\rho_{i,trop}^k(t_r) - c\cdot\Delta t^k(t_r - \tau_i^k) + c\cdot\Delta t^c(t_r - \tau_i^c) \ . \tag{4.9}$$

Forming the double-difference and subtracting the known quantities will lead to the desired excess phase. The GNSS satellite clocks still remain in the equation due to an incomplete cancellation. This is caused by slightly different light times and leads to an error of small magnitude *(Schreiner et al, 2010a)*. The double-difference equation for LEO and ground single-difference observations is given by

$$L1_i^k(t_r) - L3_i^c(t_r) - (L3_d^b(t_r) - L3_d^c(t_r)) = \Delta\rho_{i,ion}^k(t_r) + \Delta\rho_{i,trop}^k(t_r) \\ - c \cdot (\Delta t^k(t_r - \tau_i^k) - \Delta t^k(t_r - \tau_d^k)) + c \cdot (\Delta t^c(t_r - \tau_i^c) - t^c(t_r - \tau_d^c)) \ . \quad (4.10)$$

Currently, the incomplete clock cancellation is neglected in the UCAR processing but there is work in progress to consider this effect in the future. Another critical aspect is the increasing noise level if ground stations are taken into account for the double-differencing.

4.4 Calculation of Bending Angles and Atmospheric Profiles

The basic observation geometry is shown in Fig. 4.5 and can be defined by three different parameters *(Kursinski et al, 2000)*

- Bending angle α,
- Impact parameter a,
- Tangent radius r_t.

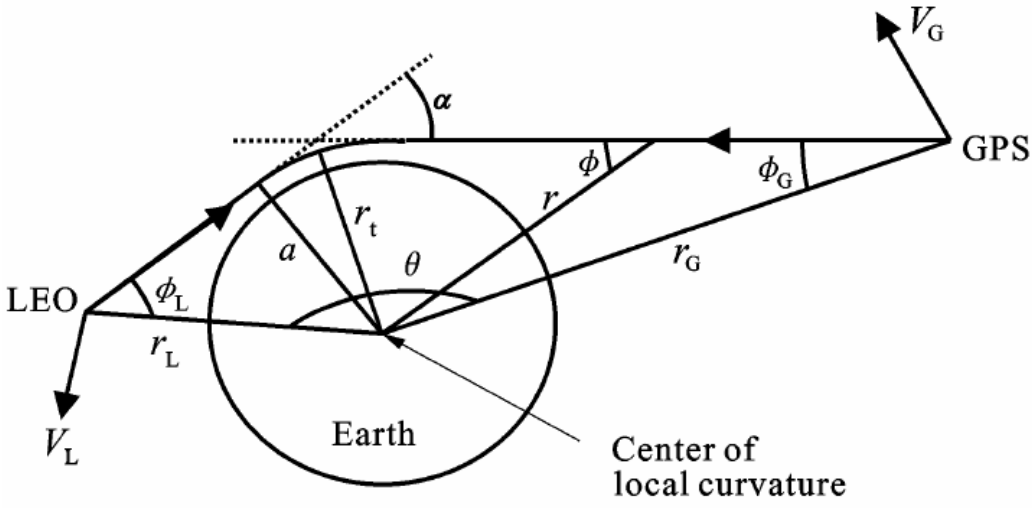

Figure 4.5: *GNSS-LEO RO observation geometry (Kursinski et al, 2000)*

The ray bending angle α defines the bending due to atmospheric refractivity. The impact parameter a is the product of atmospheric refractive index and the distance

of the ray from the curvature center ($a = n \cdot r$), and the tangent radius r_t defines the nearest distance between the ray and the Earth curvature center. This point is often denoted as tangent point.

Based on the notation of *(Hu et al, 2005)* and assuming conditions like the local spherical symmetry of Earth atmosphere refractivity, the bending angle can be expressed as

$$\alpha(a_0) = 2a_0 \int_{a_0}^{\infty} \frac{dln(n(a))}{da} \frac{1}{\sqrt{a^2 - a_0^2}} \, da \ , \tag{4.11}$$

where a_0 is the current impact parameter. Based on the Abel integration transform formula *(Hajj and Romans, 1998)*, the refractive index $n(a_0)$ can subsequently be obtained by

$$n(a_0) = \exp\left[\frac{1}{\pi} \int_{a_0}^{\infty} \frac{\alpha(a)}{\sqrt{a^2 - a_0^2}} \, da\right] \ . \tag{4.12}$$

The GNSS-RO calculation steps are defined in the following order. **Firstly**, the bending angles are obtained from the excess phase data which in turn are derived from GNSS carrier phase measurements. **Secondly**, calculating the refractive index based on equation 4.12 allows to obtain the near vertical refractivity profile at the ray tangent point. **Thirdly**, the refractivity allows for the reconstruction of the pressure, temperature and humidity, in the atmosphere and the electron density in the ionosphere using inversion methods e.g. *(Hu et al, 2005)*. This procedure is described in the following section.

4.4.1 Geometric Optics Inversion to Bending Angle

The geometric optics inversion method is based on the calculation of the Doppler frequency from GNSS phase measurements. To determine the Doppler shift the LEO tracks the GNSS phase while the signal is occulted. The LEO receiver observes the change of delaying of the signal between the GNSS and the LEO which in turn is related to slowing and bending of the signal path *(Hu et al, 2005)*. This change in the delay includes the effect caused by the atmosphere.

After eliminating clock errors on both the transmitter and the receiver side, applying relativistic corrections and cycle slip detection and fixing and also subtracting the straight line distance between GNSS and LEO (see Eq. 4.2), the atmospheric excess phase can be obtained. The excess Doppler for both carrier phase frequencies L_1 and L_2 is given by *(Hu et al, 2005)*

$$\frac{\Delta f_i}{f_i} = \frac{1}{c}\frac{d\Phi_i}{dt} \ , \ i = 1, 2 \ , \tag{4.13}$$

where c is the speed of light and the derivation of the excess phase Φ with respect to time is equal to the excess Doppler including contributions from the atmosphere and ionosphere.

With given LEO and GNSS positions as well as their corresponding velocities, the excess Doppler phase can be rewritten

$$\Delta f_i = \frac{f_i}{c}\left[\boldsymbol{v}_L \cdot \boldsymbol{t}_L - \boldsymbol{v}_G \cdot \boldsymbol{t}_G - (\boldsymbol{v}_L \cdot \boldsymbol{r}_{LG} - \boldsymbol{v}_G \cdot \boldsymbol{r}_{LG})\right] \ , \tag{4.14}$$

where

$\boldsymbol{t}_L, \boldsymbol{t}_G$ are the ray directions of both satellites,
$\boldsymbol{r}_{LG}$ is the straight line direction between the satellites,
$\boldsymbol{v}_L, \boldsymbol{v}_G$ are the velocity vectors of LEO and GNSS.

The parameters used can be seen in Fig. 4.5. After projection of the orbital motion from transmitter and receiver on the ray path, equation 4.14 is rewritten

$$\begin{aligned}\Delta f_i = \frac{f_i}{c}\ [&v_G^t \sin(\phi_G) - v_L^t \sin(\phi_L) + v_G^r \cos(\phi_G) + v_L^r \cos(\phi_L) \\ &- (\boldsymbol{v}_L \cdot \boldsymbol{r}_{LG} - \boldsymbol{v}_G \cdot \boldsymbol{r}_{LG})]\end{aligned} \tag{4.15}$$

where v_L and v_G are the scalar representations of the satellites velocities and their subscripts r and t denote the projection on the radius or tangent direction. Applying geometrical relations, the bending angle α_i for each carrier frequency can be computed as follows *(Hu et al, 2005)*

$$\alpha_i = \theta + \phi_G + \phi_L - \pi \quad i = 1, 2, \tag{4.16}$$

where θ is the angle between the LEO and GNSS satellite. Applying Snell's law, the impact parameter a_i reads

$$a_i = r_G \sin(\phi_G) = r_L \sin(\phi_L) \ . \tag{4.17}$$

To be more accurate this calculation is done iteratively. Additional corrections e.g. due to the fact that the local curvature center of the Earth is not the center of the Earth ellipsoid have to be applied *(Syndergaard, 1998)*. The bending angles and impact parameters are recalculated. Also ionosphere corrections have to be considered because the bending angle contains the contribution of the atmosphere as well as the ionosphere. Before applying the Abel transformation (Eq. 4.12) this effect has to be removed using a ionosphere free linear combination of two bending angles with the same impact parameters *(Hu et al, 2005)*. A possible combination is given by

$$\alpha_a = \frac{f_1^2 \alpha_1(a) - f_2^2 \alpha_2(a)}{f_1^2 - f_2^2} \ . \tag{4.18}$$

The first order ionospheric effect is now removed from the data. Note that the contribution to the excess Doppler of the ionosphere and atmosphere are the same at about 40 km level. Below the impact of the ionosphere decreases and finally becomes very small at about 15 km level *(Hu et al, 2005)*.

4.4.2 Calculation of Refractive Index and Atmospheric Density

As mentioned in section 4.4, the refractive index n is computed according to Eq. 4.12 but there is a singular point in the denominator of the right hand side *(Hu et al, 2005)*. To avoid the singularity in numerical integration a more suitable approach using Eq. 4.19 is introduced

$$\ln(n(a_0)) = \frac{1}{\pi} \int_{\alpha=\alpha_(a_0)}^{\alpha=0} \ln \left[\frac{a(\alpha)}{a_0} + \sqrt{\left(\frac{a(\alpha)}{a_0} \right)^2 - 1} \right] \, d\alpha. \tag{4.19}$$

Finally, the atmospheric refractivity N which is necessary to compute further climate products can be calculated. Under the condition that the water drop is neglected, the refractivity reads

$$N = (n-1) \cdot 10^6 = 77.6\frac{P}{T} + 3.73 \cdot 10^5 \frac{P_w}{T^2} \ , \tag{4.20}$$

where

P is the atmospheric pressure [hPa],

T is the atmospheric temperature [K],

P_w is the partial pressure of water vapor [hPa].

Based on this fundamental equation the atmospheric density can be computed by

$$\rho(H) = \frac{M}{R}\frac{P(h)}{T(h)} = \frac{M}{77.6\ R}N(h), \tag{4.21}$$

where M is the molecular mass ($M = 28.964kg/kmol$) and R is the gas constant ($R = 8314J/K \cdot mol$). For a more detailed discussion of this topic the reader is referred to *(Kursinski et al, 1997)*, *(Hajj and Romans, 1998)*, *(Steiner et al, 1999)* or *(Steiner et al, 2013)*.

4.5 Real Life Impact of Climate Products

An improved weather forecast and climate monitoring helps politicians to make the right decisions. In a crisis scenario this is important to save lives or protect buildings and rescue critical infrastructure. Besides the fact that the weather forecast and climate monitoring benefits from GNSS-RO measurements and get more accurate, also the prediction of natural disasters such as hurricanes are significantly improving. As the latest Intergovernmental Panel of Climate Change (IPCC)[1] report showed, there is a clear human influence on the climate and GNSS-RO contributed to detect such influences *(Lackner et al, 2011)*, *(Steiner et al, 2011)*. For a more regional point of view the reader is referred to The Austrian Assessment Report 2014 (AAR14)[2] which is based on the IPCC structure. The existing knowledge on the characteristics of climate change in Austria is presented therein.

[1] http://www.ipcc.ch

[2] http://www.apcc.ac.at

5 Precise Orbit Determination for Low Earth Orbit Satellites

The precise orbit determination is one of the major tasks within this thesis. Since the successful launch of the first satellite Sputnik in 1957, the methodology, the precision and the quality of orbit determination has increased dramatically. Nowadays, the precision of a satellite's trajectory can reach the sub-dm level. This is a requirement for satellite missions with scientific background. To meet these sophisticated mission requirements, high-end trajectory and force models as well as observation and estimation methods have been developed during the last decades.

Within this research, the zero-difference approach has been applied for all GNSS observations (see sec. 4.3.2). The ionosphere free linear combination as described in section 3.5 is used to eliminate the ionosphere. As a requirement for the zero-difference approach, high precise GNSS clocks and ephemerides are needed. This data is provided by e.g. IGS and CODE (see sec. 3.2 and 3.2.2). In addition, the double-differencing can be used. This approach eliminates errors in the GNSS ephemerides and clock errors by forming baseline differences between the ground station an the LEO *(Hofmann-Wellenhof et al, 2008)*. However, this approach is time consuming because a huge amount of GNSS observations and the complete ground station receiver network has to be processed. Finally, the triple-difference processing of GNSS data has been introduced for POD *(Byun, 2003)*.

The chosen zero-difference approach is competitive if highly precise input data is available. In this case, the resulting orbits are on the same quality compared to the other three approaches. If more than one single spacecraft is processed and high precise baselines between formation flying satellites are desired, the double-difference approach has to be preferred *(Kroes, 2006)*.

For the orbit determination several models have been invented which in turn are adjusted to the observations during the estimation process. Kinematic approaches for orbit determination (see sec. 5.5) are comparatively simple and do not require any external models *(Bock et al, 2005)*. This makes the kinematic approach very attractive for many applications. However, kinematic orbit determination

is sensitive to defective GNSS measurements, bad GNSS constellation and data gaps *(Swatschina, 2012)*.

The use of dynamic orbit modeling can overcome these problems *(Gill and Montenbruck, 2004)*. This approach is based on an a-priori knowledge of the spacecraft's motion. Physical models can be introduced to constrain the estimate of the orbit. Possible data gaps can be filled up by simply propagating the state vector according to the dynamic model *(Swatschina, 2012)*. However, especially long data arcs are affected by diverging residuals due to the insufficient knowledge of the spacecrafts dynamics. That means: the used dynamic model of the trajectory cannot be fitted well to the real observations over long periods in a least squares sense.

To overcome this problem the static dynamic model was further developed. This so called reduced-dynamic approach *(Montenbruck et al, 2005)* is provided with the necessary flexibility to adjust the trajectory to the observations in order to keep the residuals constant over long arcs *(Swatschina, 2012)*. This is achieved by applying additional empirical parameters to the estimation process. To fulfill the requirements of GNSS-RO with its 50 Hz measurements the orbit arcs must be consistent and not be interspersed by data gaps. Therefore, the reduced-dynamic approach is preferred. More information on this topic can be found in section 5.6.

5.1 Principles of Least Squares Estimation

The method of least squares estimation is used as a common method for the adjustment of the orbit models to the observations. This also holds for the Bernese GNSS software where the sum of squares of the observation residuals is minimized. If all observations are processed in one step, this is often denoted as batch least squares processing and applicable only for post processing operations. This section provides a brief introduction based on the notation of *(Montenbruck and Gill, 2000)*.

The observations are given in the vector $\boldsymbol{l}$. The functional model $\boldsymbol{F}$ includes the observation equations related to the estimation parameters contained in the vector $\boldsymbol{x}$ *(Swatschina, 2012)*. Including the residual vector $\boldsymbol{\epsilon}$, the observation equation reads

$$\boldsymbol{l} + \boldsymbol{\epsilon} = \boldsymbol{F}(\boldsymbol{x}) \ . \tag{5.1}$$

The nature of the functional model is not linear and has to be linearized for the purpose of least squares adjustment. The linearization step by using a reference solution with a-priori introduced values for the unknowns leads to

$$\boldsymbol{l} + \boldsymbol{\epsilon} = \boldsymbol{F}(\boldsymbol{x}_0) + \boldsymbol{A}\boldsymbol{x} \ , \tag{5.2}$$

where

- $\boldsymbol{A}$ is the design matrix,
- $\boldsymbol{x}_0$ denotes the vector of a-priori values for the unknowns,
- $\boldsymbol{x}$ denotes the vector for the corrections of the a-priori values $\boldsymbol{x}_0$,

and the design matrix $\boldsymbol{A}$ in turn is defined as the Jacobian matrix of $\boldsymbol{F}$

$$\boldsymbol{A} = \frac{\partial \boldsymbol{F}(\boldsymbol{x})}{\partial \boldsymbol{x}}\Big|_{x=x_0} \ . \tag{5.3}$$

The correction equation can be expressed by introducing the a-priori values for all estimation parameters. The residual vector reads

$$\boldsymbol{\epsilon} = \boldsymbol{A}\boldsymbol{x} - (\boldsymbol{l} - \boldsymbol{F}(\boldsymbol{x}_0)) \ , \tag{5.4}$$

where the term in brackets can be rewritten as $\boldsymbol{y} = \boldsymbol{l} - \boldsymbol{F}(\boldsymbol{x}_0)$. The differences between the present observations and the observations from the reference solution are often described as "*observed minus computed*".

The stochastic behavior of the model is described by the observation covariance matrix $\boldsymbol{Q}_{ll}$ which includes the variances σ_i of the observations. The weighting matrix $\boldsymbol{P}$ is given by

$$\boldsymbol{P} = \sigma_0^2 \ \boldsymbol{Q}_{ll}^{-1} \ , \tag{5.5}$$

where σ_0 is the a-priori standard deviation. The minimum condition of the normal equation system by means of introducing the weighting matrix $\boldsymbol{P}$ reads

$$\mathbf{0} = \boldsymbol{A}^T\boldsymbol{P}\boldsymbol{A}\boldsymbol{x} - \boldsymbol{A}^T\boldsymbol{P}\boldsymbol{y} \ . \tag{5.6}$$

As a final outcome of the least squares adjustment, the estimated parameters are given by

$$\boldsymbol{x} = (\boldsymbol{A}^T\boldsymbol{P}\boldsymbol{A})^{-1}\boldsymbol{A}^T\boldsymbol{P}\boldsymbol{y} \ , \tag{5.7}$$

where $\boldsymbol{A}^T\boldsymbol{P}\boldsymbol{A}$ is the so called normal equation matrix $\boldsymbol{N}$ which is symmetric and of dimension $n \times n$. The number of estimation parameters is denoted as u. The adjusted parameters are achieved by

$$\boldsymbol{x}_1 = \boldsymbol{x}_0 + \boldsymbol{x} \ , \tag{5.8}$$

and the entire adjustment process is repeated iteratively until convergence of the estimated model parameters is ensured and the residuals are minimized. The stochastic attributes of the estimated model parameters can be calculated by an a-posteriori standard deviation

$$s_0 = \sqrt{\frac{\boldsymbol{\epsilon}^T\boldsymbol{P}\boldsymbol{\epsilon}}{n-u}} \tag{5.9}$$

where $n - u$ denotes the degree of freedom. That means: number of observations minus number of estimated parameters. In addition, the covariance and cofactor matrices $\boldsymbol{Q}_{xx}$ and $\boldsymbol{C}_{xx}$ can be calculated

$$\boldsymbol{Q}_{xx} = s_0^2\boldsymbol{C}_{xx} = s_0^2\boldsymbol{N}^{-1} \ . \tag{5.10}$$

In the following, this section will provide the mathematical background for orbit determination based on the least squares approach. The notation used is taken from *(Swatschina, 2012)* and *(Jäggi, 2007)*.

5.2 Equation of Motion

A satellite orbiting the Earth is affected by many forces. Theses forces are induced by the physical environment acting on the satellites body *(Jäggi, 2007)*. This process is mathematically described by the equation of motion which is a linear differential equation of second order. The equation represents a combination of the second Newtons axiom with the law of gravitation for point masses *(Swatschina, 2012)*. Expressed in an inertial system located on satellites center of mass, the equation of motion is given as

$$\ddot{\boldsymbol{x}}(t) = -\frac{GM}{r^3} \cdot \boldsymbol{x}(t) \ . \tag{5.11}$$

where

$\ddot{\boldsymbol{x}}(t)$ is the second derivative of the position or the acceleration,
$\boldsymbol{x}(t)$ is the position,
GM is the product of gravitational constant and Earth mass,
and r is the norm of the position.

In case of a point-like Earth gravity field and an infinitesimal satellite mass compared to the Earth mass Eq. 5.11 is valid. Furthermore, all non-gravitational forces are neglected. This equation represents the simplified concept and any analytical solution of the equation will turn out the shape of conic sections also referred to as Keplerian orbits *(Vallado, 2007)*.

A differential equation of second order can be solved by 6 constants of integration. In case of orbit determination, the use of 6 Keplerian elements is a well-known method. Using this common approach, the position and velocity can be calculated for any epoch *(Beutler, 2005)* or *(Vallado, 2007)*. The Keplerian elements shown in Fig. 5.1 are in particular

a: semi-major axis,
e: eccentricity,
i: inclination,
Ω: right ascension,
ω: argument of the perigee,
ν: true anomaly.

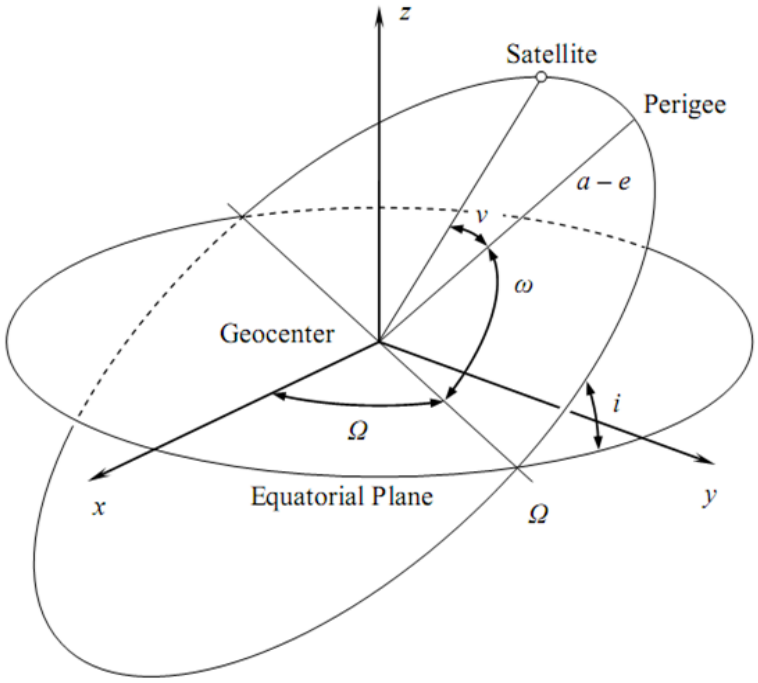

Figure 5.1: *Six Keplerian elements (Swatschina, 2012)*

If other forces acting on the satellite are taken into account additionally, the updated equation of motion reads

$$\ddot{\boldsymbol{x}}(t) = -\frac{GM}{r^3} \cdot \boldsymbol{x}(t) + \sum_i \ddot{\boldsymbol{x}}(t)_{perturb,i} \ . \tag{5.12}$$

The perturbation forces depend on position $\boldsymbol{x}$, velocity $\dot{\boldsymbol{x}}$, time t and on additional dynamical force model parameters $q_1 ... q_d$ *(Beutler, 2005)*. The initial conditions using Keplerian elements reads

$$\boldsymbol{x}(t) = \boldsymbol{x}(a, e, i, \Omega, \omega, \nu) \quad and \quad \dot{\boldsymbol{x}}(t) = \dot{\boldsymbol{x}}(a, e, i, \Omega, \omega, \nu) \ . \tag{5.13}$$

Inserting Eq. 5.13 in the equation of motion leads to

$$\ddot{\boldsymbol{x}}(t) = -\frac{GM}{r^3} \cdot \boldsymbol{x}(t) + \sum_i \ddot{\boldsymbol{x}}(t, \boldsymbol{x}, \dot{\boldsymbol{x}}, q_1 ... q_d)_{perturb,i} \ . \tag{5.14}$$

In addition to the initial conditions, these dynamic parameters are estimated during the adjustment. In general, the equation of motion will be solved by numerical

approaches. Examples of solving differential equations can be found in *(Beutler, 1990)*. The Bernese software package is based on the so-called collocation method *(Beutler, 2005)*. This method directly leads to a polynomial function of time instead of positions and is a very accurate and flexible numerical integrator *(Swatschina, 2012)*.

5.3 Force Model and Orbit Perturbations

The dynamic force model includes gravitational and non-gravitational forces. Both types of forces are responsible for the perturbations acting on the satellite and the type of perturbation physically induces a change in the satellite acceleration *(Swatschina, 2012)*. Hence, the force is denoted as acceleration in the following. The gravitational accelerations are induced by gravitational forces apart from the idealized point-like Earth concept. In literature, the gravitational and non-gravitational forces are often denoted as conservative and non-conservative forces or accelerations respectively. These accelerations have to be taken into account to ensure the most precise results in dynamic orbit modeling. In Tab. 5.1 the relevant gravitational accelerations acting on a LEO satellite are listed.

Table 5.1: *Gravitational perturbations for LEO satellites (Bock, 2003)*

Perturbation	**Acceleration** $[m/s^2]$
Two-body term	8.6
Inhomogeneous Earth gravity field	$1.5 \cdot 10^{-2}$
Oblateness of the Earth	$2.0 \cdot 10^{-2}$
Solid Earth tides	$1.5 \cdot 10^{-7}$
Polar tides	$1.5 \cdot 10^{-8}$
Ocean tides	$5.0 \cdot 10^{-8}$
Lunar gravitational attraction	$5.5 \cdot 10^{-6}$
Solar gravitational attraction	$5.0 \cdot 10^{-7}$
General relativity	$5.0 \cdot 10^{-9}$
Attraction of other planets	$1.0 \cdot 10^{-10}$

The non-gravitational forces are depending on the area-to-mass ratio of the individual spacecraft. The shape and the flight direction of the satellite are important, too. The magnitude of the force component is directly proportional to the surface

area of the spacecraft seen from a certain direction *(Feltens, 1991)*. The most important non-gravitational accelerations are listed in Tab. 5.2.

Table 5.2: *Non-gravitational perturbations for LEO satellites (Bock, 2003)*

Perturbation	**Acceleration** $[m/s^2]$
Atmospheric drag	$5.0 \cdot 10^{-7}$
Solar radiation pressure	$3.0 \cdot 10^{-8}$
Albedo	$4.0 \cdot 10^{-10}$

The strong dependency of the dynamic orbit modeling on the quality of the applied force model and the chosen orbit integrator is a drawback. This approach of modeling is always limited to rather short arcs because there are forces which can not be modeled sufficiently or accurately enough. As an example, the atmospheric drag as a non-gravitational acceleration could not be modeled very accurately due to the lack of knowledge of the atmospheric density and its variation with time and location *(Swatschina, 2012)*. The solution to this problem by adding empirical parameters to the dynamic model is discussed later in the reduced-dynamic orbit section 5.6. For a detailed description of gravitational and non-gravitational accelerations, the reader is referred to excellent literature e.g. *(Swatschina, 2012)*, *(Jäggi, 2007)*, *(Beutler, 2005)* or *(Bock, 2003)* where a precise mathematical description is given.

As an important pre-requirement for solving the non-linear differential equation system as given in Eq. 5.12, the linearized form by partial derivatives of all force components with respect to the spacecrafts position and velocity have to be formed *(Swatschina, 2012)*. Afterwards, this linearized form is provided to the orbit integrator method. The same linearizations are available for solving the variational equations but in addition the dependency to the dynamical parameters is required. The particular partial derivatives can be found in e.g. *(Swatschina, 2012)*.

5.4 Variational Equations

The variational equations approach is besides from the energy integral, the short arc, the acceleration and the celestial mechanics approach the most prominent

method for solving the equation of motion. A comparison between these different approaches can be found in *(Baur et al, 2014)*. However, variational equations are implemented in the Bernese GNSS software package, thus, they are discussed in more detail.

The partial derivatives of the a-priori orbit with respect to the estimated parameters are needed to adjust the orbit to the observations in a least squares sense *(Swatschina, 2012)*. The solution of the equation of motion (see Eq. 5.14) is determined by the initial conditions and force model parameters. Assuming P_i as one of these dynamical parameters, the derivative of the a-priori orbit $\boldsymbol{x}(t)$ is given by

$$\boldsymbol{z}_{P_i} \equiv \frac{\partial \boldsymbol{x}(t)}{\partial P_i} \ , \tag{5.15}$$

where

$$P_i \in (p_1, p_2, ...p_6, q_1...q_d). \tag{5.16}$$

As mentioned above, the equation of motion needs to be solved numerically. Hence, the differential equations system describing the relation between the orbit parameter and the accelerations can be differentiated with respect to the orbit parameters P_i *(Jäggi, 2007)*. This step converts the equation of motion to the variational equation

$$\ddot{\boldsymbol{z}}_{P_i} = \boldsymbol{A}_0 \cdot \boldsymbol{z}_{P_i} + \boldsymbol{A}_1 \cdot \dot{\boldsymbol{z}}_{P_i} + \frac{\partial \ddot{\boldsymbol{x}}_{perturb}}{\partial P_i} \ , \tag{5.17}$$

with the 3 x 3 Jacobian matrices $\boldsymbol{A}_0$ and $\boldsymbol{A}_1$ defined as

$$\boldsymbol{A}_{0,[j,k]} = \boldsymbol{A}_{0,[j,k]}(t, \boldsymbol{x}, \dot{\boldsymbol{x}}) = \frac{\partial \boldsymbol{f}_j}{\partial \boldsymbol{x}_k} \quad j,k = 1,2,3 \ , \tag{5.18}$$

$$\boldsymbol{A}_{1,[j,k]} = \boldsymbol{A}_{1,[j,k]}(t, \boldsymbol{x}, \dot{\boldsymbol{x}}) = \frac{\partial \boldsymbol{f}_j}{\partial \dot{\boldsymbol{x}}_k} \quad j,k = 1,2,3 \ . \tag{5.19}$$

The variational equations (5.17) is a linear homogeneous differential equation system of second order. The initial values are given by

$$\boldsymbol{z}_{P_i} \neq 0 \text{ and } \dot{\boldsymbol{z}}_{P_i} \neq 0 \quad P_i \in (a, e, i, \Omega, \omega, \nu) \;, \tag{5.20}$$

where the homogeneous character holds for the initial parameter. In contrast, for the dynamical parameters $P_i \in (q_1 ... q_d)$ the system in Eq. 5.17 is inhomogeneous but has zero initial values because the initial satellite state does not depend on the force model *(Jäggi, 2007)*. Finally, the Bernese software requires linear differential equations for the collocation orbit integration method *(Beutler, 1990)*.

5.5 Kinematic Orbit Determination

The determination of a spacecrafts orbit can be carried out by using the (reduced)-dynamic or kinematic approach. The kinematic approach is purely geometrical and independent from the knowledge about the satellite dynamics (e.g. gravity field or atmospheric drag). This is a special need for gravity field determination e.g. *(Mayer-Gürr, 2006)*, *(Mayer-Gürr et al, 2012a)*, or *(Mayer-Gürr et al, 2012b)*.

Basically, the kinematic orbit determination is based on three independent LEO coordinates plus the LEO clock parameter at every observation epoch for each satellite-receiver combination. These are the epoch dependent 4×4 blocks in the main diagonal of the normal equation matrix $\boldsymbol{N}$ (see sec. 5.1). In case of carrier phase measurement, ambiguities must be considered additionally. The epoch independent ambiguities are set up for every carrier phase L_1 and L_2 and for each continuous track of the satellite. In addition, antenna or transmitter phase center variations can set up epoch independently. *(Svehla and Rothacher, 2005)*. The normal equation system in case of the zero-difference kinematic approach looks like it is shown in Fig. 5.2.

However, due to the lack of the knowledge of the satellites dynamics this approach in not appropriate for the determination of the GNSS-RO orbital arcs. The characteristics of different orbit solutions including the kinematic orbit can be seen in Fig. 5.3. During the Bernese POD processing the kinematic orbits are used to compute a first initial solution. Furthermore, the finally achieved kinematic orbit is used for a comparison with the corresponding reduced-dynamic solution. More information on this topic can be found in section 5.9.

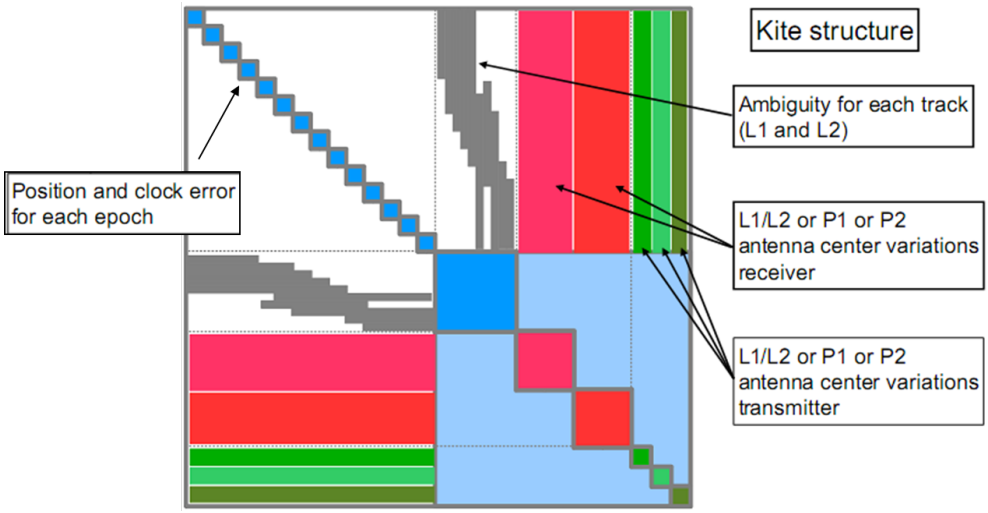

Figure 5.2: *Normal equation system (Zehentner and Mayer-Gürr, 2013)*

5.6 Dynamic and Reduced-Dynamic Orbit Determination

The main difference between reduced and reduced-dynamic orbit modeling is the flexibility of the dynamic force model by set up of additional parameters in the least squares estimation process. The reduced-dynamic approach was introduced for the first time by *(Wu et al, 1991)*. Hereby the orbit model (5.14) is parametrized by

$$\ddot{\boldsymbol{x}}(t) \equiv \boldsymbol{f}(t, p_1, p_2..., p_6, q_1, q_2, ..., q_d) + \boldsymbol{f}_1(a_1, ..., a_n) \ , \tag{5.21}$$

with the newly introduced parameters $a_1, ..., a_n$ to be determined additionally within the least squares adjustment. The trajectory can therefore be appropriately fitted to the observation data while the highest amount of dynamic information is remaining during the estimation process *(Swatschina, 2012)*. To prevent the trajectory from divergence (see Fig. 5.5) a realistic set of a-priori parameters and constraints have to be introduced. The common approach is to use a-priori stochastic properties like expectation values or weightings *(Montenbruck et al, 2005)*. If exactly these parameters are applied pseudo-stochastic parameters are depicted.

The pseudo-stochastic orbit differs from stochastic orbit modeling. The latter is characterized by the fact that the spacecraft trajectory is modeled by a solution of stochastic differential equations *(Jazwinski, 1970)*. In contrast, pseudo-stochastic modeling introduces additional parameters into the estimation process. On the one

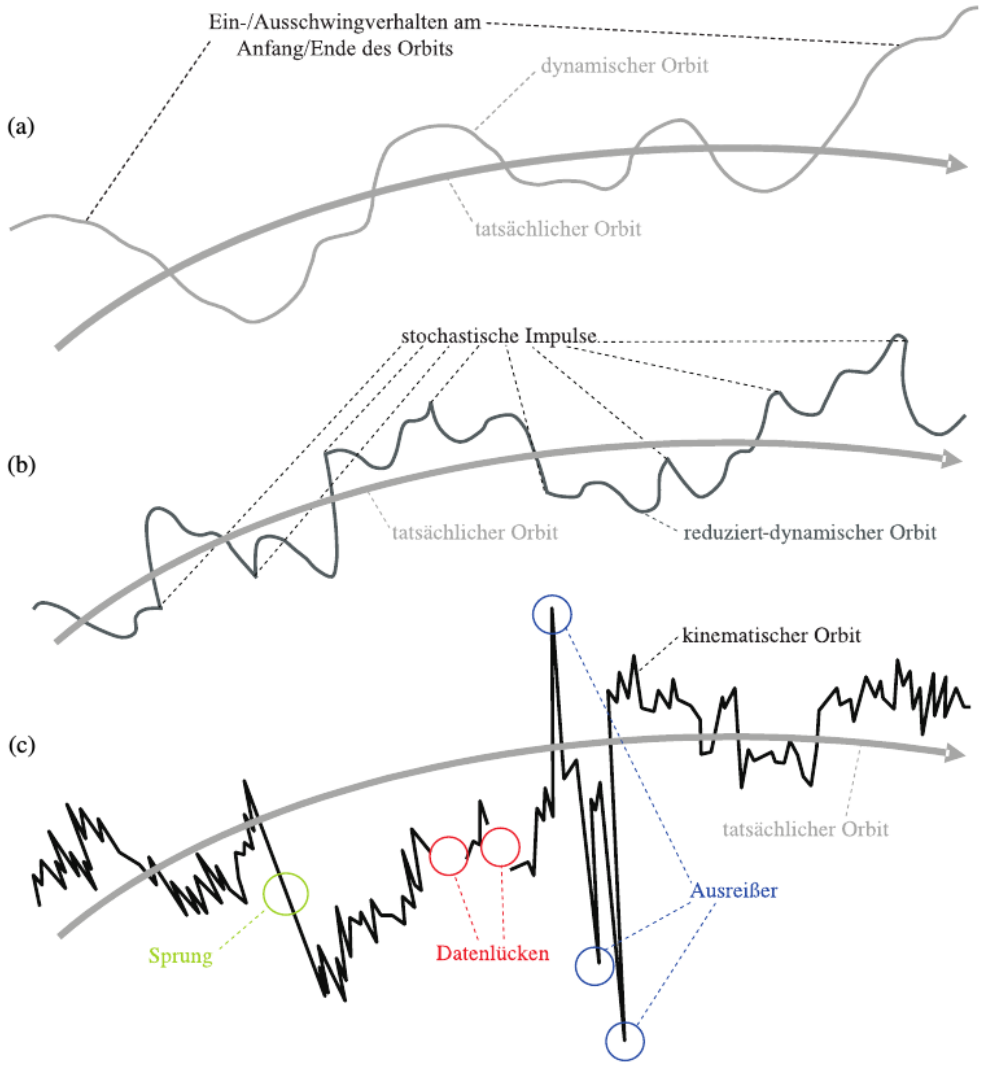

Figure 5.3: *Three different orbit types: (a) dynamic orbit, (b) reduced-dynamic orbit and (c) kinematic orbit (Reubelt, 2009)*

hand, a huge number of these parameters can be introduced which leads to an attenuation of the dynamics on the other hand, an increase in the weighting preserves the influence of the dynamic model *(Swatschina, 2012)*. This is often denoted as highly reduced-dynamic orbit modeling *(Jäggi, 2007)*. Theoretically, if an infinite number of unconstrained parameters is introduced, the restraint of the dynamics vanishes and the solution coincides with the kinematic model. This means that any type of orbit can be approximated by the pseudo-stochastic approach *(Jäggi et al, 2006)*, and is illustrated in Fig. 5.4. Examples of several pseudo-stochastic force models can be found in *(Jäggi, 2007)*.

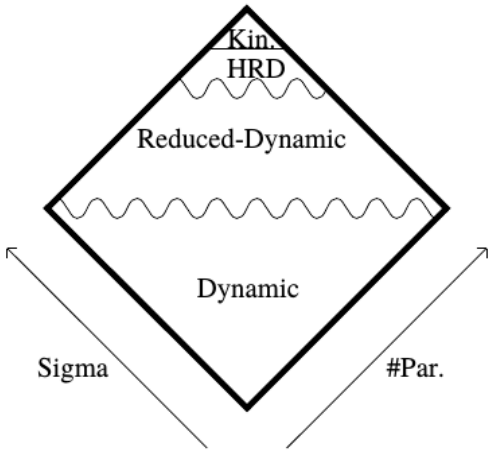

Figure 5.4: *Dynamic, reduced-dynamic, highly reduced-dynamic and kinematic orbit determination as function of parameters and a-priori sigma of the estimated pseudo-stochastic parameters (Jäggi, 2007)*

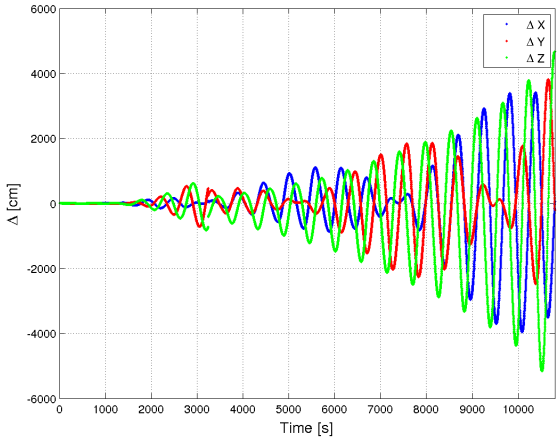

Figure 5.5: *Dynamic orbits tend to diverge over time (sampling rate of the example: 10 seconds)*

In the following, two realizations, namely the concepts of pseudo-stochastic pulses and piece-wise constant acceleration are discussed. The latter is used within this research for the reduced-dynamic orbit determination with the Bernese GNSS software. These two sets of empirical parameters are highly suitable to overcome the deficits of the deterministic force model. The difference between these two sets of empirical parameters is revealed on the velocity level. The pulse solution shows discontinuities in the velocities. From a physical point of view, the more realistic approach is based on piece-wise constant accelerations because the discontinuities are transferred to the acceleration level *(Beutler, 2005)*.

5.6.1 Pseudo-Stochastic Pulses

Sudden changes in the direction and magnitude of satellites velocities between particular epochs can be used to compensate the imperfect modeling of the dynamics by continuously re-adjusting the satellites track *(Swatschina, 2012)*. The orbit characteristics based on pseudo-stochastic pulses can be described as *(Bock, 2003)*

- each resulting orbit or arc is continuous,
- at pre-determined epochs the orbit is allowed to suffer velocity changes v_i in pre-determined directions i,
- pseudo-stochastic pulses v_i are parameters of the least squares adjustment,
- each pseudo-stochastic pulse is characterized by an a-priori variance.

The immediate velocity changes are a consequence of the pseudo-stochastic pulses *(Beutler et al, 1994)*. The pulses are usually set up in the radial, along and out-of-plane direction in pre-defined epochs with a uniform spacing (e.g. every 30 minutes) or at epochs which correspond to orbit maneuvers. This is especially the case for GNSS satellites to overcome the insufficient solar radiation pressure modeling *(Swatschina, 2012)*. Therefore, one set of pulses is introduced per day. In between, the orbit is described by the deterministic equation of motion (see Eq. 5.14). This concept is illustrated in Fig. 5.6.

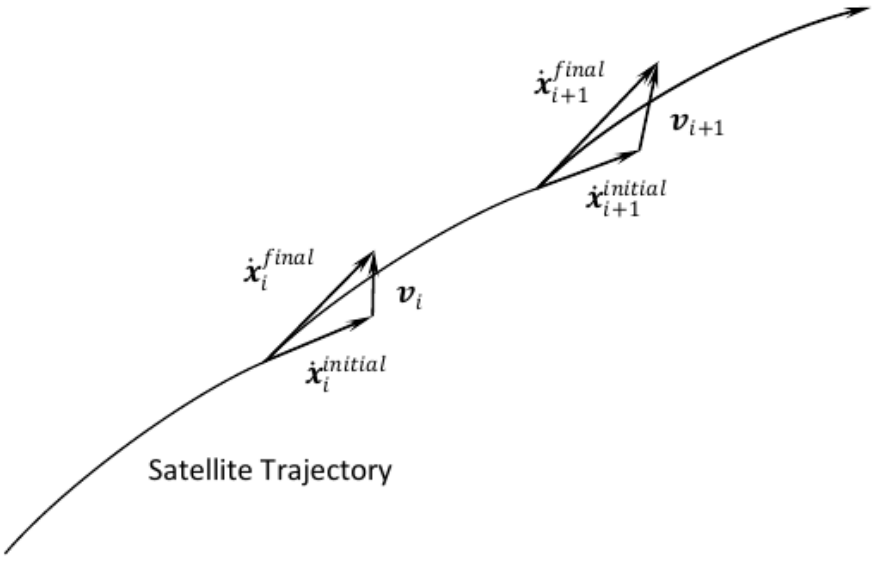

Figure 5.6: *Pseudo-stochastic pulses (Swatschina, 2012)*

Following the notation of *(Swatschina, 2012)* - if for example three pulses

$$v_{i,j} \; with \; i = 1, ..., n-1; \; j = 1, 2, 3, \tag{5.22}$$

are set-up at pre-defined epochs t_i in the current direction $\boldsymbol{e}_j(t_i)$, the equation of motion reads

$$\ddot{\boldsymbol{x}}(t) = \boldsymbol{f}(t, p_1, p_2 ....p_6, q_1 ..., q_d) + \sum_{i=1}^{n-1} \sum_{j=1}^{3} v_{i,j} \cdot \delta(t - t_i) \cdot \boldsymbol{e}_j(t_i) \; , \tag{5.23}$$

where $\delta(t)$ represents Dirac's delta function *(Jäggi et al, 2006)*. The variational equation for one single component of the pulse reads

$$\ddot{\boldsymbol{z}}_{v;i,j} = \boldsymbol{A}_0 \cdot \boldsymbol{z}_{v;i,j} + \boldsymbol{A}_1 \cdot \dot{\boldsymbol{z}}_{v;i,j} + \delta(t - t_i) \cdot \boldsymbol{e}_j(t_i) \; . \tag{5.24}$$

The solution of the variational equation for any pulse $v_{i,j}$ may be written as a linear combination of the 6 solutions $\boldsymbol{z}_{p,k}$, $k = 1, ...6$, referring to the initial conditions p_k *(Beutler et al, 2006)*. Therefore, the solution of Eq. 5.24 reads

$$\boldsymbol{z}_{v;i,j}(t) = \begin{cases} \boldsymbol{0} & t < t_i \\ \sum\limits_{k=1}^{6} \beta_{i,j;k} \cdot \boldsymbol{z}_{pk}(t) & t \geq t_i \; , \end{cases} \tag{5.25}$$

where the coefficients $\beta_{i,j;k}$ are obtained from the conditions

$$\boldsymbol{z}_{v;i,j}(t_i) = \boldsymbol{0} \quad and \quad \dot{\boldsymbol{z}}_{v;i,j}(t_i) = \boldsymbol{e}_j(t_i) \; , \tag{5.26}$$

and the partial derivations $\boldsymbol{z}_{v;i,j}$ are computed only for the variational equations with respect to the the initial conditions *(Swatschina, 2012)*. The resulting equation systems and formed linear combinations can be found in *(Jäggi, 2007)* or *(Swatschina, 2012)*.

However, by introducing sub-intervals $[t_i, t_{i+1}]$ *(Beutler et al, 2006)*, the correction equation of the least squares approach reads

$$\boldsymbol{A}_i \cdot \Delta\boldsymbol{p} + \boldsymbol{A}_i \cdot \sum_{m=1}^{i} \boldsymbol{B}_m \cdot \Delta\boldsymbol{v}_m - \boldsymbol{y}_i = \boldsymbol{\epsilon}_i \ . \tag{5.27}$$

For the entire observations system, the correction equations dividend in sub-intervals $[t_i, t_{i+1}]$ with $i = 0...n-1$, can be written in matrix-vector notation

$$\boldsymbol{\epsilon} = \begin{bmatrix} \boldsymbol{A}_0 & \boldsymbol{0} & \boldsymbol{0} & \cdots & \boldsymbol{0} \\ \boldsymbol{A}_1 & \boldsymbol{A}_1\boldsymbol{B}_1 & \boldsymbol{0} & \cdots & \boldsymbol{0} \\ \boldsymbol{A}_2 & \boldsymbol{A}_2\boldsymbol{B}_1 & \boldsymbol{A}_2\boldsymbol{B}_2 & \cdots & \boldsymbol{0} \\ \vdots & \vdots & \vdots & \ddots & \vdots \\ \boldsymbol{A}_{n-1} & \boldsymbol{A}_{n-1}\boldsymbol{B}_1 & \boldsymbol{A}_{n-1}\boldsymbol{B}_2 & \cdots & \boldsymbol{A}_{n-1}\boldsymbol{B}_{n-1} \end{bmatrix} \cdot \begin{bmatrix} \Delta\boldsymbol{p} \\ \Delta\boldsymbol{v}_1 \\ \Delta\boldsymbol{v}_2 \\ \vdots \\ \Delta\boldsymbol{v}_{n-1} \end{bmatrix} - \boldsymbol{y} \ . \tag{5.28}$$

Finally, the resulting normal equation system is of dimension $d = 6 + 3 \cdot (n-1)$. This is described in more detail by *(Swatschina, 2012)*.

As mentioned above, the empirical parameters can be constrained. A common approach is to introduce a-priori standard deviations in the weighting scheme to constrain the parameters to pre-defined values *(Beutler et al, 2006)*. Following the publication of *(Beutler et al, 2006)*, artificial observations which directly measure the pulses are given by

$$\boldsymbol{v}_i = \boldsymbol{0} \quad i = 0, ..., n-1, \tag{5.29}$$

and the weighting matrix $\boldsymbol{P}$ is the inverse covariance matrix for these parameters

$$\boldsymbol{P}_i = \sigma_0^2 \cdot \boldsymbol{Q}_{vi}^{-1} \begin{bmatrix} \frac{\sigma_0^2}{\sigma_1^2} & 0 & 0 \\ 0 & \frac{\sigma_0^2}{\sigma_2^2} & 0 \\ 0 & 0 & \frac{\sigma_0^2}{\sigma_3^2} \end{bmatrix} \qquad i = 0, ...n-1, \tag{5.30}$$

where σ_0 is the a-priori standard deviation, $\boldsymbol{Q}_{vi}$ is the covariance matrix of the parameters and σ_k, $k = 1, 2, 3$ are pre-defined standard deviations of the three components of $\boldsymbol{v}_i$ *(Swatschina, 2012)*. The normal equation system includes the constraints and is set up for the initial conditions and the pseudo-stochastic pulses. Furthermore, dynamical parameters or clock offsets as well as ambiguities are incorporated within the least squares approach.

However, the main focus of this thesis is on the piece-wise constant accelerations approach which is used for LEO orbit determination. The following section describes this approach in more detail.

5.6.2 Piece-wise Constant Accelerations

As mentioned above, the use of pulses to overcome the imperfect modeled forces is suitable for GNSS satellites but inappropriate for LEO missions. The pulses cause discontinuities and undifferentiabilities at the velocity level *(Gerlach et al, 2003)*. Therefore, the concept of stochastic pulses was advanced to piece-wise constant accelerations by a refinement of the empirical parametrization *(Jäggi et al, 2005)*. By introducing one parameter in addition to each position component, the model allows for upgrading from pulses to piece-wise constant accelerations *(Swatschina, 2012)*.

The resulting trajectory is more realistic because the occurring discontinuities are shifted to the acceleration level. The introduced empirical accelerations are constant over pre-defined epochs in pre-defined directions, e.g. along, across and out-of-plane which is similar to the pulses approach *(Jäggi et al, 2005)*. The concept of pseudo-stochastic orbit modeling with piece-wise constant accelerations is illustrated in Fig. 5.7.

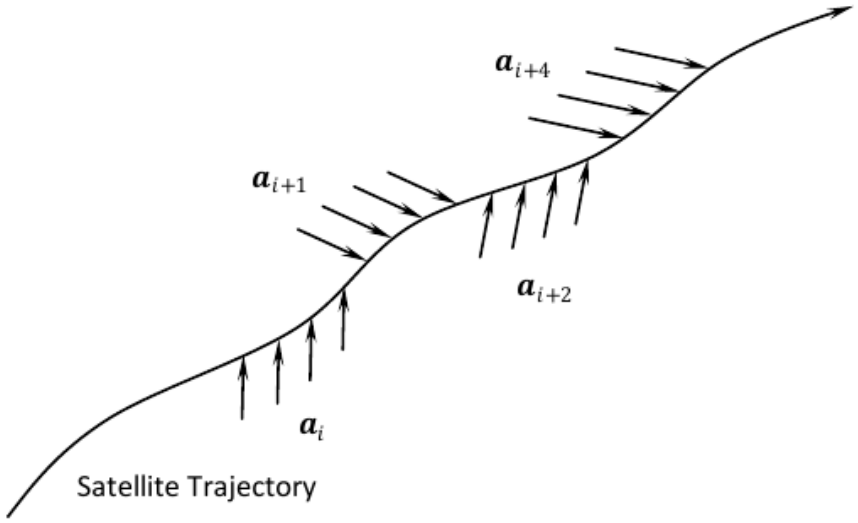

Figure 5.7: *Pseudo-stochastic piece-wise constant accelerations (Swatschina, 2012)*

The mathematical concept is explained in the following. Based on *(Swatschina, 2012)*, let us assume three constant accelerations

$$a_{i,j} \; with \; i = 1, ..., n-1; \; j = 1, 2, 3, \tag{5.31}$$

are set up within the time interval $[t_i, t_{i+1}]$ in three pre-defined directions $\boldsymbol{e}_j(t)$, *(Jäggi et al, 2005)*. The resulting equation of motion can be written as

$$\ddot{\boldsymbol{x}}(t) = \boldsymbol{f}(t, p_1, p_2 .... p_6, q_1 ..., q_d) + \sum_{i=1}^{n-1} \sum_{j=1}^{3} a_{i,j} \cdot \xi_i(t) \cdot \boldsymbol{e}_j(t) \; , \tag{5.32}$$

with ξ_i defined as

$$\xi_i(t) = \begin{cases} 0 & t < t_i \\ 1 & t_i \leq t < t_{i+1} \\ 0 & t_{i+1} \leq t \; . \end{cases} \tag{5.33}$$

Taking a particular acceleration $a_{i,j}$ into account, the variational equation reads

$$\ddot{\boldsymbol{z}}_{a;i,j} = \boldsymbol{A}_0 \cdot \boldsymbol{z}_{a;i,j} + \boldsymbol{A}_1 \cdot \dot{\boldsymbol{z}}_{a;i,j} + \xi_i(t) \cdot \boldsymbol{e}_j(t) \; . \tag{5.34}$$

The solution of the variational equation using accelerations can again be written as a linear combination in the same way as for the stochastic pulses *(Beutler et al, 2006)*. The partial derivatives solving equation 5.34 are given as

$$\boldsymbol{z}_{a;i,j} = \begin{cases} \boldsymbol{0} & & & t < t_i \\ \sum\limits_{k=1}^{6} & \beta_{i,j;k}(t) \cdot \boldsymbol{z}_{pk}(t) = \tilde{\boldsymbol{z}}_{a;i,j} & & t_i \leq t < t_{i+1} \\ \sum\limits_{k=1}^{6} & \beta_{i,j;k}(t_i) \cdot \boldsymbol{z}_{pk}(t) = \sum\limits_{k=1}^{6} & \beta_{i,j;k} \cdot \boldsymbol{z}_{pk}(t) & t_{i+1} \leq t \; . \end{cases} \tag{5.35}$$

As shown in *(Jäggi et al, 2005)*, the solution for $\beta_{ij,k}$ claims additional partial derivatives with respect to the accelerations.

By means of the least squares approach, the correction equation of the normal equation system for piece-wise constant accelerations after grouping them into sub-intervals can be written as

$$\boldsymbol{A}_i \cdot \Delta\boldsymbol{p} + \boldsymbol{A}_1 \cdot \sum_{m=0}^{i-1} \boldsymbol{B}_{m+1} \cdot \Delta\boldsymbol{a}_m + \tilde{\boldsymbol{A}}_i \cdot \Delta\boldsymbol{a}_i - \boldsymbol{y}_i = \boldsymbol{\epsilon}_i \ , \tag{5.36}$$

with the sub-intervals $[t_i, t_{i+1}]$ for $i = 0, ...n-1$, analogously to the stochastic pulses *(Jäggi et al, 2005)*. The matrix $\tilde{\boldsymbol{A}}_i$ denotes the partial derivatives of the observations. The matrix $\boldsymbol{B}_i$ contains the constant parameters $\beta_{i,j;k}$ which are obtained by computation of $\boldsymbol{z}_{a;i,j}$ at epoch $[t_{i-1}, t_i]$ *(Swatschina, 2012)*. Those parameters are different compared to the stochastic pulses approach. The set of correction equations given in matrix-vector notation reads

$$\boldsymbol{\epsilon} = \begin{bmatrix} \boldsymbol{A}_0 & \tilde{\boldsymbol{A}}_0 & \boldsymbol{0} & \cdots & \boldsymbol{0} & \boldsymbol{0} \\ \boldsymbol{A}_1 & \boldsymbol{A}_1\boldsymbol{B}_1 & \tilde{\boldsymbol{A}}_1 & \cdots & \boldsymbol{0} & \boldsymbol{0} \\ \boldsymbol{A}_2 & \boldsymbol{A}_2\boldsymbol{B}_1 & \boldsymbol{A}_2\boldsymbol{B}_2 & \cdots & \boldsymbol{0} & \boldsymbol{0} \\ \vdots & \vdots & \vdots & \ddots & \vdots & \vdots \\ \boldsymbol{A}_{n-2} & \boldsymbol{A}_{n-2}\boldsymbol{B}_1 & \boldsymbol{A}_{n-2}\boldsymbol{B}_2 & \cdots & \tilde{\boldsymbol{A}}_{n-2} & \boldsymbol{0} \\ \boldsymbol{A}_{n-1} & \boldsymbol{A}_{n-1}\boldsymbol{B}_1 & \boldsymbol{A}_{n-1}\boldsymbol{B}_1 & \cdots & \boldsymbol{A}_{n-1}\boldsymbol{B}_{n-1} & \tilde{\boldsymbol{A}}_{n-1} \end{bmatrix} \cdot \begin{bmatrix} \Delta\boldsymbol{p} \\ \Delta\boldsymbol{a}_0 \\ \Delta\boldsymbol{a}_1 \\ \Delta\boldsymbol{a}_2 \\ \vdots \\ \Delta\boldsymbol{a}_{n-1} \end{bmatrix} - \boldsymbol{y} \tag{5.37}$$

The resulting normal equation system in of dimension $d = 6 + 3 \cdot n$ and can be found in *(Beutler et al, 2006)*. The constraints are again introduced analogously as for the stochastic pulses described in section 5.6.1 by an a-priori weighting scheme.

5.7 Orbit Determination using Bernese GNSS Software

For the estimation of the final orbits and velocities for the excess phase computation, the latest version of the Bernese GNSS software has been used. This software allows for efficient computation of LEO orbits and clock corrections as well as many other scientific applications. The estimation process is based on the least squares approach, which is briefly explained in section 5.1.

Running the first orbit determination with own data sets may lead to some errors in the processing. This is due to the fact that the software is tailored to the processing examples. Most of the errors are caused by insufficient initialization and can be overcome by simply increasing the number of the initialized variables to a higher value and re-compilation. Note that both the station and the receiver files are case sensitive. For example, the receiver type might be defined in the receiver file but not exactly match with the notation of the receiver defined in the station file. Another excellent source for troubleshooting can be found at the FAQ page[1] of the Bernese GNSS software. As general information, a very detailed software user manual is provided on the website[2], *(Dach et al, 2007)* or *(Dach et al, 2013)*.

5.7.1 LEO POD Processing Description

The chosen processing strategy is similar to the approaches of the established analysis centers CODE and UCAR and is shown at a glance in Fig. 5.8. Based on precise input data provided by external sources, this data is in a first step being prepared for the Bernese software. The input data consist of

- Precise GNSS orbits and Earth rotation parameters (ERP),
- GNSS clock corrections and differential code biases (DCB),
- LEO satellite phase L_1, L_2 and code P_1 , P_2 GNSS measurements,
- LEO satellite attitude quaternion data,
- Bernese GNSS satellite status file.

Afterwards, a first solution is computed based only on code measurements. During the iterative screening of the phase measurements an improved orbit result

[1] http://www.bernese.unibe.ch/faq/
[2] http://www.bernese.unibe.ch/

is achieved. Based on this orbit, the kinematic and reduced-dynamic orbits are computed afterwards. In case of reduced-dynamic orbit determination, an orbit model is introduced which replaces the epoch-wise coordinates by state dynamic and pseudo-stochastic parameters to be estimated by a least squares approach *(Swatschina, 2012)*. The dynamic model state usually consists of

- 6 osculation elements (Keplerian elements),
- 3-9 radiation pressure acceleration terms,
- pseudo-stochastic parameters (piece-wise constant empirical accelerations) every 6 minutes.

This leads to 720 empirical parameters per day. The perturbing accelerations are modeled additionally in the equation of motion. This includes the EGM2008 *(Pavlis et al, 2008)* up to d/o 120, third body tidal accelerations due to sun and moon as well as solid Earth and ocean tides up to d/o 50. For all observations an elevation cut-off angle of 5° is introduced.

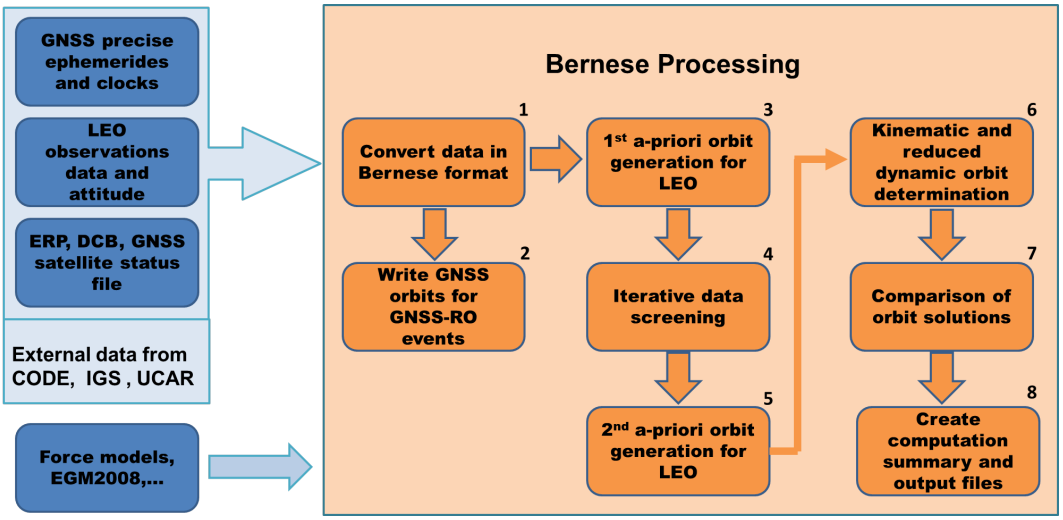

Figure 5.8: *Orbit processing scheme of this study*

In the next step, the two orbit solutions are compared. This is only possible if a final kinematic solution could be obtained from the data which is not always the case, especially for the FORMOSAT-3/COSMIC mission. The last step consists of writing the desired output products as orbits and clock offsets, residuals, or covariance information to the output files. Note that for all investigated satellite missions the data screening process remains the same. Nevertheless, the chosen processing strategy seems highly capable for precise orbit determination.

5.7.2 Set-Up Bernese for POD

This section describes the settings used for the POD processing. This is an important task because the achieved quality depends directly on it.

Antenna Offsets

The knowledge of the different satellite instrument offsets is essential for POD. These values must be provided to the software a-priori and are finally added to the estimated orbits. This is due to the fact that the estimated orbit positions are related to the center of mass of the spacecraft and not to the position of the GNSS antenna. The positions of the navigation GNSS antenna expressed in the body fixed system are shown in Tab. 5.3. For the FORMOSAT-3/COSMIC mission (FM1-FM6) on each satellite, two POD antennas (POD1 and POD2) are available.

All offsets are assumed to be constant during mission lifetime. This also holds for the center of mass of the satellite which indeed can be slightly varying caused by fuel consumption of the satellites thrusters. It has to be mentioned that also for the GNSS satellites, a center of mass correction must be applied. This correction depends on the individual satellite tranche. In Tab. 5.3 the constant offsets are shown. Note that UCAR and EUMETSAT use different offset values for MetOp-A. In Tab. 5.3 the EUMETSAT values can be seen.

The corresponding small phase center offsets of the antennas are shown in Tab. 5.4. These offsets depend on the two carrier phase frequencies.

In addition, the Phase Center Variations (PCV) should be applied. The variation values can be estimated by processing a long time span based on the observation residuals. For more information on this topic see *(Jäggi et al, 2009)*. Another approach using radial basis functions for PCV estimation can be found in *(Zehentner and Mayer-Gürr, 2013)*.

The values for the occultation antennas (OCC) can be found in the satellite information file[3] of the Bernese software. Note that for the occultation antennas no phase center variations are available.

[3] C:/BERN52/GPS/GEN/SATELLITE.

Table 5.3: *Important LEO POD antenna offsets*

Satellite	$\boldsymbol{x}_{body}$ [m]	$\boldsymbol{y}_{body}$ [m]	$\boldsymbol{z}_{body}$ [m]
CHAMP	-1.4880	0.0000	-0.3928
GRACE-A	-0.004	-0.0004	-0.4514
MetOp-A	1.1410	0.0800	-0.8980
FM1 POD1	-0.4741	0.0052	-0.2605
FM1 POD2	0.4681	0.0048	-0.2565
FM2 POD1	-0.4735	0.0046	-0.2603
FM2 POD2	0.4689	0.0047	-0.2559
FM3 POD1	-0.4739	0.0043	-0.2598
FM3 POD2	0.4682	0.0047	-0.2547
FM4 POD1	-0.4746	0.0045	-0.2597
FM4 POD2	0.4680	0.0048	-0.2554
FM5 POD1	-0.4746	0.0052	-0.2598
FM5 POD2	0.4675	0.0050	-0.2556
FM6 POD1	-0.4744	0.0049	-0.2606
FM6 POD2	0.4678	0.0042	-0.2557

Receiver Implementation

Not all receiver types are pre-defined in the Bernese software. For the investigated satellite missions the following receiver and antenna types are added additionally to the station information file[4]. Also the satellites abbreviations and the type of processing (spaceborne) can be defined there. An overview about the implemented instruments is given in Tab. 5.5.

The corresponding GPS or GNSS frequencies are added to the corresponding receiver information file[5]. The type of single or dual frequency receiver is also defined in this file.

[4] C:/CAMPAIGN52/CAMNAME/STA/STATIONFILENAME.STA
[5] C:/BERN52/GPS/GEN/RECEIVER.

Table 5.4: *Important LEO POD phase center offsets*

Satellite	north [mm]	east [mm]	up [mm]
CHAMP - L1	1.49	0.60	-7.01
CHAMP - L2	0.96	0.86	22.29
GRACE-A - L1	1.49	0.60	-7.01
GRACE-A - L2	0.96	0.86	22.29
MetOp-A - L1	-47.40	-47.40	1.20
MetOp-A - L2	47.40	47.40	6.30
FM POD1 - L1	-34.50	-1.60	59.80
FM POD1 - L2	-39.70	4.20	71.30
FM POD2 - L1	-29.90	1.90	59.80
FM POD2 - L2	-35.10	-3.90	71.40

Table 5.5: *Implemented LEO instruments*

Satellite	**Receiver**	**Antenna**
CHAMP	BlackJack	Dorne Margolin
GRACE-A	BlackJack	GRCA
MetOp-A	GRAS	GRAS POD (GZA)
FM POD1	IGOR	HAIGH-FARR (POD1)
FM POD2	IGOR	HAIGH-FARR (POD2)

Station File Preparation

The station file is the centerpiece of the computation. It provides information about the satellites, the used receiver and antenna definitions as well as the processing types. The satellites abbreviations during the entire orbit computation process and many other meaningful information are defined there, too.

5.8 Bernese Processing Engine (BPE)

The BPE is a powerful tool for the automatization of the whole orbit processing. It allows to tailor processing sequences and may be used to perform all orbit depending tasks *(Dach et al, 2007)*. Furthermore, new processing sequences can be defined, user scripts may be included or adapted, quality reports and processing summaries can be retrieved. The BPE processing tasks are defined by the user in so-called Process Control Files (PCF). An example of the PCF for LEO missions is provided within this section. Note that the BPE can be either used with a Graphical User Interface (GUI) or batch processing.

5.8.1 Preparing BPE for Different LEO Missions

The given process control file "LEOPOD.PCF" for BPE processing (see Fig. 5.9) is originally tailored to the GRACE mission. Hence, it must be adapted in order to perform highly accurate orbit computation with other LEO satellite missions. Therefore, some input scripts within the PCF are changed. It is also important to change the corresponding BPE server variables (see Fig. 5.10). This set of global variables controls many important sequences and allows for individual settings. As an example, the sampling rate of the input observations or the user defined cut off angle can be defined there.

5.8.2 Convert Data in Bernese Format

The external precise GNSS ephemerides, clock corrections, Earth rotation parameters and the LEO observations cannot be directly used for the orbit processing. Different format conversions performed with the Bernese software package make them ready to use. In a first step, the GNSS data given in SP3-c format is converted to Bernese standard format using a sequence of programs and transformations (see sec. 5.8.3). Afterwards, the LEO observations usually given in RINEX format are separated to code and phase measurements and transformed into Bernese binary format. This also holds for the Earth rotation parameters. Only the LEO satellites attitude is ready to use if the data is given in form of quaternions. The used programs for format converting can be found in the corresponding PCF files and are described in section 5.9.

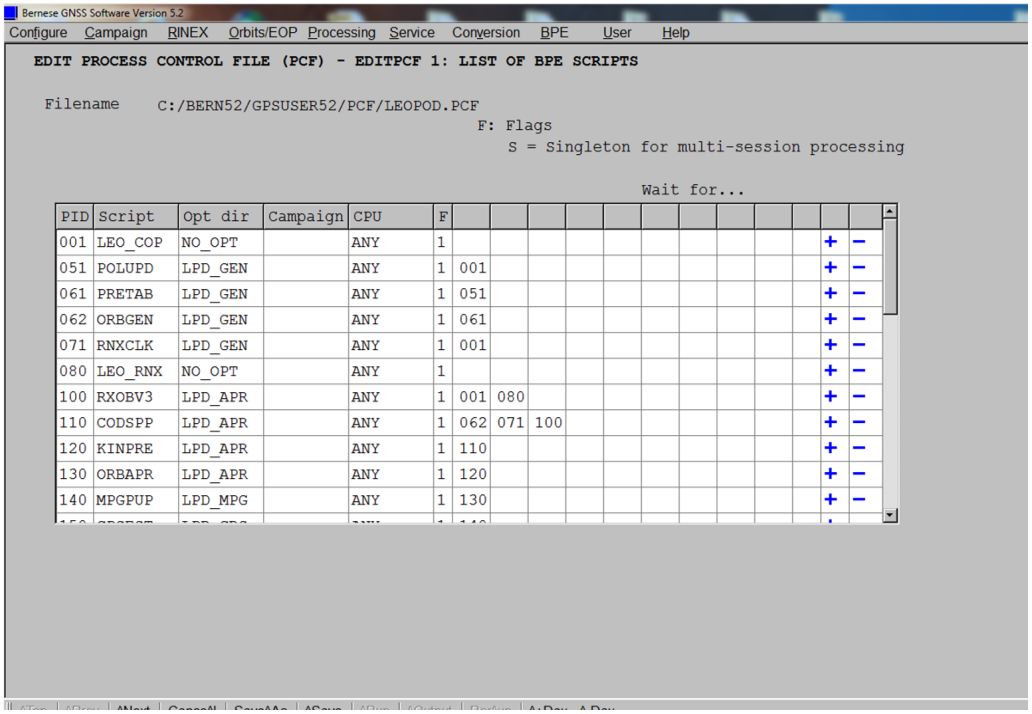

Figure 5.9: *Bernese process control file (PCV)*

The next step, after format converting is to compute a first a-priori orbit based on code measurements and to perform the clock synchronization. This kinematic orbit solution of low precision is used to obtain the initial conditions for a first dynamic orbit integration afterwards.

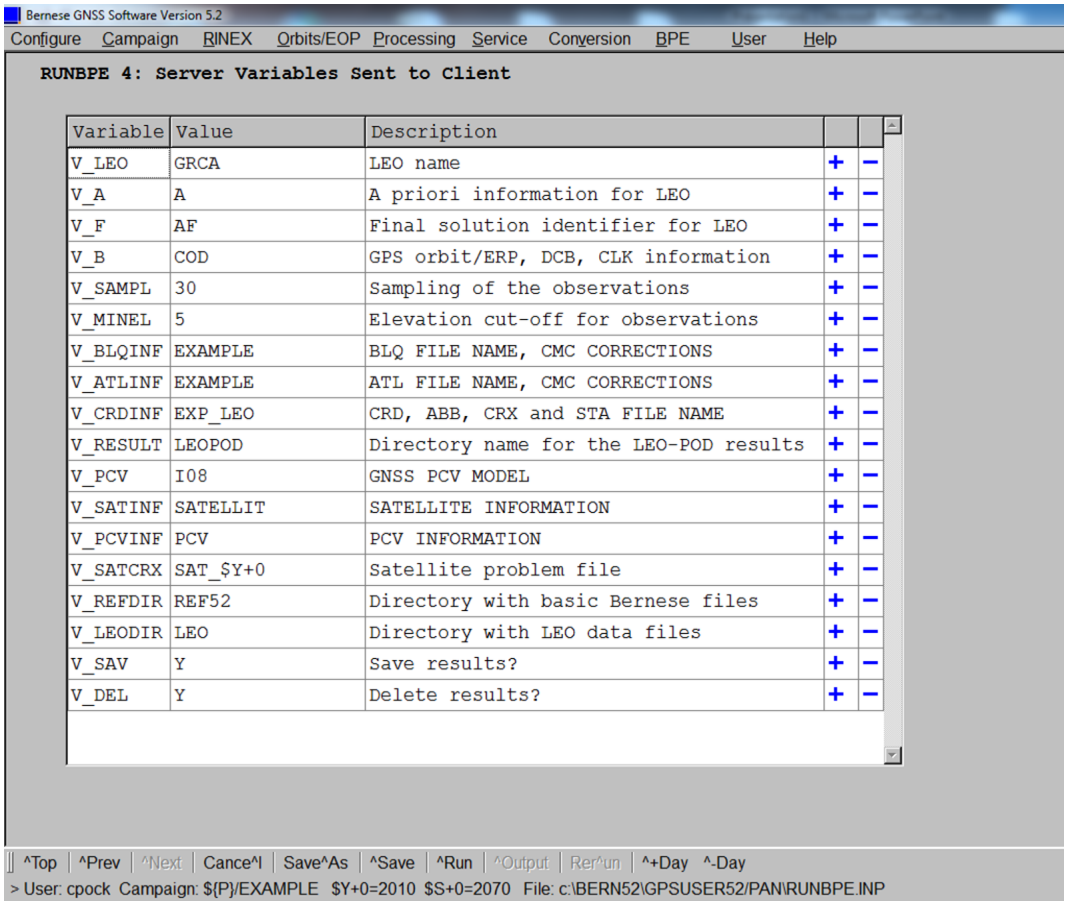

Figure 5.10: *Bernese BPE server variables*

5.8.3 Reference Frame Transformations for POD

The use of different orbit reference frames and the transformation between these systems is an important task in the process of orbit determination. For example, the GNSS-RO needs positions and velocities in an inertial system. Therefore, the Celestial Reference Frame (CRF) was obtained. The CRF is often denoted as Earth Centered Inertial (ECI). The ephemerides data of the GNSS provided by the IGS are related to the Terrestrial Reference Frame (TRF) given in SP3-c format. In addition, receiver and antenna offsets with respect to the center of mass of the satellite are given in the body-fixed satellite coordinate system (SCS). In the following, the basic transformations between the different systems are briefly summarized. The notation used is based on *(Swatschina, 2012)*.

CRF-TRF Transformation

Based on *(Swatschina, 2012)*, a vector $\boldsymbol{r}_{CRF}$, transformed to the TRF is accomplished by

$$\boldsymbol{r}_{TRF} = \boldsymbol{R}(t) \cdot \boldsymbol{r}_{CRF} \ , \tag{5.38}$$

where $\mathbf{R}(t)$ is a time dependent 3×3 orthogonal matrix and consists of different rotations

$$\boldsymbol{R}(t) = \boldsymbol{M}(t) \cdot \boldsymbol{E}(t) \cdot \boldsymbol{N}(t) \cdot \boldsymbol{P}(t) \ , \tag{5.39}$$

where

$\boldsymbol{M}(t)$ is the polar motion - simplified to one matrix,
$\boldsymbol{E}(t)$ is the Earth rotation matrix (Greenwich apparent sidereal time),
$\boldsymbol{N}(t)$ is the nutation matrix,
$\boldsymbol{P}(t)$ is the matrix for the precession.

The exact algorithm is outlined in the International Earth Rotation and Reference Systems (IERS) conventions *(McCarthy and Petit, 2004)*. The latest version was released in 2010[6].

The inverse transformation from the TRF to CRF is given by the transposed matrix of $\mathbf{R}(t)$. The equation reads

$$\boldsymbol{r}_{CRF} = \boldsymbol{R}^T(t) \cdot \boldsymbol{r}_{TRF} \ . \tag{5.40}$$

This transformation is also valid for the case of transforming any perturbing forces and vice versa

$$\ddot{\boldsymbol{r}}_{CRF} = \boldsymbol{R}^T(t) \cdot \ddot{\boldsymbol{r}}_{TRF} \ . \tag{5.41}$$

[6] http://www.iers.org/IERS/

SCS-CRF Transformation

Orbits can be compared in different coordinate systems. A common approach is to transform the celestial positions and velocities in the time varying Satellite Coordinate System (SCS) *(Jäggi, 2007)*. The origin of this system is defined in the spacecrafts center of mass. The three coordinate axis radial $\boldsymbol{r}(t)$, along-track $\boldsymbol{a}(t)$ and across-track $\boldsymbol{c}(t)$ are defined in Fig. 5.11. The differences between kinematic and reduced-dynamic orbits presented in chapter 7 are referred to this coordinate system.

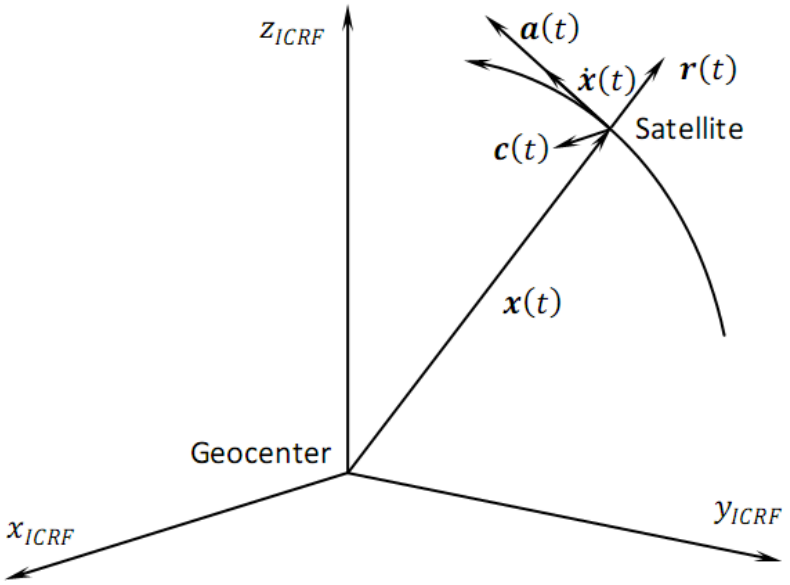

Figure 5.11: *Satellite coordinate system (Swatschina, 2012)*

The particular axis are defined on the position and velocity vector of the satellite

$$\boldsymbol{r}(t) = \frac{\boldsymbol{x}(t)}{|\boldsymbol{x}(t)|} \ , \tag{5.42}$$

$$\boldsymbol{c}(t) = \frac{\boldsymbol{x}(t) \times \dot{\boldsymbol{x}}(t)}{|\boldsymbol{x}(t) \times \dot{\boldsymbol{x}}(t)|} \ , \tag{5.43}$$

$$\boldsymbol{a}(t) = \boldsymbol{c}(t) \times \boldsymbol{r}(t) \ . \tag{5.44}$$

The SCS is an orthogonal, time dependent and right-handed coordinate system with its origin at satellite's center of mass. Using this three axis for the transformation, the rotation matrix reads

$$\boldsymbol{D}(t) = [\boldsymbol{r}(t)\ \boldsymbol{a}(t)\ \boldsymbol{c}(t)]\ , \tag{5.45}$$

and after applying this matrix to the satellite coordinate system the CRF position can be obtained by

$$\boldsymbol{r}_{CRF} = \boldsymbol{D}(t) \cdot \boldsymbol{r}_{SCS}\ , \tag{5.46}$$

and vice versa using the inverse of the rotation matrix $\boldsymbol{D}^T(t)$. This also holds for the TRF

$$\boldsymbol{r}_{TRF} = \boldsymbol{R}(t) \cdot \boldsymbol{D}(t) \cdot \boldsymbol{r}_{SCS}\ , \tag{5.47}$$

$$\boldsymbol{r}_{SCS} = \boldsymbol{D}^T(t) \cdot \boldsymbol{R}^T(t) \cdot \boldsymbol{r}_{TRF}\ . \tag{5.48}$$

Spacecraft Body-CRF Transformation

The spacecraft body system is needed to identify the exact location of instruments (e.g antennas for POD or occultation) and is usually defined with respect to the center of mass of the spacecraft. The alignment to the inertial system is determined by the present attitude. In case of the CHAMP or GRACE mission the nominal attitude model is maintained very accurately *(Swatschina, 2012)*. This nominal attitude model is a close approximation of the body-fixed frame. The three vectors for e.g. the CHAMP mission are defined as shown in Fig. 5.12. Based on *(Swatschina, 2012)* we have

$\boldsymbol{x}_{body}(t)$ perpendicular to the $\boldsymbol{z}_{body}(t)$ axis,
$\boldsymbol{y}_{body}(t)$ perpendicular to the orbital plane,
$\boldsymbol{z}_{body}(t)$ is pointing in the nadir direction,

all three vectors are unit vectors and the orthogonal axes are calculated by

$$\boldsymbol{y}_{body}(t) = -\boldsymbol{c}(t), \tag{5.49}$$

$$\boldsymbol{z}_{body}(t) = -\boldsymbol{r}(t)\ , \tag{5.50}$$

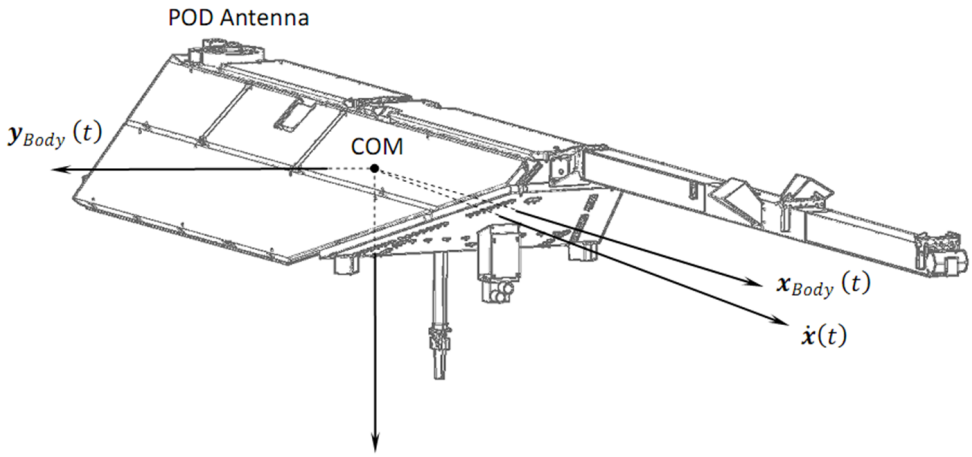

Figure 5.12: *Satellite body coordinate system (Swatschina, 2012)*

$$\boldsymbol{x}_{body}(t) = \boldsymbol{y}_{body}(t) \times \boldsymbol{z}_{body}(t) \ , \tag{5.51}$$

where $\boldsymbol{c}(t)$ and $\boldsymbol{r}(t)$ are defined in Eq. 5.44 and Eq. 5.42. Furthermore, the transformation from the body fixed system to the inertial CRF system is given with the rotation matrix $\boldsymbol{C}$

$$\boldsymbol{C}(t) = [\boldsymbol{x}_{body}(t)\ \boldsymbol{y}_{body}(t)\ \boldsymbol{z}_{body}(t)] \ . \tag{5.52}$$

Applying the matrix to the direction vector, the finally rotated vector reads

$$\boldsymbol{r}_{CRF} = \boldsymbol{C}(t) \cdot \boldsymbol{r}_{body} \ , \tag{5.53}$$

$$\boldsymbol{r}_{body} = \boldsymbol{C}^T(t) \cdot \boldsymbol{r}_{CRF} \ . \tag{5.54}$$

Using only this nominal attitude model as given in Eq. 5.52 provides an accuracy of approximately 3 degrees with respect to the present orientation *(Swatschina, 2012)*. It has to be pointed out that for the strict transformation highly accurate attitude data from star camera observations are needed which are replacing the nominal rotation matrix.

If no precise star camera data is available, this usually leads to errors in the transformation which propagates to position and velocity, depending on the distance

between the satellites instruments and the center of mass. These errors are decreasing with a closer distance to the center of mass. The exact values of the offsets of all investigated satellite missions can be found in section 5.7.2.

5.9 Bernese POD Processing Chain

This section is going to describe the involved scripts which are subsequently used by the BPE in order to compute highly accurate orbit solutions. The following scenario describes the processing (LEOPOD.PCF) *(Bock, 2012)* which is originally tailored to the GRACE mission.

5.9.1 Data Pre-processing

The first processing step is to copy the data from the Bernese DATAPOOL environment to the particular campaign and Bernese folders using the LEO-COP [7] user script. The script has to be adapted for every single LEO mission. The mandatory external files for the orbit processing and their file extensions are in particular

- GNSS precise ephemerides .PRE
- GNSS clocks .CLK
- Earth rotation parameters .ERP

Furthermore, differential code biases corrections between GNSS satellites and ground receivers are needed. These data is only provided by CODE.

- GPS or GNSS file .DCB

For the processing some general files are mandatory. The initial coordinates are given in the station coordinate file

- Station coordinate file .CRD
- Station abbreviation file .ABB
- Station information file .STA

Finally, ocean and atmospheric tidal loading files for the center of mass correction of the orbit positions from Earth-fixed system to the center of mass system of the orbit integration can be taken into account. These files are optional and the corresponding corrections are in the range of a few millimeters.

[7] C:/BERN52/GPSUSER52/SCRIPT

- Ocean loading .BLQ
- Atmospheric loading .ATL

Another important requirement is that the processed satellite mission and all information about antenna offsets, receiver type etc. are already incorporated in the different Bernese input files. Furthermore, the LEO observations are expected in RINEX format and also the corresponding attitude files must be available. Attitude information is mandatory using the BPE, otherwise the BPE will stop with an error if one of the mandatory files is missing. The next step, is to transform the input data into Bernese format. Therefore, a sequence of programs are responsible which are briefly described in the following section.

5.9.2 Prepare Pole, Orbit and Clock Information

POLUPD - extracts Earth rotation information from an IERS format (extension .IEP) and converts into a Bernese pole file format (extension .ERP).

PRETAB - converts the precise GNSS orbits from the Earth-fixed IGS SP3-c format (extension .PRE) into tabular positions in the inertial frame (extension .TAB) for subsequent numerical integration performed by the program ORBGEN.

ORBGEN - integrates the equation of motion using the positions given as tabular orbit and convert them to Bernese standard orbit (extension .STD) The .STD format is a binary format used by the Bernese software. The orbit is represented by 6 osculating elements and 3-9 dynamical parameters associated with solar radiation pressure. Finally, a summary file (extension .PRC) is generated, providing an overview of the orbit quality. When relying on IGS products the rms should be on the centimeter level and the parametrization in based on the Keplerian elements, solar radiation pressure as well as on one set of stochastic pulses every 12 hours.

RNXCLK - extract the GNSS clock information given in clock RINEX file into a Bernese satellite clock file (extension .CLK).

5.9.3 LEO Data Import

RXOBV3 - creates Bernese zero-difference code and phase observation files (extensions .CZH, .CZO, .PZH, .PZO) from RINEX files. In addition, the station

information file is used to check the RINEX header content. If a new station is encountered, the coordinate file and also the abbreviation file will be updated for stations that are not yet listed.

5.9.4 First LEO a-priori Orbit Generation

CODSPP - performs a zero-difference point positioning based on code observations. The receiver clock is synchronized to GPS time and a kinematic code orbit is generated. The program determines approximated LEO positions by a straightforward point positioning approach and a basic outlier detection is included, too.

KINPRE - convert kinematic positions (extension .KIN) to SP3-c format.

ORBAPR - the script performs the orbit integration based on ORBGEN and generates a first a-priori LEO orbit from code-derived kinematic positions.

The coordinates in the precise orbit file are kinematic positions derived only from code observations of the LEO. It is expected that the rms is on the meters level. This result depends on the code observation quality and whether the orbit can be fitted well without any empirical accelerations.

5.9.5 Data Screening

The data screening procedure is done iteratively. The count of iterations (typical 3) is determined by the user.

MPGPUP - script for the programs MAUPRP, GPSEST and ORBGEN to control the LEO observation screening loop.

MAUPRP - detects and corrects cycle slips and add multiple ambiguities for the phase observation files. It works with station observation files in zero-difference mode and single-difference baseline observations. Outlier detection is included, too.

GPSEST - important program within the Bernese software for the least squares parameter estimation. Residual files for data screening based on the ionosphere free linear combinations are estimated. Many more details can be found in *(Dach et al, 2007)*.

RESRMS - produces a residual statistic based on the screened files.

SATMRK - to mark identified outliers in the observation files.

CODSPP - receiver clock synchronization - see section 5.9.4.

Note that all programs run iteratively during the data screening because the first a-priori orbit is not yet good enough for a reliable screening result by the MAUPRP program. Therefore, orbit improvement steps are carried out with GPSEST.

5.9.6 Second LEO a-priori Orbit Generation

STDPRE - produce a precise ephemerides file by coordinate transformation from Bernese standard orbit.

ORBAPF - this script performs the orbit integration based on ORBGEN and generates a second a-priori orbit for the final reduced-dynamic orbit solution.

The positions which were derived from the iteratively data screening plus the orbit improvement step are converted from the standard orbit file using the STDPRE program. This standard orbit file contains epoch-wise accelerations every 15 minutes. The resulting final reduced-dynamic orbit will be generated with piece-wise constant accelerations every 6 minutes which corresponds to 720 parameters per day. Hence, the occurring mixture of empirical parameters and the different sampling rate requires the generation of a new .STD file without pulses using the program ORBGEN. This resulting LEO orbit depends on the fitting quality without setting up any stochastic pulses *(Bock, 2012)*.

5.9.7 Reduced-Dynamic Orbit

GPSEST - reduced-dynamic orbit generation with 6 minutes piece-wise constant accelerations.

GPSXTR - extraction of a summary file of the parameter estimation with GPSEST for reduced-dynamic orbit determination.

ORBGEN - update final reduced-dynamic orbit with orbital elements.

STDPRE - produce a precise ephemerides file by coordinate transformation from Bernese standard orbit.

GPSEST - estimate final phase observation residuals.

RESRMS - produces a residual statistics of the reduced-dynamic orbit generation to validate the quality of the observations.

5.9.8 Kinematic Orbit

GPSEST - performs kinematic orbit and residual estimation.

GPSXTR - extraction of a summary file of the parameter estimation with GPSEST for kinematic orbit determination.

KINPRE - converts kinematic positions (extension .KIN) to SP3-c format.

RESRMS - produces the final residual statistics.

5.9.9 Comparison of Orbits - Internal Orbit Overlap

ORBCMP - compares the reduced-dynamic and kinematic orbits in radial, along-track and out-of-plane direction. The differences are expressed in terms of rms, mean, minimum and maximum values and are expected to be on the few centimeter level *(Bock, 2012)*.

5.9.10 Estimated Output Products

LEO Clock Estimates

The estimated clock offsets are provided in RINEX file format with 10s sampling. The file includes the receiver clock corrections from the kinematic positioning together with the used GNSS satellite clock corrections.

Variance-Covariance Information

The variance-covariance matrix is only available for the kinematic orbit solution. The matrix can be established for every estimated parameter (coordinate, clock,

ambiguities). The reduced-dynamic approach replaces the epoch-wise coordinates by pseudo-stochastic parameters. These estimated parameters can be found in the orbital element file (.ELE) of the Bernese program and are used for the final update to compute the reduced-dynamic solution. The rms values of the Keplerian elements can be found there, too. The stochastic behavior of the pseudo-stochastic orbit parameters is not described in the .ELE file format.

Phase Residuals

The phase residuals of both orbit solutions, the reduced-dynamic and the kinematic are given in the corresponding .RES files estimated by the GPSEST program.

Orbit Outputs

The kinematic positions are given in the .KIN file and in the SP3-c file as Earth-fixed positions. The .KIN file provides additional information whether the solution is based on three different cases. The corresponding flags are

- K - estimate is reliable,
- S - estimate with few observations,
- X - estimation not possible, interpolated coordinate is given.

The reduced-dynamic result is expressed in two coordinate systems, on the one hand, in the Earth-fixed SP3-c format and on the other hand, in the binary inertial .STD format. The orbital elements and empirical parameters of the solution can be found in the corresponding .ELE file.

Processing Summary

The main protocol contains the summary of the processing steps and can be found in the .PRC file. All parameters and the setup for the entire processing are listed here.

For a more detailed description of the particular programs and the whole processing, the reader is referred to the official Bernese user manual *(Dach et al, 2007)* or *(Bock, 2012)*.

6 Aspects of Orbit Uncertainty Estimation

This chapter presents some ideas to capture the uncertainty of the orbit determination. This is a very challenging task because the real orbit is usually unknown. The only way to find the "truth" is to use independent observation methods like SLR and compare these results with POD. Another aspect is to distinguish between uncertainty from the GNSS and LEO orbits. The GNSS orbit uncertainty provided by IGS is currently 2.5 cm *(Griffiths and Ray, 2009)*. This value is derived from weighted individual solutions of the different ACs. Providing a reliable accuracy value for LEO orbits is much more difficult because LEO orbits are typically stand alone solutions and not weighted. Moreover, it is difficult to get free orbit data from different ACs. Another problem is the lack of standards for LEO orbit determination. Besides the use of different force models etc., the orbits are also affected by inconsistent processing strategies, different computation software and "operator noise".

6.1 Error Boundaries for GNSS-RO

For the estimation of LEO orbits the error budget in this research is determined with 5 cm rms for the positions and 0.05 mm/s rms for the orbit velocity, whereby the velocity is more important than the position for the GNSS-RO processing. This is due to highly accurate requirements on the GNSS-RO arcs in the excess phase computation. For the investigated LEO satellites CHAMP, GRACE-A and MetOp-A, these requirements are very challenging but feasible. For the FORMOSAT-3/COSMIC mission this goal is hard to achieve. The achieved rms values are beyond the error boundaries and no independent orbit data provided by different ACs except UCAR is currently available. However, some ideas of capturing the uncertainty are presented in the following.

6.2 Uncertainty Separation Approach

The first idea, is to separate the uncertainty into two parts and quantify it. The two parts are coming on the one hand, from the GNSS orbits and clocks and on the

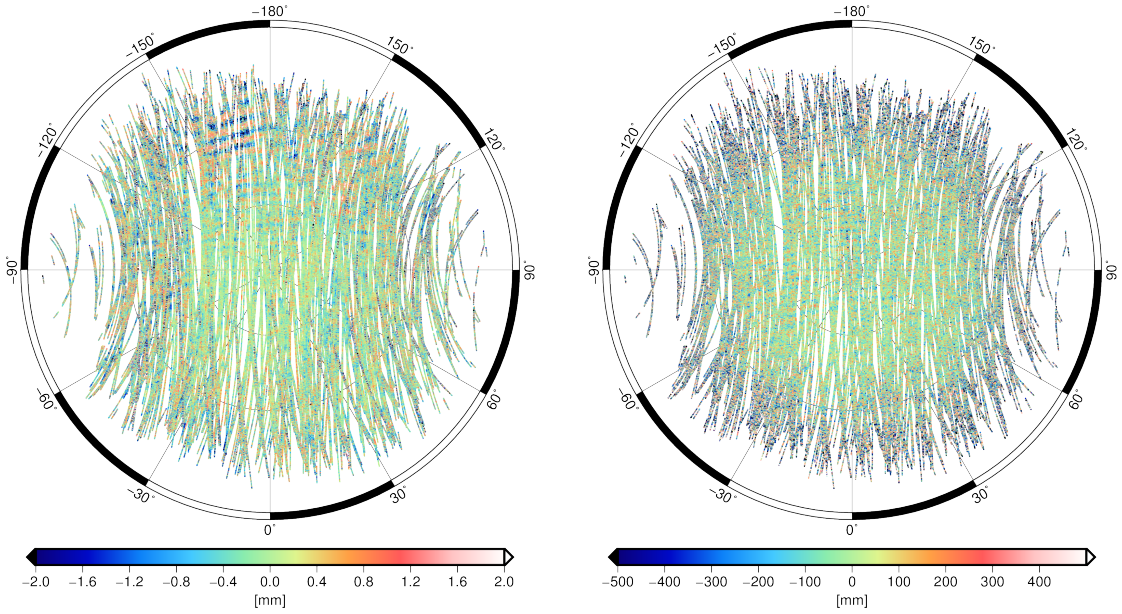

Figure 6.1: *Skyplot of the residuals from phase L1 (left) and code (right) observations for the GRACE-A satellite; day: 14th Jan. 2011*

other hand, from the receiver and tracking noise of the LEO. For the latter, several investigations and intensive in-flight validation of GNSS receivers have been carried out and the reader is referred to excellent literature e.g. *(Montenbruck and Kroes, 2003)*, *(Montenbruck et al, 2006)* or *(Montenbruck et al, 2008)*. However, to give an idea about the magnitude of the receiver and tracking effects, the residuals of one test day for the GRACE-A mission are shown in Fig. 6.1. The phase residuals for both the L_1 and the L_2 phase are on the millimeter level. In this special case, antenna PCVs are applied *(Zehentner and Mayer-Gürr, 2013)*. Compared to the influence on the GNSS and clock side, which is discussed in more detail in section 7.6.5, the receiver plus noise part together is rather low.

6.3 Variance-Covariance Information of Different Orbits

The estimation of orbit positions based on the kinematic approach gives the stochastic information for every epoch (see sec. 5.5). The GNSS-RO technique requires continuous orbit arcs which are not degraded by outliers, jumps or data gaps as is the case for the kinematic approach. Reduced-dynamic orbits are much more appropriate but this type of orbit gives no direct variance-covariance information due to the replacement of the epoch-wise positions by the dynamic force

model and pseudo-stochastic parameters (see sec. 5.6). Hence, only the uncertainty of the stochastic parameters can be described. Another important characteristic of the variance-covariance information is that no biases or systematics in the orbit processing can be detected. It is only the stochastic behavior characterized.

The idea of this investigation is to compute both the kinematic and the reduced-dynamic orbit and compare these two solutions. The statistics of the residuals over one day give an idea about the quality of and consistency of the computed orbits and is a type of internal validation.

For the external validation orbit data from different independent ACs is needed. The computed 24h residuals for the test days and different satellite missions can be found as statistics in chapter 7. Typical rms values are ≤ 4 cm.

6.4 Variance Propagation of Orbit Positions

This idea is based on the assumption that the velocity output of the variational equations can be represented by a higher degree polynomial derivation based on the corresponding orbit positions. In this idealized case, the positions are represented by a polynomial typical of degree n=8 and the velocity is assumed to be a change of the position with respect to time. This simple relation is given in Eq. 6.1

$$\dot{\boldsymbol{x}}(t) = \frac{\partial \boldsymbol{x}(t)}{\partial t}, \tag{6.1}$$

and the polynomial, in this case represents the x component of the coordinate vector reads

$$x(t) = a_0 + a_1 \cdot x + a_2 \cdot x^2 + a_3 \cdot x^3 + ...a_8 \cdot x^8, \tag{6.2}$$

and the velocity expressed as simple derivation becomes

$$\dot{x}(t) = a_1 + 2a_2 \ \cdot x + 3a_3 \cdot x^2 + ...8a_8 \cdot x^7. \tag{6.3}$$

It is important to evaluate the velocity at the mid point of the given interval which is of length n+1. This can be seen in Fig. 6.2.

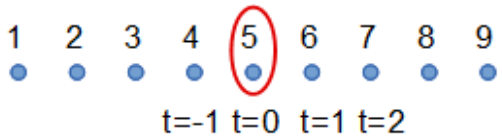

Figure 6.2: *Evaluation of polynomial in the middle of the chosen interval*

First the design matrix $\boldsymbol{A}$ is build. Furthermore, assuming no overdetermination, the polynomial coefficients can be easily calculated from solving the equation system shown in Eq. 6.5.

$$\boldsymbol{A} = \begin{bmatrix} 1 & t & t^2 & \cdots & t^8 \\ \vdots & \vdots & \vdots & \ddots & \vdots \\ 1 & t & t^2 & \cdots & t^8 \end{bmatrix} \tag{6.4}$$

As already mentioned, the velocity will be evaluated at the mid point of the interval, hence, the observations vector $\boldsymbol{y}$ reads

$$\boldsymbol{y} = \begin{bmatrix} x_{-4} \\ \vdots \\ x_0 \\ \vdots \\ x_4 \end{bmatrix} \rightarrow \boldsymbol{b} = \boldsymbol{A}^{-1}\, \boldsymbol{y}, \tag{6.5}$$

and the velocity component turns out directly as the polynomial coefficient a_1 for the time t=0 (see Eq. 6.6). This means that the velocity is indeed nothing else than a linear combination of the coefficient and the position vector $\boldsymbol{y}$.

Hence, the design matrix $\boldsymbol{A}$ respectively the second column of the matrix can be used as a filter. This is due to a given constant time sampling whereby the matrix is not changed.

$$\dot{x}_{mid}(t) = a_1. \tag{6.6}$$

The variance propagation can now be computed assuming white noise σ_x, σ_y, and σ_z typical in the range of some centimeters. This will show the impact of

orbit uncertainty on the corresponding velocity. Taking the y and z coordinates additionally into account, the uncertainty can be estimated as

$$\boldsymbol{\Sigma}(v) = \boldsymbol{A}\ \boldsymbol{\Sigma}(y)\ \boldsymbol{A}^T = \begin{bmatrix} \sigma^2_{v_x} & \sigma^2_{v_{xy}} & \sigma^2_{v_{xz}} \\ \vdots & \sigma^2_{v_y} & \sigma^2_{v_{yz}} \\ \cdots & \cdots & \sigma^2_{v_z} \end{bmatrix} \tag{6.7}$$

In a next step, the entire interval is shifted by one epoch and the variance propagation can be repeated. Note that this approach has not been implemented to the orbit processing within this thesis so far. In this sense only the idea is described in theory here.

7 Orbit Calculation and Results

The calculation of the precise orbits and velocities is carried out for a joint test day and a time span of plus/minus one day. In particular the chosen time period and the missions are

07-08-09 Aug. 2008 - CHAMP
12-13-14 Jan. 2011 - GRACE-A, MetOp-A, FORMOSAT-3/COSMIC
12-13-14 Jul. 2011 - GRACE-A, MetOp-A, FORMOSAT-3/COSMIC
22-23-24 Apr. 2012 - GRACE-A, MetOp-A, FORMOSAT-3/COSMIC
01-02-03 May 2012 - MetOp-A

Within this chapter, all results are displayed for the middle of the 3-days time span. In a first computation step, the precise kinematic and reduced-dynamic orbits and the corresponding velocities are computed for the time span. Afterwards, an independent validation with data provided by external analysis centers has been carried out in order to proof the chosen processing strategy. The achieved results can be found in the following sections, individually treated for each LEO mission.

7.1 LEO POD Processing Overview

For all processed LEO missions the processing steps remain the same

- Based on code observations: receiver clock synchronization and first a-priori initial kinematic orbit computation.
- Iteratively phase reprocessing and data screening: cycle slip detection and fixing, set up ambiguities and improve the a-priori orbit solution.
- New receiver clock synchronization based on screened data - introducing improved a-priori orbit.
- Reduced-dynamic orbit computation based on the ionosphere free linear combination in zero-differencing mode. Orbit parametrization as 6 Keplerian elements, 3 constant acceleration (dynamical parameters) and 720 piece-wise constant accelerations (stochastic parameters) constrained to $5 \cdot 10^{-9} m/s^2$ in along, across and radial direction.

- Kinematic orbit computation based again on the ionosphere free linear combination in zero-differencing mode. Estimation of clock offsets and kinematic positions with more than 5 observations per epoch. Estimation of epoch specific variance-covariance information.
- Comparison of reduced-dynamic and kinematic orbit solutions - estimation of residuals.

All POD orbit solutions are based on the above mentioned processing steps. The screening of the data remains the same for all specified LEO missions. It is important to know that the outcome can be computed straightforward without thinking of individual settings.

7.2 CHAMP POD

For the validation of the computed CHAMP results, data from two different analysis centers is available. The first orbit data set has been computed with the identical Bernese software but with the older version 5.0. This data set is provided by CODE *(Prange, 2010)*. The second data provider UCAR is also equipped with the identical Bernese software. The position and velocity differences are expressed in the Earth-fixed coordinate system. The sampling rate of CODE CHAMP data is 10s. The second validation data set (see Fig. 7.2) provided by UCAR has a sampling rate of 60s.

External and Internal Validation of CHAMP POD

The statistics of the orbit comparison shown in Fig. 7.1 and Fig. 7.2 are summarized in the corresponding Tab. 7.4 and Tab. 7.5. The results compared to CODE show a very good agreement in position and velocity components. This is due to a similar processing strategy and the almost identical external input models but no PCVs are applied. The comparison to UCAR data also shows a good result but here the differences are bigger. There are several reasons for that, e.g. the external input data set used is different and also the degrees of Earth potential and ocean tides is different during the orbit integration process. Nevertheless, the results are on the 5 cm rms level for a 24h RD-orbit processing. The result from the internal orbit comparison of the reduced-dynamic and kinematic solution is shown in Tab. 7.3.

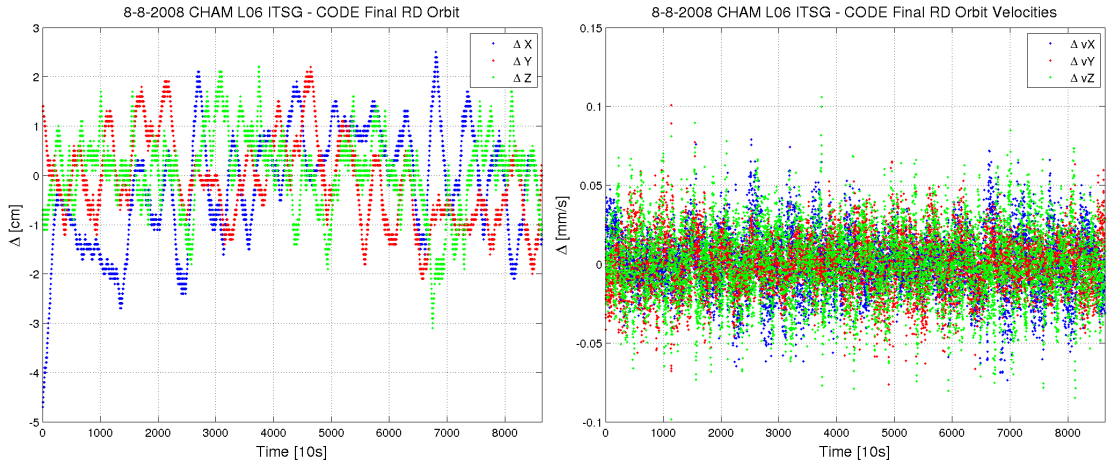

Figure 7.1: *Differences in reduced-dynamic orbit position (left) and velocity (right) compared to* ***CODE*** *for the CHAMP satellite; day: 8th Aug. 2008, sampling rate 10 seconds*

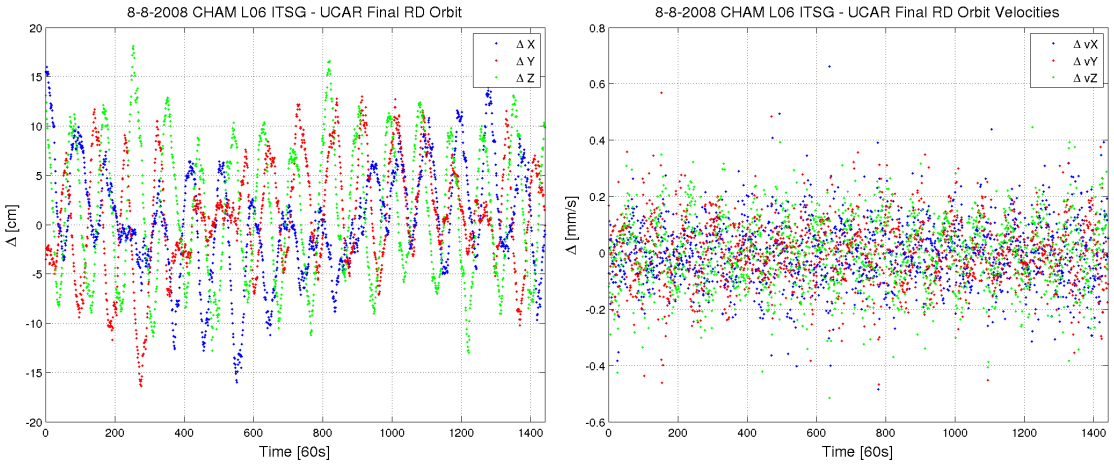

Figure 7.2: *Differences in reduced-dynamic orbit position (left) and velocity (right) compared to* ***UCAR*** *for the CHAMP satellite; day: 8th Aug. 2008, sampling rate 60 seconds*

Table 7.1: *CHAMP 24h RD-orbit compared to* ***CODE****, day: 8th Aug. 2008*

	min [cm]	max [cm]	mean [cm]	rms [cm]
dX	-4.70	2.50	-0.18	1.14
dY	-2.10	2.20	-0.13	0.86
dZ	-3.10	2.20	0.05	0.80
	min [mm/s]	max [mm/s]	mean [mm/s]	rms [mm/s]
dvX	-0.07	0.08	0.00	0.02
dvY	-0.08	0.10	0.00	0.02
dvZ	-0.10	0.11	0.00	0.02

Table 7.2: *CHAMP 24h RD-orbit compared to* ***UCAR****, day: 8th Aug. 2008*

	min [cm]	max [cm]	mean [cm]	rms [cm]
dX	-16.00	16.00	0.37	5.60
dY	-16.40	13.00	0.96	5.58
dZ	-13.00	18.10	1.43	6.89
	min [mm/s]	max [mm/s]	mean [mm/s]	rms [mm/s]
dvX	-0.49	0.66	0.00	0.11
dvY	-0.47	0.57	0.00	0.12
dvZ	-0.52	0.45	0.00	0.13

Table 7.3: *CHAMP 24h kinematic and RD-orbit comparison, day: 8th Aug. 2008*

	min [cm]	max [cm]	mean [cm]	rms [cm]
radial	-13.84	9.20	0.12	2.23
along	-4.98	6.14	0.16	1.76
across	-5.16	3.23	-0.13	1.16

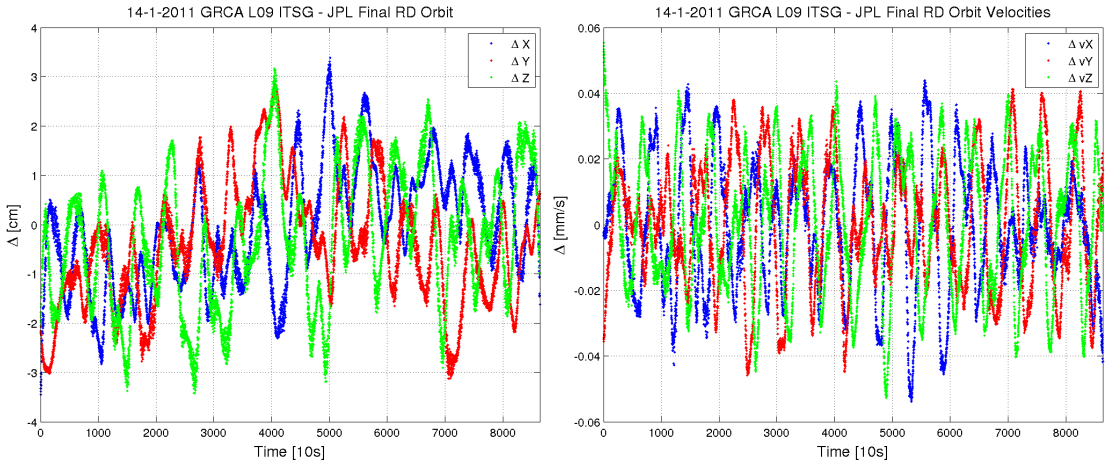

Figure 7.3: *Differences in reduced-dynamic orbit position (left) and velocity (right) compared to **JPL** for the GRACE-A satellite; day: 14th Jan. 2011, sampling rate 10 seconds*

7.3 GRACE-A POD

The GRACE-A solutions are compared with data from different analysis centers. The 10s sampling data is provided by the JPL computed with the GIPSY[1] software whereas the 60s solution is provided by UCAR and computed with Bernese software. The achieved residuals and the very good agreement with JPL in position and velocity components for the three joint test days can be seen within this section.

External and Internal Validation of GRACE-A POD

In general, GRACE-A results show a very good agreement with both data sets provided by the analysis centers CODE and JPL. The results are well below the thresholds for the GNSS-RO processing. Nevertheless, the comparison with JPL data show a better result although they use a completely different software package. For the internal validation the results are on the expected centimeter level.

[1] https://gipsy-oasis.jpl.nasa.gov/

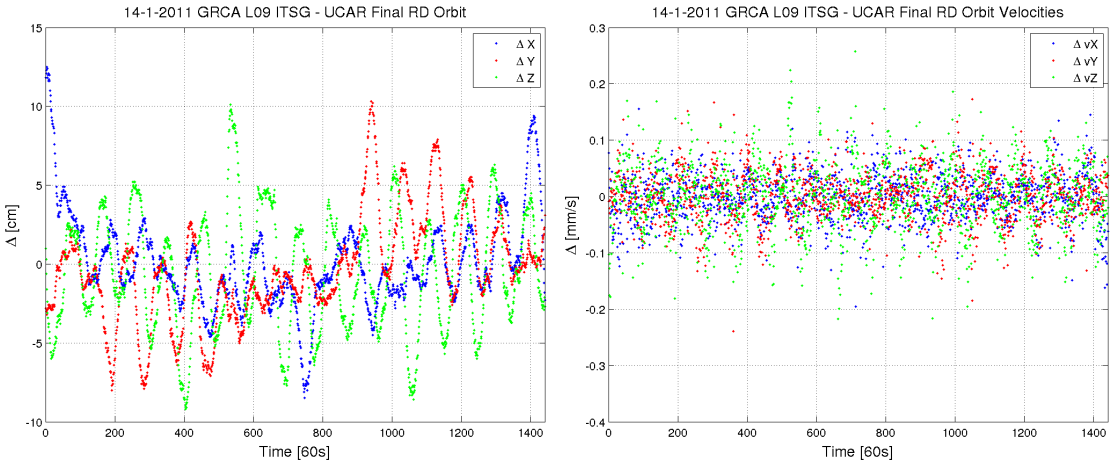

Figure 7.4: *Differences in reduced-dynamic orbit position (left) and velocity (right) compared to* ***UCAR*** *for the GRACE-A satellite; day: 14th Jan. 2011, sampling rate 60 seconds*

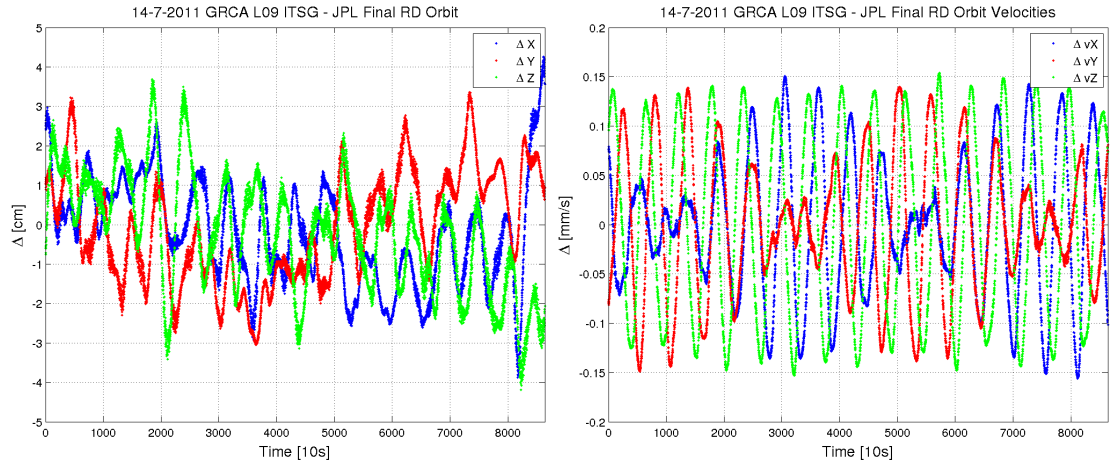

Figure 7.5: *Differences in reduced-dynamic orbit position (left) and velocity (right) compared to* ***JPL*** *for the GRACE-A satellite; day: 14th Jul. 2011, sampling rate 10 seconds*

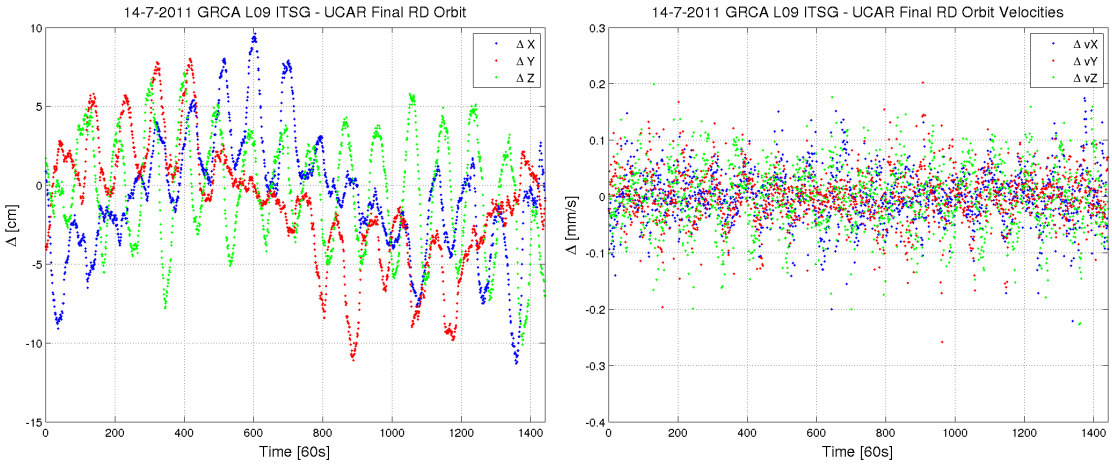

Figure 7.6: *Differences in reduced-dynamic orbit position (left) and velocity (right) compared to* ***UCAR*** *for the GRACE-A satellite; day: 14th Jul. 2011, sampling rate 60 seconds*

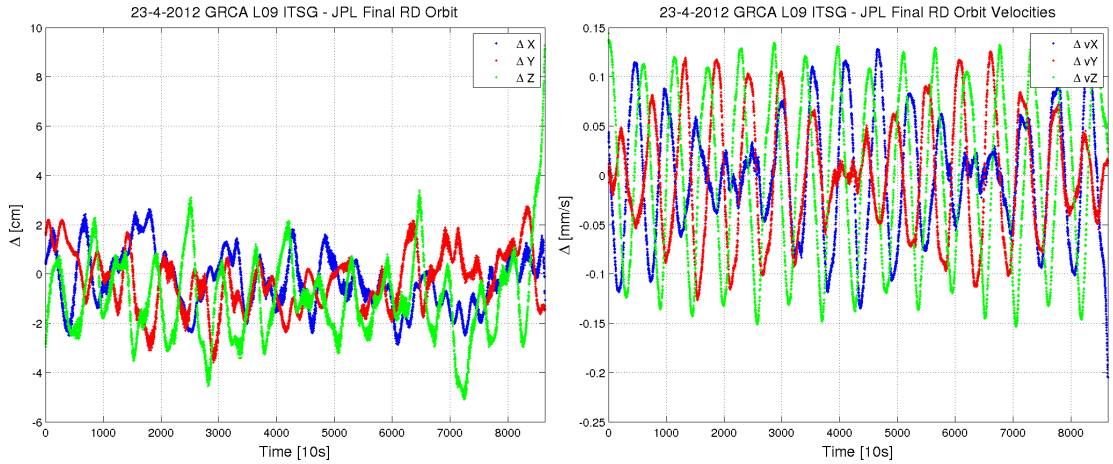

Figure 7.7: *Differences in reduced-dynamic orbit position (left) and velocity (right) compared to* ***JPL*** *for the GRACE-A satellite; day: 23rd Apr. 2012, sampling rate 10 seconds*

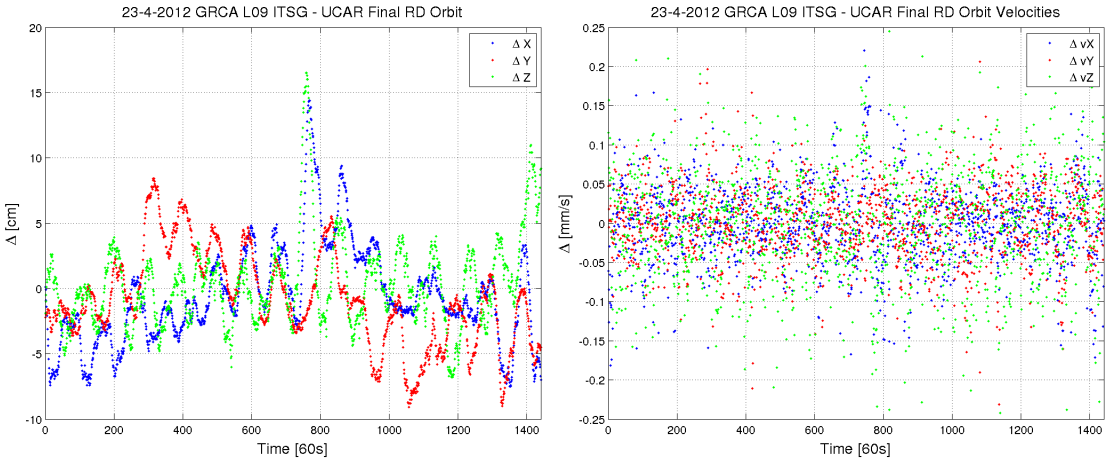

Figure 7.8: *Differences in reduced-dynamic orbit position (left) and velocity (right) compared to* ***UCAR*** *for the GRACE-A satellite; day: 23rd Apr. 2012, sampling rate 60 seconds*

Table 7.4: *GRACE-A 24h RD-orbit compared to* ***JPL****, day: 14th Jan. 2011*

	min [cm]	max [cm]	mean [cm]	rms [cm]
dX	-3.45	3.38	-0.04	1.18
dY	-3.12	2.84	-0.38	1.24
dZ	-3.42	3.17	-0.29	1.35
	min [mm/s]	max [mm/s]	mean [mm/s]	rms [mm/s]
dvX	-0.05	0.04	0.00	0.02
dvY	-0.05	0.04	0.00	0.02
dvZ	-0.05	0.06	0.00	0.02

Table 7.5: *GRACE-A 24h RD-orbit compared to* ***UCAR****, day: 14th Jan. 2011*

	min [cm]	max [cm]	mean [cm]	rms [cm]
dX	-8.50	12.50	0.09	2.95
dY	-8.00	10.30	-0.38	3.28
dZ	-9.20	10.10	-0.51	3.77
	min [mm/s]	max [mm/s]	mean [mm/s]	rms [mm/s]
dvX	-0.20	0.20	0.00	0.04
dvY	-0.24	0.17	0.00	0.04
dvZ	-0.22	0.26	0.00	0.06

Table 7.6: *GRACE-A 24h kinematic and RD-orbit comparison, day: 14th Jan. 2011*

	min [cm]	max [cm]	mean [cm]	rms [cm]
radial	-9.12	11.13	0.00	2.04
along	-5.31	4.31	0.10	1.36
across	-4.30	2.78	0.50	1.16

Table 7.7: *GRACE-A 24h RD-orbit compared to **JPL**, day: 14th Jul. 2011*

	min [cm]	max [cm]	mean [cm]	rms [cm]
dX	-3.88	4.26	-0.19	1.33
dY	-3.05	3.36	-0.07	1.37
dZ	-4.19	3.69	-0.22	1.45
	min [mm/s]	max [mm/s]	mean [mm/s]	rms [mm/s]
dvX	-0.16	0.15	0.00	0.07
dvY	-0.15	0.14	0.00	0.07
dvZ	-0.15	0.15	0.00	0.10

Table 7.8: *GRACE-A 24h RD-orbit compared to **UCAR**, day: 14th Jul. 2011*

	min [cm]	max [cm]	mean [cm]	rms [cm]
dX	-11.30	9.60	-0.71	3.84
dY	-11.10	8.00	-1.16	3.86
dZ	-10.10	7.10	-0.33	3.55
	min [mm/s]	max [mm/s]	mean [mm/s]	rms [mm/s]
dvX	-0.22	0.17	0.00	0.05
dvY	-0.26	0.20	0.00	0.05
dvZ	-0.23	0.20	0.00	0.06

Table 7.9: *GRACE-A 24h kinematic and RD-orbit comparison, day: 14th Jul. 2011*

	min [cm]	max [cm]	mean [cm]	rms [cm]
radial	-15.18	15.67	0.00	2.58
along	-10.45	6.86	-0.21	1.85
across	-3.65	5.61	0.55	1.61

Table 7.10: *GRACE-A 24h RD-orbit compared to **JPL**, day: 23rd Apr. 2012*

	min [cm]	max [cm]	mean [cm]	rms [cm]
dX	-2.87	2.63	-0.25	1.12
dY	-3.60	2.73	-0.27	1.18
dZ	-5.10	9.26	-0.95	1.72
	min [mm/s]	max [mm/s]	mean [mm/s]	rms [mm/s]
dvX	-0.21	0.13	0.00	0.06
dvY	-0.13	0.13	0.00	0.06
dvZ	-0.15	0.14	0.00	0.09

Table 7.11: *GRACE-A 24h RD-orbit compared to **UCAR**, day: 23rd Apr. 2012*

	min [cm]	max [cm]	mean [cm]	rms [cm]
dX	-7.50	14.40	-0.55	3.79
dY	-9.10	8.40	-0.82	3.62
dZ	-6.80	16.50	0.39	3.46
	min [mm/s]	max [mm/s]	mean [mm/s]	rms [mm/s]
dvX	-0.18	0.22	0.00	0.05
dvY	-0.23	0.21	0.00	0.05
dvZ	-0.24	0.24	0.00	0.07

Table 7.12: *GRACE-A 24h kinematic and RD-orbit comparison, day: 23rd Apr. 2012*

	min [cm]	max [cm]	mean [cm]	rms [cm]
radial	-16.69	15.09	0.18	3.03
along	-8.98	28.80	0.00	2.66
across	-4.77	10.73	1.47	2.53

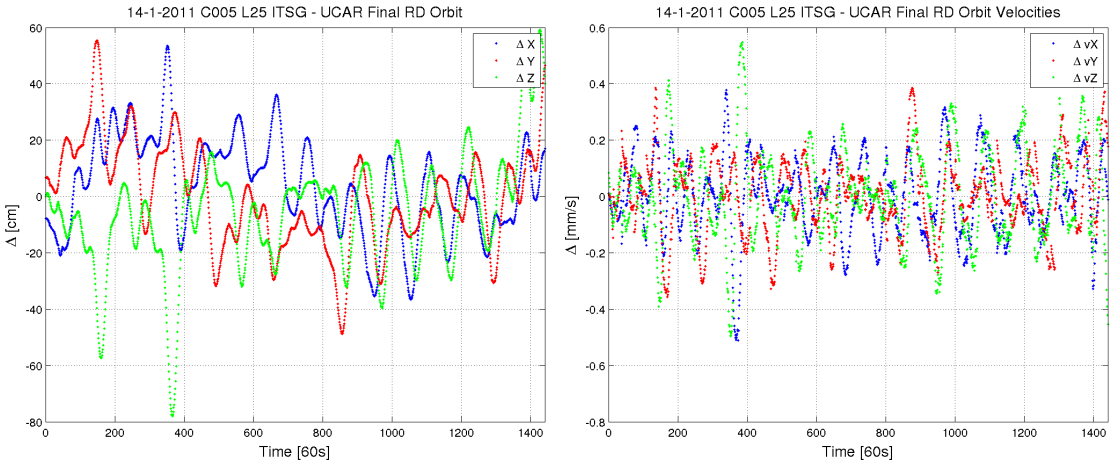

Figure 7.9: *Differences in reduced-dynamic orbit position (left) and velocity (right) compared to* ***UCAR*** *for the COSMIC FM-5 satellite; day: 14th Jan. 2011, sampling rate 60 seconds*

7.4 FORMOSAT-3/COSMIC POD

As mentioned in section 2.3, this mission nominally consists of 6 micro-satellites and every satellite is equipped with two POD patch antennas. For the three test days, only the results from FM-5 are shown. The results from the other days and satellites show similar characteristics. For external validation purposes only data provided by UCAR is available. It has to be pointed out that these reference orbits are computed with nominal attitude, whereas the computed LEO orbits are estimated with the real measured satellite attitude. This may leads to some typical jumps in the comparison results.

External and Internal Validation of FORMOSAT-3/COSMIC POD

The position and velocity rms over one day is on the expected decimeter level. Inter-agency comparisons of post-processed orbits between UCAR, JPL and GFZ show similar results and can be found in *(Schreiner et al, 2010b)*. Due to the fact that the COSMIC kinematic orbit solution consists of a huge amount of interpolated positions caused by observation data gaps, no conclusive interpretation of the internal orbit comparison between the kinematic and reduced-dynamic orbit is possible.

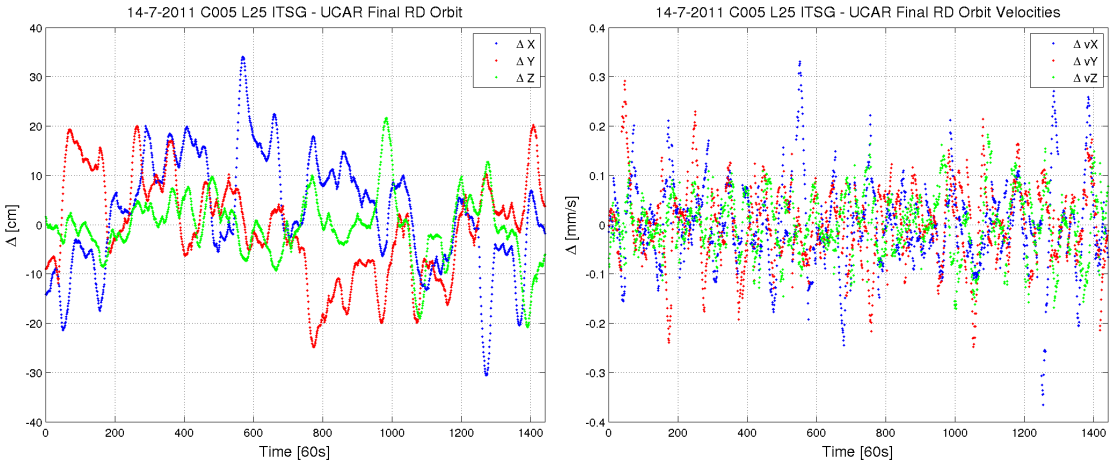

Figure 7.10: *Differences in reduced-dynamic orbit position (left) and velocity (right) compared to* ***UCAR*** *for the COSMIC FM-5 satellite; day: 14th Jan. 2011, sampling rate 60 seconds*

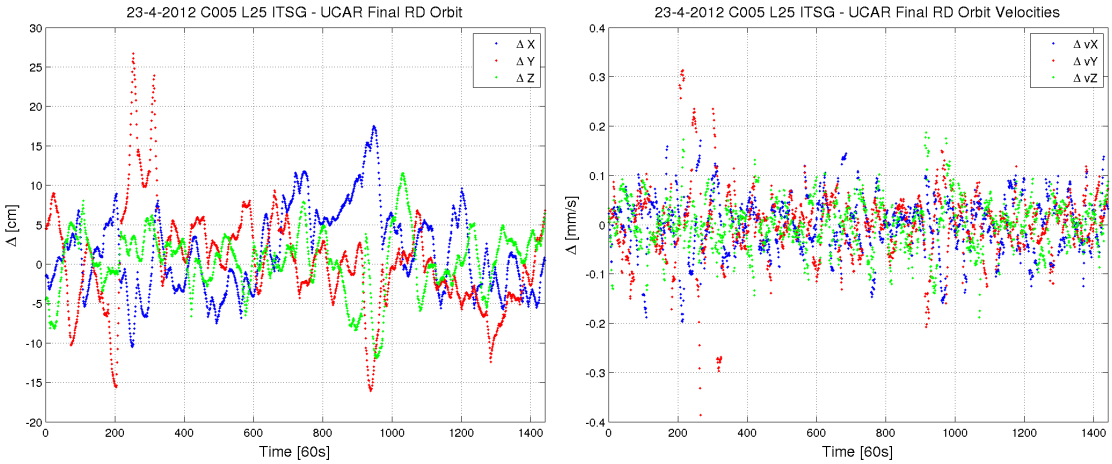

Figure 7.11: *Differences in reduced-dynamic orbit position (left) and velocity (right) compared to* ***UCAR*** *for the COSMIC FM-5 satellite; day: 23rd Apr. 2012, sampling rate 60 seconds*

Table 7.13: *COSMIC FM-5 RD-orbit compared to* ***UCAR****, day: 14th Jan. 2011*

	min [cm]	max [cm]	mean [cm]	rms [cm]
dX	-36.70	53.50	4.00	16.94
dY	-48.90	55.40	0.11	18.07
dZ	-78.00	59.20	-5.67	20.38
	min [mm/s]	max [mm/s]	mean [mm/s]	rms [mm/s]
dvX	-0.51	0.38	0.00	0.14
dvY	-0.36	0.38	0.00	0.13
dvZ	-0.50	0.55	0.00	0.17

Table 7.14: *COSMIC FM-5 RD-orbit compared to* ***UCAR****, day: 14th Jul. 2011*

	min [cm]	max [cm]	mean [cm]	rms [cm]
dX	-30.60	34.10	2.57	11.36
dY	-24.80	20.20	-0.60	10.08
dZ	-20.80	21.60	-0.38	6.42
	min [mm/s]	max [mm/s]	mean [mm/s]	rms [mm/s]
dvX	-0.37	0.33	0.00	0.09
dvY	-0.25	0.29	0.00	0.08
dvZ	-0.17	0.18	0.00	0.06

Table 7.15: *COSMIC FM-5 RD-orbit compared to* ***UCAR****, day: 23rd Apr. 2012*

	min [cm]	max [cm]	mean [cm]	rms [cm]
dX	-10.50	17.50	1.63	5.33
dY	-16.10	26.70	0.28	6.31
dZ	-11.90	11.50	0.43	3.90
	min [mm/s]	max [mm/s]	mean [mm/s]	rms [mm/s]
dvX	-0.20	0.17	0.00	0.06
dvY	-0.39	0.31	0.00	0.07
dvZ	-0.19	0.19	0.00	0.05

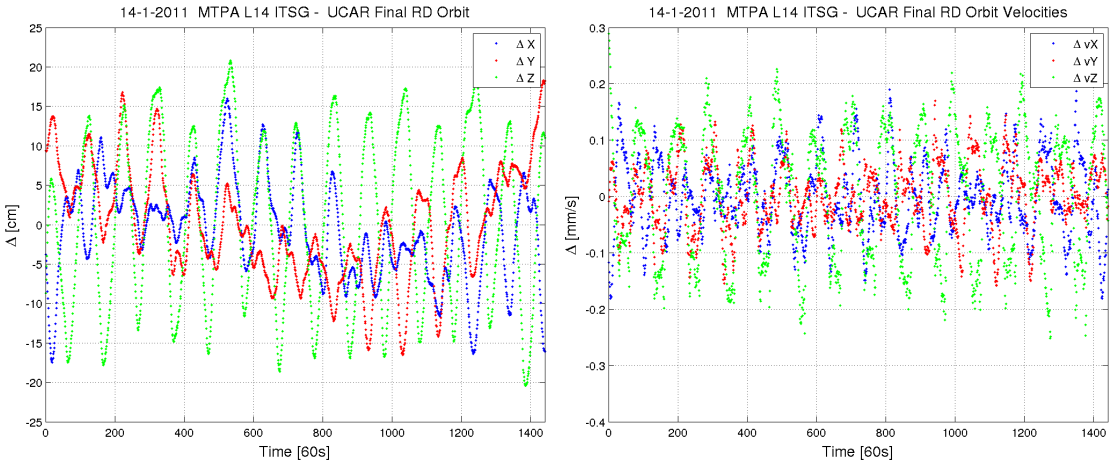

Figure 7.12: *Differences in reduced-dynamic orbit position (left) and velocity (right) compared to* ***UCAR*** *for the MetOp-A satellite; day: 14th Jan. 2011, sampling rate 60 seconds*

7.5 MetOp-A POD

The computed MetOp-A orbits are compared with external data provided by UCAR, too. In contrast to the other investigated satellite missions, the achieved orbit residuals are not as good as expected. UCAR is currently performing a complete reprocessing of their publicly available orbit products. Some investigations by *(Schreiner et al, 2013)* are showing a hemisphere dependent bias in the computed bending angles of COSMIC and MetOp-A. Note that the available attitude data for MetOp-A is of nominal type due to the restricted access to the real measurements.

External and Internal Validation of MetOp-A POD

The results for the MetOp-A satellite compared to the UCAR are very different and difficult to understand. For this mission, observations with 1s sampling rates are available but the achieved results for the orbit comparisons are not as good as expected. The position rms for one day can reach the 10 cm level. Orbit comparisons found in literature *(Montenbruck et al, 2008)* show more consistent results. Currently, UCAR is performing a complete reprocessing of their MetOp-A LEO data.

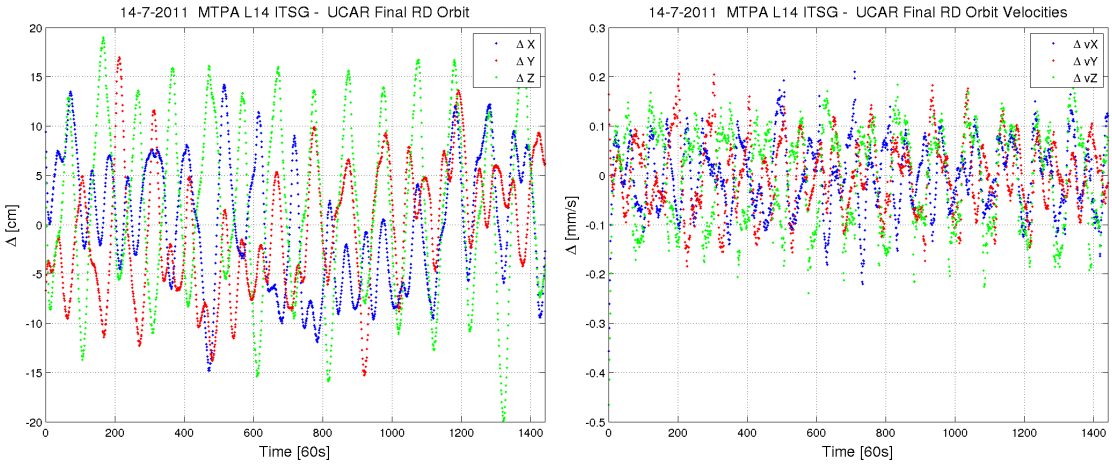

Figure 7.13: *Differences in reduced-dynamic orbit position (left) and velocity (right) compared to* ***UCAR*** *for the MetOp-A satellite; day: 14th Jul. 2011, sampling rate 60 seconds*

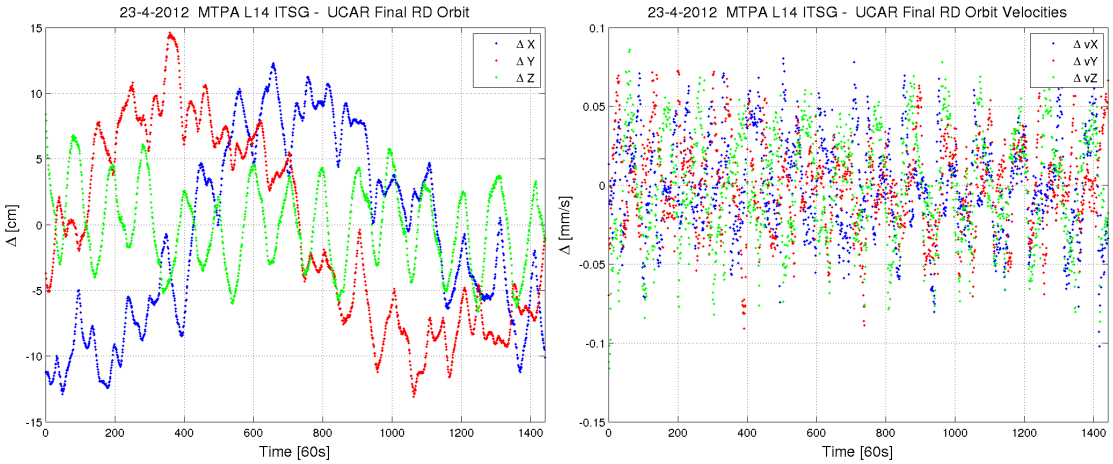

Figure 7.14: *Differences in reduced-dynamic orbit position (left) and velocity (right) compared to* ***UCAR*** *for the MetOp-A satellite; day: 23rd Apr. 2012, sampling rate 60 seconds*

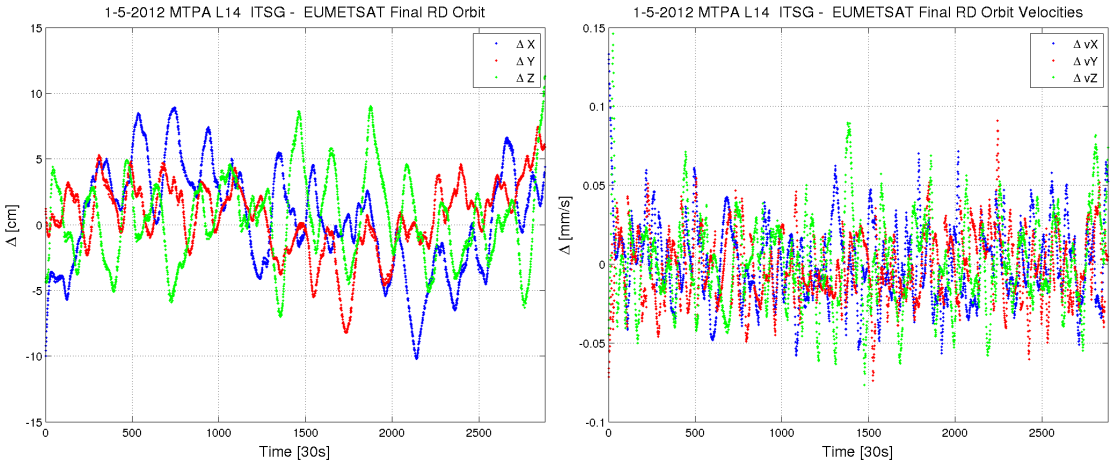

Figure 7.15: *Differences in reduced-dynamic orbit position (left) and velocity (right) compared to* ***EUMETSAT*** *for the MetOp-A satellite; day: 1st May 2012, sampling rate 30 seconds*

In addition, data and a lot of technical description is provided by EUMETSAT. The achieved results compared to this data set show a very good agreement for the complete time span although EUMETSAT is using a different software package (NAPEOS[2]). After comparing UCAR and EUMETSAT orbit settings, it turns out that they are using different antenna offset corrections, too. This is remarkable because these corrections are geometrically defined and assumed to be the same for every analysis center. Nevertheless, the comparison to UCAR are based on UCAR offsets showing significant rms values whereas the EUMETSAT settings provide excellent results (see Fig. 7.15 and Tab. 7.22).

Table 7.16: *MetOp-A 24h RD-orbit compared to* ***UCAR****, day: 14th Jan. 2011*

	min [cm]	max [cm]	mean [cm]	rms [cm]
dX	-17.90	14.20	-1.03	5.36
dY	-14.80	15.80	0.05	6.09
dZ	-18.20	19.60	0.85	9.53
	min [mm/s]	max [mm/s]	mean [mm/s]	rms [mm/s]
dvX	-0.17	0.18	0.00	0.06
dvY	-0.15	0.16	0.00	0.05
dvZ	-0.26	0.32	0.00	0.10

[2]http://www.positim.com/napeos.html

Table 7.17: *MetOp-A 24h kinematic and RD-orbit comparison, day: 14th Jan. 2011*

	min [cm]	max [cm]	mean [cm]	rms [cm]
radial	-41.38	23.12	0.60	4.16
along	-10.65	19.42	0.06	3.46
across	-17.90	14.79	1.47	3.88

Table 7.18: *MetOp-A 24h RD-orbit compared to **UCAR**, day: 14th Jul. 2011*

	min [cm]	max [cm]	mean [cm]	rms [cm]
dX	-14.80	14.20	0.16	6.42
dY	-15.30	17.00	-0.57	6.34
dZ	-19.90	19.00	1.89	8.66
	min [mm/s]	max [mm/s]	mean [mm/s]	rms [mm/s]
dvX	-0.36	0.21	0.00	0.07
dvY	-0.18	0.20	0.00	0.07
dvZ	-0.47	0.22	0.00	0.10

Table 7.19: *MetOp-A 24h kinematic and RD-orbit comparison, day: 14th Jul. 2011*

	min [cm]	max [cm]	mean [cm]	rms [cm]
radial	-30.10	56.03	0.07	6.80
along	-24.30	17.13	-0.06	5.33
across	-98.20	17.58	0.30	7.94

Table 7.20: *MetOp-A 24h RD-orbit compared to **UCAR**, day: 23rd Apr. 2012*

	min [cm]	max [cm]	mean [cm]	rms [cm]
dX	-12.90	12.30	-0.59	7.12
dY	-13.10	14.60	-0.42	7.18
dZ	-6.60	8.40	-0.10	3.15
	min [mm/s]	max [mm/s]	mean [mm/s]	rms [mm/s]
dvX	-0.10	0.08	0.00	0.03
dvY	-0.09	0.09	0.00	0.03
dvZ	-0.09	0.09	0.00	0.03

Table 7.21: *MetOp-A 24h kinematic and RD-orbit comparison, day: 23rd Apr. 2012*

	min [cm]	max [cm]	mean [cm]	rms [cm]
radial	-77.77	29.22	0.35	8.04
along	-26.49	23.72	-0.26	6.85
across	-16.37	16.90	0.03	5.69

Table 7.22: *MetOp-A 24h RD-orbit compared to **EUMETSAT**, day: 1st May 2012*

	min [cm]	max [cm]	mean [cm]	rms [cm]
dX	-10.20	8.90	0.52	3.97
dY	-8.20	7.40	0.60	2.78
dZ	-7.00	11.30	0.40	3.26
	min [mm/s]	max [mm/s]	mean [mm/s]	rms [mm/s]
dvX	-0.06	0.13	0.00	0.02
dvY	-0.07	0.09	0.00	0.02
dvZ	-0.08	0.15	0.00	0.03

7.6 POD Investigations and Results of Orbit Uncertainty Estimation

This section will provide results for different types of investigations. Some of them will have the focus on the computation performance and others will answer open questions concerning the processing strategy. In some cases (e.g. additional stochastic parameters) a reconfiguration of the Bernese software was necessary because the standard definitions are not ready to use for these numbers of parameters. In an other case the session table which is typical defined for a permanent campaign with 24 hours sessions needs to be modified to be able to compute the edge effects for longer arcs.

Also, results connected to chapter 6, where the theoretical background of these investigations was treated are presented within this section. The practical applications of some ideas to quantify orbit uncertainty are shown. The variance-covariance information as one of these ideas is a way of describing the stochastic orbit behavior but is only connected to kinematic orbits and gives no information about biases or offsets. These systematics can only be detected either by independent SLR measurements or by orbit comparisons with data provided by different analysis centers. This circumstance leads to another problems because on the one hand, not all analysis centers share their LEO data and on the other hand, not all LEOs are equipped with laser retro reflectors which are needed for SLR.

The last investigations deal with the GNSS-RO technique and provide the link from the computed orbits to the finally desired excess phase arcs.

7.6.1 Different Observation Sampling Rates

This investigation will show the impact of different observation sample rates. Two reduced-dynamic orbits are computed for the FORMOSAT-3/COSMIC and MetOp-A mission for one test day. On the one hand, with the original observation sampling rate of 1s and on the other hand, with 10s sampling. The differences for the COSMIC FM-5 satellite are shown in Fig. 7.16. It can be clearly seen that there is a strong dependency on the number of input data. This is especially the case for the COSMIC satellites. Here, the number and the quality of the observables is sometimes not sufficient over 24 hours. The MetOp-A satellite is

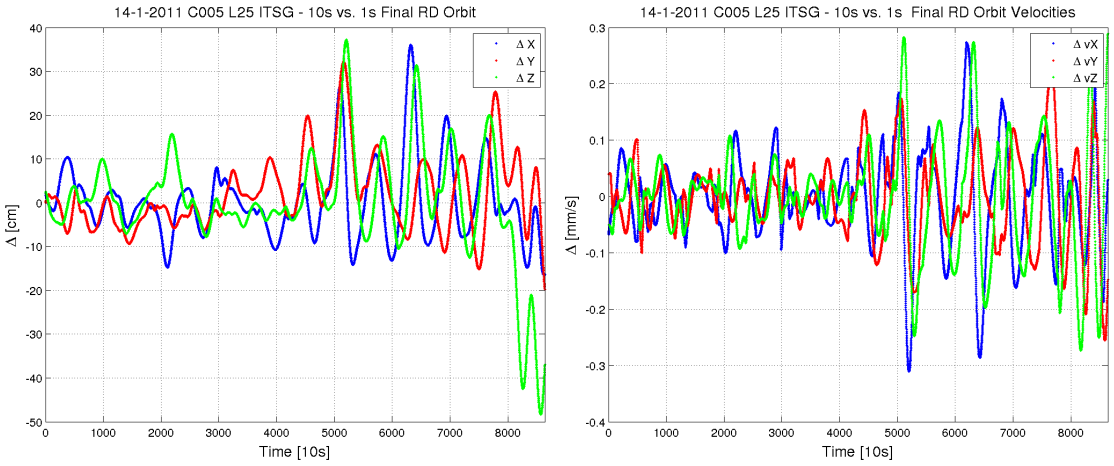

Figure 7.16: *Differences in reduced-dynamic orbit position (left) and velocity (right) based on 10s vs. 1s observations sampling rate for the COSMIC FM-5 satellite; day: 14th Jan. 2011*

showing more robustness. The two solutions are only varying in the range of some few centimeters and also the differences in the satellite velocity is rather low (see Fig. 7.17).

Table 7.23: *COSMIC FM-5 24h RD-orbit differences based on 10s vs. 1s observation sampling rate, day: 14th Jan. 2011*

	min [cm]	max [cm]	mean [cm]	rms [cm]
dX	-16.60	36.00	0.23	8.72
dY	-19.80	32.20	1.89	8.33
dZ	-19.80	32.20	1.89	8.33
	min [mm/s]	max [mm/s]	mean [mm/s]	rms [mm/s]
dvX	-0.31	0.27	0.00	0.09
dvY	-0.26	0.22	0.00	0.08
dvZ	-0.27	0.29	0.00	0.09

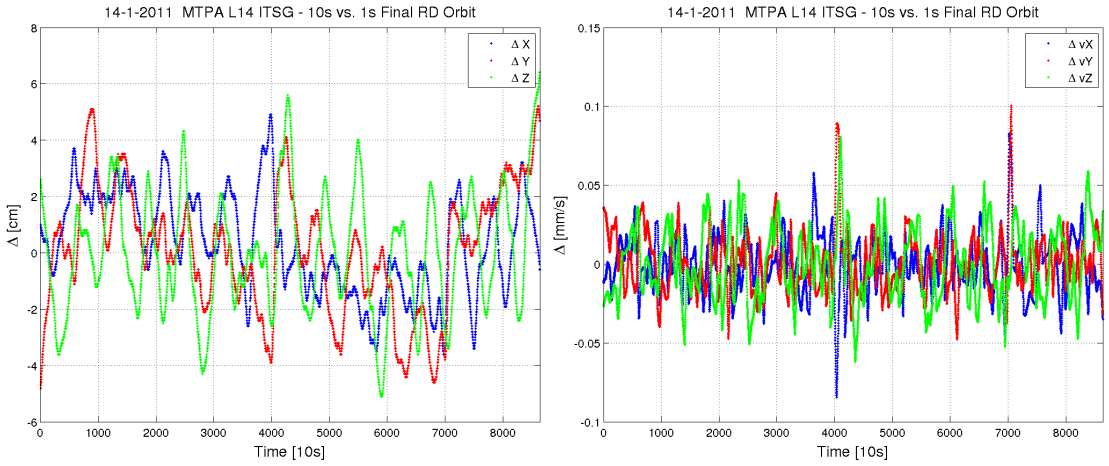

Figure 7.17: *Differences in reduced-dynamic orbit position (left) and velocity (right) based on 10s vs. 1s observations sampling rate for the MetOp-A satellite; day: 14th Jan. 2011*

Table 7.24: *MetOp-A 24h RD-orbit differences based on 10s vs. 1s observation sampling rate, day: 14th Jan. 2011*

	min [cm]	max [cm]	mean [cm]	rms [cm]
dX	-3.60	4.90	0.32	1.78
dY	-4.80	5.20	0.10	2.18
dZ	-5.10	6.40	0.00	2.13
	min [mm/s]	max [mm/s]	mean [mm/s]	rms [mm/s]
dvX	-0.08	0.08	0.00	0.02
dvY	-0.05	0.10	0.00	0.02
dvZ	-0.06	0.08	0.00	0.02

7.6.2 Set-up Different Number of Stochastic Parameters

In this investigation the constant empirical accelerations are set up every 3 and 12 minutes instead of the usual 6 minutes to see the magnitude of change in the orbit estimation while the orbit constraints have remained unchanged. The three solutions are computed for the GRACE-A satellite with 10s observation sampling rate. In Fig. 7.18 the differences between the 6 and 3 minutes solutions can be seen. The impact of these additional 240 parameters is rather low.

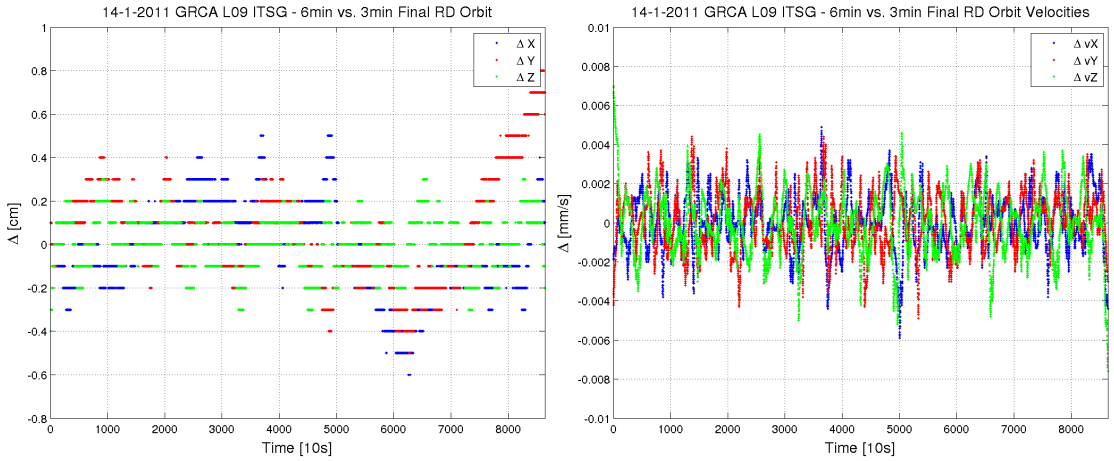

Figure 7.18: *Differences in reduced-dynamic orbit position (left) and velocity (right) based on 6min vs. 3min stochastic parameters for the GRACE-A satellite; day: 14th Jan. 2011, sampling rate 10 seconds*

The resulting orbit differences for the test day are below ± 1cm in the positions and also for the velocities, no significant change is observable. This also holds for the differences of the 6 and 12 minutes solutions as shown in Fig. 7.19.

To summarize, there is no significant contribution to the orbit determination by an additional or a reduced number of stochastic parameters. The behavior of the differences is independent of the investigated satellite mission as long as the quality of the GNSS observations is good. In this special case, a reduced number of stochastic parameters is even sufficient. Due to the fact that this is rarely the case over a long time span, the use of a set of stochastic parameters every 6 minutes is recommended. The difference behavior, especially for the orbit position components looks slightly confusing (see Fig. 7.18). The reason is that the orbit output format (SP3-c) is given only up to the millimeter.

Table 7.25: *GRACE-A 24h RD-orbit differences based on 6min vs. 3min stochastic parameters, day: 14th Jan. 2011*

	min [cm]	max [cm]	mean [cm]	rms [cm]
dX	-0.60	0.50	-0.02	0.20
dY	-0.50	0.80	0.06	0.23
dZ	-0.40	0.30	0.01	0.12

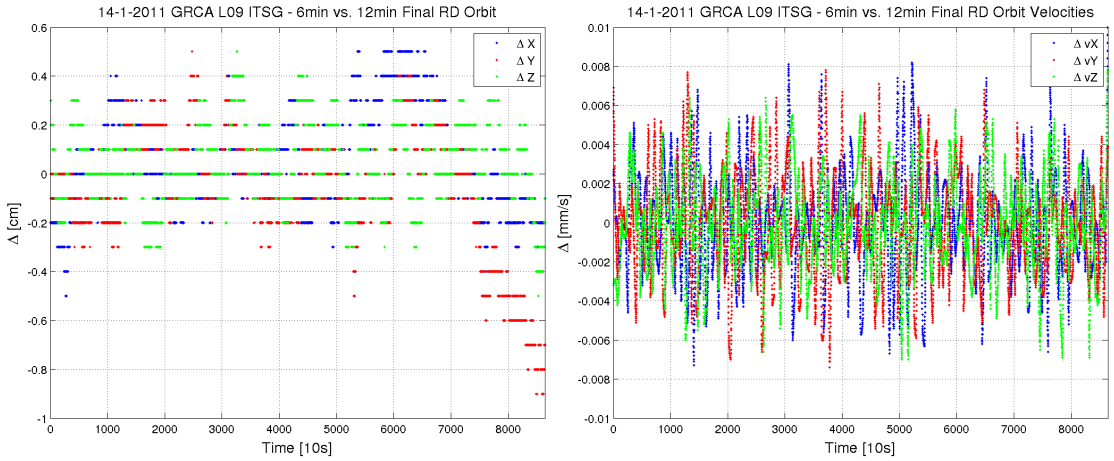

Figure 7.19: *Differences in reduced-dynamic orbit position (left) and velocity (right) based on 6min vs. 12min stochastic parameters for the GRACE-A satellite; day: 14th Jan. 2011, sampling rate 10 seconds*

Table 7.26: *GRACE-A 24h RD-orbit differences based on 6min vs. 12min stochastic parameters, day: 14th Jan. 2011*

	min [cm]	max [cm]	mean [cm]	rms [cm]
dX	-0.50	0.50	0.06	0.20
dY	-0.90	0.50	-0.06	0.25
dZ	-0.50	0.50	0.05	0.16

7.6.3 Edge Effects Caused by Different Processing Lengths

In this section, the impact of different processing lengths are investigated. In the first processing, three days are computed individually with a time span of 24h each. Afterwards, these three solutions are combined to one 30h arc. In a second step a continuous 30h arc is computed directly. Now it is possible to see the edge effects at the beginning and end of the 24h period by comparing the two 30h arc solutions. The sudden jumps in position and velocity components can be clearly identified but are in general not critical for the orbit computation. In Fig. 7.20, the edge effects are exemplarily shown for the GRACE-A satellite.

The Bernese orbit estimation is usually configured to day-by-day 24h arc length processing. For these investigations it is not enough to change only the orbit integration length and the session table definition. The complete input data sets

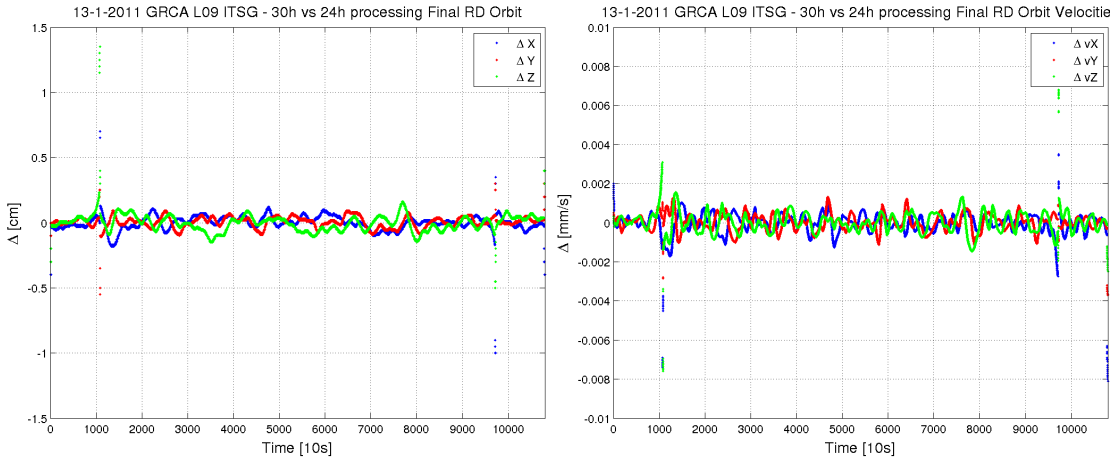

Figure 7.20: *Differences in reduced-dynamic orbit position (left) and velocity (right) based on different processing lengths for the GRACE-A satellite; days: 13th-15th Jan. 2011, sampling rate 10 seconds*

(GNSS and LEO data) which are usually given day-by-day must be manipulated to ensure a correct processing. This pre-processing is very costly from a computational point of view and does not appear reasonable in relation to the efforts.

Table 7.27: *GRACE-A 30h RD-orbit differences based on different processing lengths, days: 13th-15th Jan. 2011*

	min [cm]	max [cm]	mean [cm]	rms [cm]
dX	-1.00	0.70	0.00	0.06
dY	-0.55	0.30	0.01	0.04
dZ	-0.50	1.35	0.00	0.07

7.6.4 Impact of Different GNSS Clock Correction Rates

The clock corrections of the GPS system are representing the offsets of the GPS clocks aboard the satellites with respect to the GPS system time. These offsets are estimated from ground station network and are the result of weighted individual solutions (IGS) with 30s sampling. High rate clock corrections every 5s are provided by CODE besides the standard 30s clock interval. To see the change in the orbits the two solutions from CODE have been compared for the test days. In Fig. 7.21, the result from one single day can be seen which is representative for all

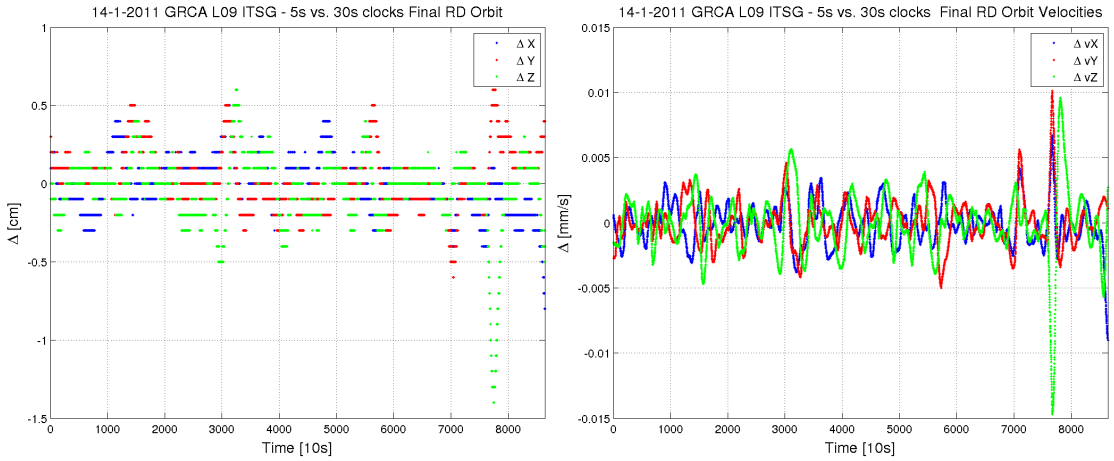

Figure 7.21: *Differences in reduced-dynamic orbit position (left) and velocity (right) based on 5sec vs. 30sec GPS-clock corrections for the GRACE-A satellite; day: 14th Jan. 2011, sampling rate 10 seconds*

other test days. The changes in the position are on the sub-cm level, the velocity differences caused by different GPS clock correction rates are rather low.

7.6.5 Results of Uncertainty Separation Approach

The entire orbit uncertainty is separated into two parts. The first part is depending on the tracking and receiver noise. By introducing phase center variations, the effect for both carrier phase measurements L_1 and L_2 is on the millimeter level as shown in chapter 6. This effect is rather small compared to the effect caused by different GNSS input data. In this investigation, input data provided by CODE and IGS are compared for the test days. The processing strategy remains exactly the same and the differences in Fig. 7.27 are caused by different GNSS orbits, clock corrections and Earth rotation data. The data provided by IGS is based on weighted individual solutions from different analysis centers within the IGS. CODE is one of these analysis centers. The differences are only up to $\pm$ 1.5 cm and $\pm$ 0.01 mm/s. This is due to the fact that CODE is one of the important and biggest contributors to the IGS and this in turn results in a higher weighting of their orbits.

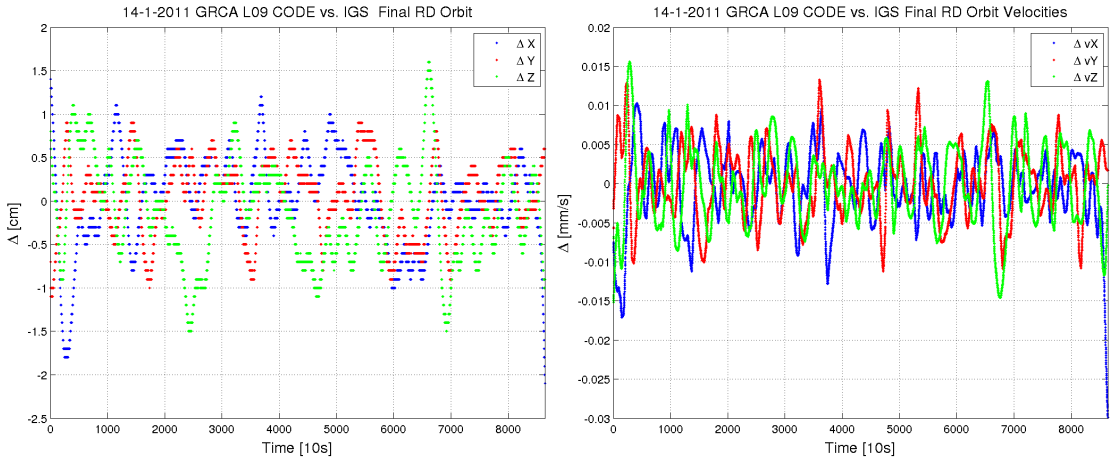

Figure 7.22: *Differences in reduced-dynamic orbit position (left) and velocity (right) based on CODE vs. IGS input data for the GRACE-A satellite; day: 14th Jan. 2011, sampling rate 10 seconds*

7.7 Link to GNSS-RO Orbit Arcs

Several LEO orbits and velocities for different satellite missions have been computed. Now, the bridge to the GNSS-RO and the excess phase processing can build. In this section the differences between the UCAR 50 Hz LEO data given in the inertial true-of-date (TOD) system and the results computed within this thesis are shown.

The UCAR data is provided with atmospheric excess phase level-1b files, given in the Network Common Data Format (NetCDF)[3]. This binary file format is given individually for every occultation event on a daily basis. The positions and velocities of the GNSS and LEO satellites as well as the starting and ending times of every occultation event and the computed excess phase data is provided, too. Besides from these data, there are many more physical quantities stored within this files. For more details the reader is referred to the official website[4].

The future work of excess phase processing is shown in Fig. 7.23. Note that LEO and GNSS satellites are orbiting far away from each other. Therefore, the transmitted GNSS signal needs about 0.07 seconds for the transmission and both satellite positions may change significantly during this period. The LEO data

[3]http://www.unidata.ucar.edu/packages/netcdf/index.html
[4]http://cdaac-www.cosmic.ucar.edu/cdaac/doc/formats.html

is given at signal reception time, the GNSS satellites at signal transmission time. This transmission time needs to be determined. For this purpose a proper strategy is presented in *(Zhang et al, 2013)*.

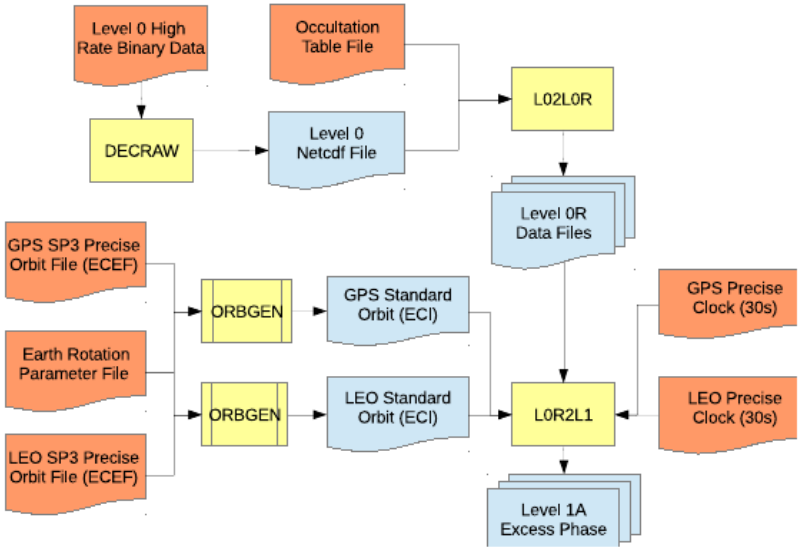

Figure 7.23: *Excess phase level-1b processing (Zhang et al, 2013)*

7.7.1 Data Preparation for GNSS-RO Event Interpolation

To give an idea about the GNSS-RO arc data sets, selected UCAR reference results are exemplarily visualized for 4 individual occultation events, as shown in Fig. 7.24. The occulting GNSS satellites involved are in particular G13, G10, G24 and G31. The duration of the different occultation events is presented in Tab. 7.28.

Table 7.28: *Duration of selected CHAMP GNSS-RO events; day: 8th Aug. 2008*

G13 event **1** [s]	G10 event **2** [s]	G24 event **3** [s]	G31 event **4** [s]
64.46	121.46	57.46	138.46

Concerning the quality of the computed GNSS-RO arcs, the CHAMP satellite is used on behalf of all other investigated LEO missions. This is due to the consistent use of the same sub-daily pole model (IERS2010) and nutation model (IAU2000R06) for the UCAR CHAMP2014 reprocessing. Other provided occultation data e.g. GRACE-A are based on older sub-daily pole and nutation models. Currently, there is work in progress to reprocess the entire occultation data sets with up to date models.

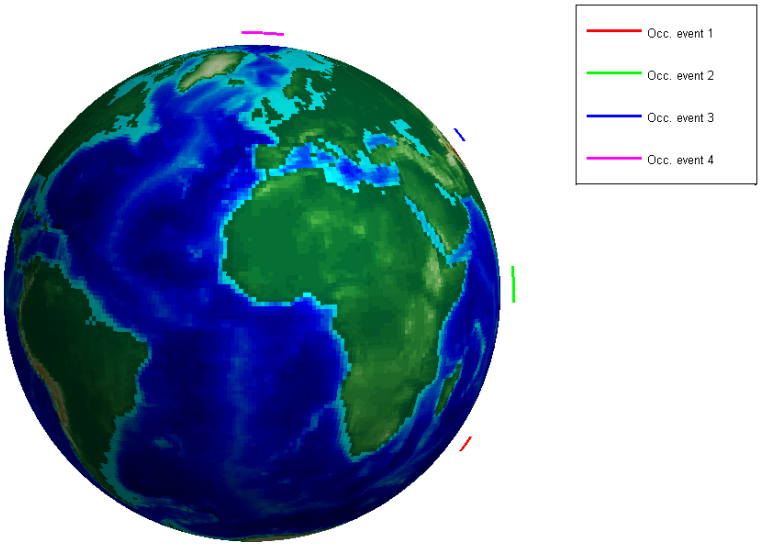

Figure 7.24: *Selected GNSS-RO events for CHAMP; day: 8th Aug. 2008*

For the data preparation task it is important to distinguish between GNSS and LEO data. LEO orbits are based on the POD navigation antenna, collecting observations with 1s or 10s sampling rates, whereas the occultation antenna is recording measurements to the occulting GNSS satellite on the 50 Hz level. Hence, for the GNSS-RO technique, positions and velocities must refer to these high frequent data. Therefore, the originally computed 1s or 10s reduced-dynamic LEO POD data provides a stable basis for coordinate and velocity interpolation at the 50 Hz events. A more detailed explanation of the GNSS-RO observation technique can be found in chapter 4.

The high precise GNSS orbits are originally provided by the IGS or other analysis centers with 15 minutes sampling. The corresponding GNSS satellite velocities are not being provided. Due to the absence of many perturbing forces at MEO orbit attitudes (see chap. 3), the orbits are smooth. This in turn, provides a stable basis for the 50 Hz GNSS-RO event arc interpolation, too. Nevertheless, the Bernese STDPRE program can be used to compute GNSS orbits and velocities with every desired sampling interval. This task can be easily included in the excess phase processing chain.

After transforming the Earth-fixed SP3-c LEO data into the J2000 celestial inertial system (CRF), an additional transformation to the occultation Earth-Centered Inertial (ECI) true-of-date coordinate system is needed. The relationships between the different systems are presented in Fig. 7.25. Finally, the orbits are interpolated

to the 50 Hz occultation events and compared with the originally UCAR reference data. The achieved results are in a similar range as the Earth-fixed LEO orbit differences. Some space for improvements is given due to the fact, that the exact input models and settings for the true-of-date transformation are not yet known.

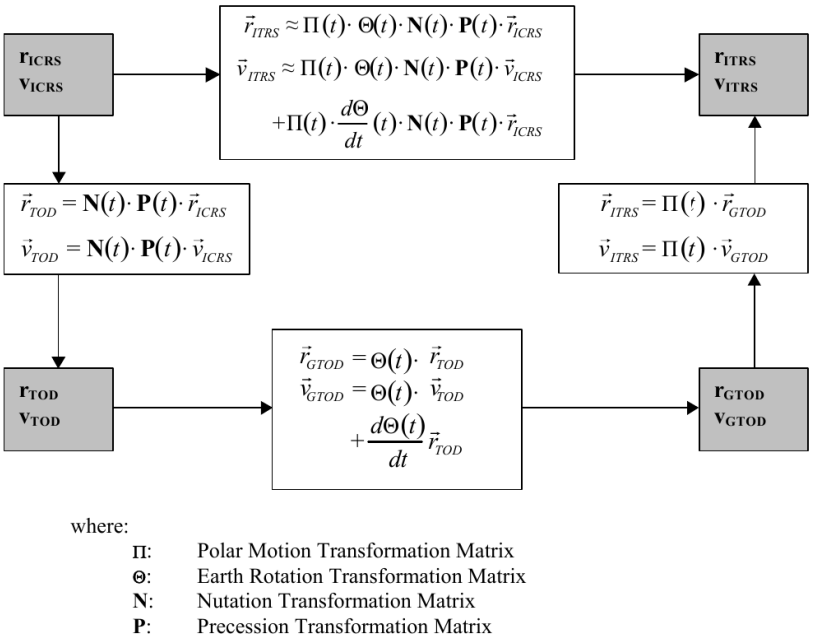

Figure 7.25: *Relationships between coordinate reference systems (CCSDS, 2010)*

7.7.2 Results of GNSS-RO Arc Comparisons

For the interpolation to the specific GNSS-RO time tags a polynomial of degree 7 is used. In addition the offsets of the center of mass to the occultation antenna must be considered. After coordinate transformation from the spacecraft reference frame to the J2000 inertial CRF, using the satellite attitude data the offsets are applied. The original offset values are shown in Tab. 7.29.

Table 7.29: *CHAMP occultation helix offsets*

x[m]	y[m]	z[m]
-1.6431	0.0000	-0.0646

The change of the LEO position and velocity components during the occultation events with a average duration of 1-2 minutes is expected to be rather low and almost constant. The illustrations and statistics of the achieved results is provided in the following.

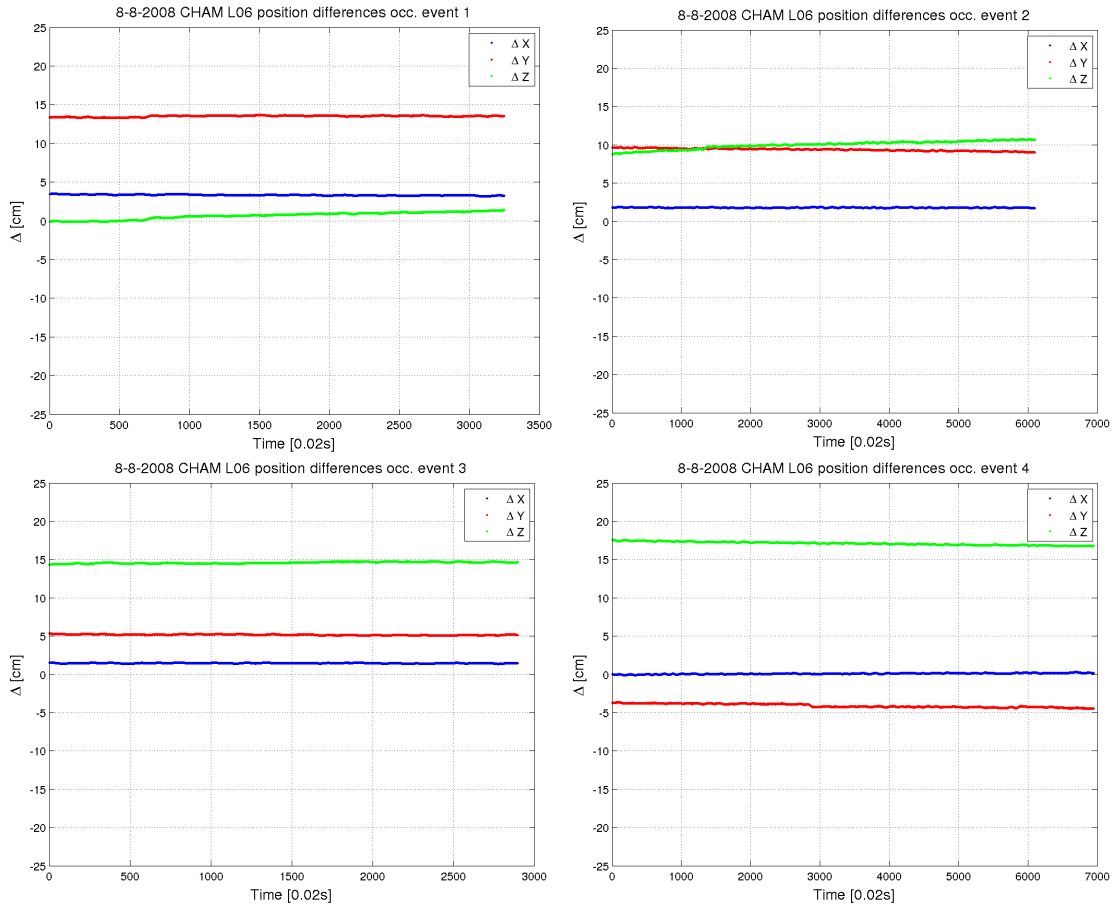

Figure 7.26: *Position differences of the selected occultation arcs, CHAMP satellite; day: 8th Aug. 2008, sampling rate 0.02 seconds*

Table 7.30: *CHAMP GNSS-RO arc comparison of event **1**; day: 8th Aug. 2008*

	min [cm]	max [cm]	mean [cm]	rms [cm]
dX	3.14	3.51	3.32	3.32
dY	13.29	13.65	13.51	13.51
dZ	-0.13	1.38	0.67	0.80
	min [mm/s]	max [mm/s]	mean [mm/s]	rms [mm/s]
dvX	-0.060	-0.053	-0.056	0.056
dvY	0.032	0.045	0.038	0.038
dvZ	0.120	0.132	0.123	0.124

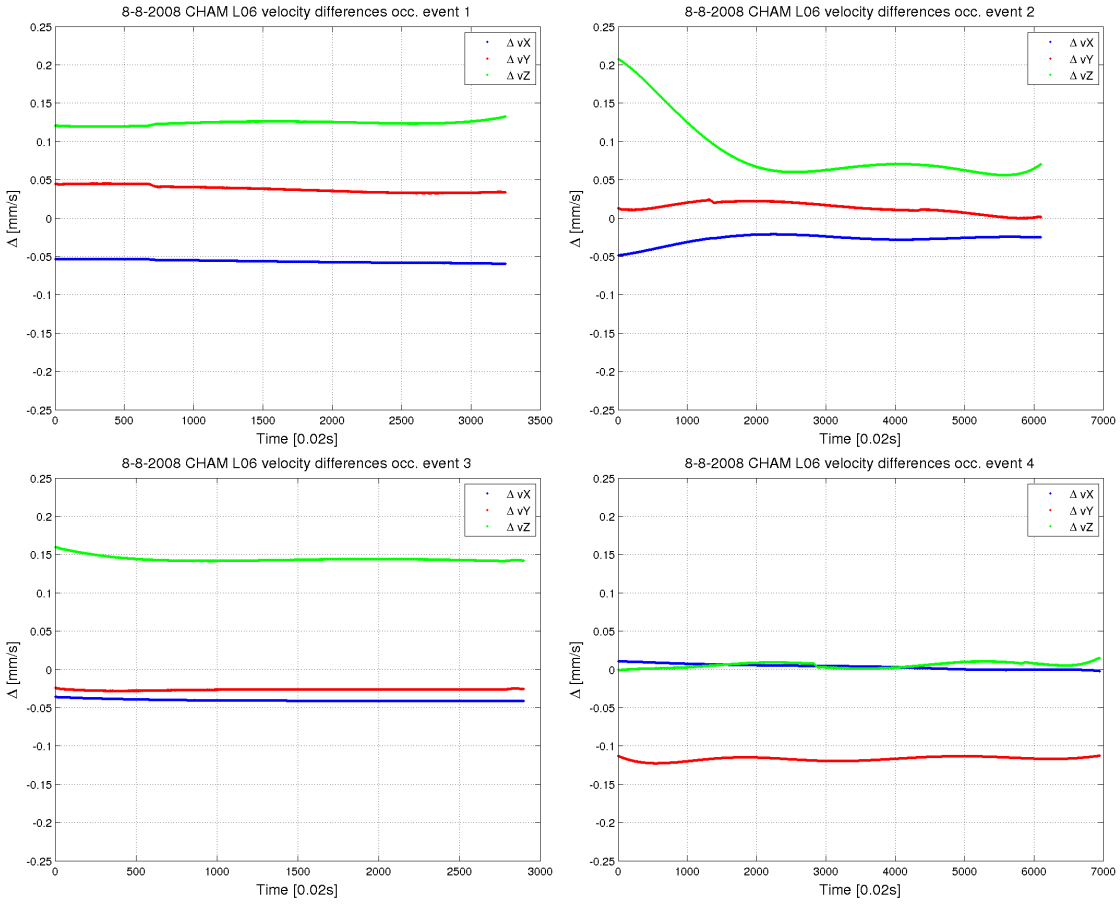

Figure 7.27: *Velocity differences of the selected occultation arcs, CHAMP satellite; day: 8th Aug. 2008, sampling rate 0.02 seconds*

Table 7.31: *CHAMP GNSS-RO arc comparison of event 2; day: 8th Aug. 2008*

	min [cm]	max [cm]	mean [cm]	rms [cm]
dX	1.70	1.88	1.79	1.79
dY	8.99	9.70	9.37	9.37
dZ	8.76	10.73	9.98	10.00
	min [mm/s]	max [mm/s]	mean [mm/s]	rms [mm/s]
dvX	-0.048	-0.021	-0.027	0.028
dvY	0.000	0.023	0.013	0.015
dvZ	0.056	0.207	0.085	0.094

Table 7.32: *CHAMP GNSS-RO arc comparison of event **3**; day: 8th Aug. 2008*

	min [cm]	max [cm]	mean [cm]	rms [cm]
dX	1.36	1.54	1.46	1.46
dY	5.05	5.33	5.17	5.17
dZ	14.29	14.77	14.58	14.59
	min [mm/s]	max [mm/s]	mean [mm/s]	rms [mm/s]
dvX	-0.041	-0.036	-0.040	0.040
dvY	-0.028	-0.024	-0.026	0.026
dvZ	-0.141	0.160	0.144	0.144

Table 7.33: *CHAMP GNSS-RO arc comparison of event **4**; day: 8th Aug. 2008*

	min [cm]	max [cm]	mean [cm]	rms [cm]
dX	-0.09	0.28	0.10	0.12
dY	-4.49	-3.65	-4.08	4.09
dZ	16.75	17.57	17.10	17.11
	min [mm/s]	max [mm/s]	mean [mm/s]	rms [mm/s]
dvX	-0.002	0.010	0.003	0.004
dvY	-0.122	-0.112	-0.116	0.116
dvZ	0.000	0.014	0.005	0.006

8 Conclusion and Outlook

The envisaged goal to provide LEO position and velocity data on the same accuracy level compared to the established analysis centers CODE, UCAR, JPL and EUMETSAT was achieved. As demonstrated in chapters 5 and 7, the chosen orbit processing strategy enables an accurate and continuous outcome independent of the specified LEO mission and a good agreement in the results. The orbit position comparisons are in general on the sub-dm rms level for 24h processing and seem highly capable for the subsequent excess phase computation. Moreover, the desired accuracy thresholds of < 5 cm and < 0.05 mm/s rms were met for the validation with data provided by CODE, JPL and EUMETSAT. The comparisons with UCAR show bigger rms values. Possible reasons for this could be a less optimized processing strategy or different input models at UCAR. Furthermore, UCAR and EUMETSAT use different MetOp-A antenna offsets within their processing. This inconsistency leads to errors either in UCAR or EUMETSAT orbit products. In order to achieve a high quality of the orbit data, several general conditions with regard to correct instrument settings, input data, force models, pseudo-stochastic parameters and data screening have to be considered correctly within the LEO processing.

Manifold investigations have been carried out throughout this research. It could be shown that the observation data sampling of 10 seconds is sufficient for LEO orbits except for the FORMOSAT-3/COSMIC mission. This mission is strongly affected by additional input data and originally collecting GNSS measurements with 1 second sampling rate. Hence, the original sampling rate is recommended.

For the pseudo-stochastic parameters, three different sets of samplings have been investigated (3 minutes sampling, 6 minutes sampling and 12 minutes sampling). It turned out best to keep the 6 minutes set as advised by literature. An increasing number of parameters with 3 minutes does not lead to significant orbit improvements but is costly from a computational point of view.

The edge effects caused by different processing period lengths (24h arcs, or somewhat more) can be clearly identified in the achieved results. Nevertheless, this effect is small and limited to the transition boundaries of the processed days. A

special preparation of the GNSS input data is necessary to ensure correct results, these efforts do not seem justified. Hence, a straight forward 24h day-by-day processing is recommended, at least for fast track processing (on follow-on day of observations). Time delayed post-processing or re-processing might opt for the additional efforts.

The investigations concerning different clock correction data of 5s or 30s lead to small differences in the computed LEO positions and velocities. From a computational point of view, the use of the 5s high-rate clock corrections is not costly but these corrections are only provided by CODE. Comparing the IGS and CODE final GNSS input data and their impact on the computed LEO positions and velocities, this impact is small and the differences are on the one-centimeter level. This means: it is possible to use the CODE input data, including the 5s clock estimates, instead of the official IGS products if the traceability of the used input data can be guaranteed for the purpose of climate research. (e.g. cross-verification of CODE input with IGS input)

During this study, also some ideas for quantifying the orbit uncertainty have been collected. This challenging task is driven by the lack of uncertainty information for the orbit data needed for the excess phase processing. In chapter 6, some ideas are presented in theory. Furthermore, for a practical approach of the uncertainty separation it turned out that the effect of the receiver noise and tracking is rather low compared to the impact of different GNSS input data which is on the cm level.

The results from the GNSS-RO orbit arc comparisons during example occultation events show a good agreement to the reference data provided by UCAR. As expected, the differences show a almost constant behavior during the short duration of occultation events. The GNSS-RO arc differences computed in the inertial true-of-date system are in a similar range as the Earth-fixed LEO orbits. Some space for improvements is given due to the fact, that the exact input models and settings for the true-of-date transformation are not yet known.

In summary, the developed processing strategy is highly capable for the precise orbit determination of LEO satellites. The used Bernese GNSS software is a comprehensive and powerful tool for this application. The achieved results provide a perfect basis for further implementation in the orbit and excess phase processing chain of the new rOPS at the Wegener Center for Climate and Global Change.

List of Figures

List of Tables

Bibliography

Ashby N, Spilker JJ (1996) Introduction to relativistic effects on the global positioning system. Global Positioning System: Theory and applications 1(18):623–697

Bar-Sever Y (1995) A New model for GPS yaw attitude. Journal of Geodesy 70(11):714–723, DOI 10.1007/BF00867149

Baur O, Bock H, Hoeck E, Jäggi A, Krauss S, Mayer-Gürr T, Reubelt T, Siemes C, Zehentner N (2014) Comparison of GOCE-GPS gravity fields derived by different approaches. Journal of Geodesy pp 1–15, DOI 10.1007/s00190-014-0736-6

Beutler G (1990) Numerische Integration gewöhnlicher Differentialgleichungssysteme: Prinzipien und Algorithmen. Mitteilungen der Satelliten-Beobachtungsstation Zimmerwald Nr:23, AIUB, Bern, Switzerland

Beutler G (2005) Methods of Celestial Mechanics, vol 1. Springer Verlag Berlin Heidelberg New York, DOI 10.1007/978-3-540-26870-3

Beutler G, Brockmann E, Gurtner W, Hugentobler U, Mervart L, Rothacher M, Verdun A (1994) Extended orbit modeling techniques at the CODE processing center of the international GPS service for geodynamics (IGS): Theory and initial results. Manuscripta Geodaetica 19(6):367–386

Beutler G, Jäggi A, Hugentobler U, Mervart L (2006) Efficient satellite orbit modelling using pseudo-stochastic parameters. Journal of Geodesy 80:353–372, DOI 10.1007/s00190-006-0072-6

Beyerle G, Schmidt T, Michalak G, Heise S, Wickert J, Reigber C (2005) GPS radio occultation with GRACE: Atmospheric profiling utilizing the zero-difference technique. Geophysical Research Letters 32(13), DOI 10.1029/2005GL023109

Bock H (2003) Efficient Methods for Determining Precise Orbits of Low Earth Orbiters using the Global Positioning System. PhD thesis, University Bern - AIUB, Bern, Switzerland, URL `www.sgc.ethz.ch/sgc-volumes/sgk-65.pdf`

Bock H (2012) The LEOPOD.PCV information file. University Bern - AIUB, Bern, Switzerland

Bock H, Hugentobler U, Jaeggi A, Beutler G (2005) Precise orbit determination for champ using an efficient kinematic and reduced-dynamic procedure. In: Reigber C, Luehr H, Schwintzer P, Wickert J (eds) Earth Observation with CHAMP, Springer Berlin Heidelberg, pp 157–162, DOI 10.1007/3-540-26800-6_25

Byun SH (2003) Satellite orbit determination using triple-differenced GPS carrier phase in pure kinematic mode. Journal of Geodesy 76:569–585, DOI 10.1007/s00190-002-0279-0

Case K, Kruizinga G, Wu S (2002) Grace level 1b data product user handbook. JPL Publication D-22027, Pasadena, CA, USA

CCSDS S (2010) Navigation Data-Definitions and Conventions. Report Concerning Space Data System Standards CCSDS 5000-G-2 Green Book Issue 3 Washington, DC, USA URL `http://www.ccsds.org`

Dach R, Hugentobler U, Fridez P, Meindl M (2007) Bernese GPS software version 5.0. User manual. University of Bern - AIUB, Bern, Switzerland

Dach R, Brockmann E, Schaer S, Beutler G, Meindl M, Prange L, Bock H, Jäggi A, Ostini L (2009) GNSS processing at CODE: status report. Journal of Geodesy 83(3-4):353–365, DOI 10.1007/s00190-008-0281-2

Dach R, Hugentobler U, Fridez P, Meindl M (2013) Bernese GNSS software: New features in version 5.2. Presentation, University of Bern - AIUB, Bern, Switzerland

Dow JM, Neilan RE, Gendt G (2005) The International GPS Service: Celebrating the 10th anniversary and looking to the next decade. In: Advances in Space Research, vol 36, pp 320–326, DOI 10.1016/j.asr.2005.05.125

Dow JM, Neilan RE, Rizos C (2009) The International GNSS Service in a changing landscape of Global Navigation Satellite Systems. Journal of Geodesy 83(3-4):191–198, DOI 10.1007/s00190-008-0300-3

Dunn C, Bertiger W, Bar-Sever Y, Desai S, Haines B, Kuang D, Franklin G, Harris I, Kruizinga G, Meehan T, Nandi S, Nguyen D, Rogstad T, Thomas JB, Tien

J, Romans L, Watkins M, Wu SC, Bettadpur S, Kim J (2003) Instrument of Grace: GPS augments gravity measurements. GPS World 14(2):16–28

Feltens J (1991) Nicht-gravitative Störeinflüsse bei der Modellierung von GPS-Erdumlaufbahnen. Deutsche Geodätische Kommission, Bayerische Akademie der Wissenschaften, Reihe C, Vol:371

Ge M, Gendt G, Rothacher M, Shi C, Liu J (2007) Resolution of GPS carrier-phase ambiguities in Precise Point Positioning (PPP) with daily observations. Journal of Geodesy 82(7):389–399, DOI 10.1007/s00190-007-0187-4

Ge M, Chen J, Douša J, Gendt G, Wickert J (2011) A computationally efficient approach for estimating high-rate satellite clock corrections in realtime. GPS Solutions 16(1):9–17, DOI 10.1007/s10291-011-0206-z

Gerlach C, Földvary L, Svehla D, Gruber T, Wermuth M, Sneeuw N, Frommknecht B, Oberndorfer H, Peters T, Rothacher M, Rummel R, Steigenberger P (2003) A CHAMP-only gravity field model from kinematic orbits using the energy integral. Geophysical Research Letters 30(20), DOI 10.1029/2003GL018025

Gill E, Montenbruck O (2004) Comparison of GPS-based Orbit Determination Strategies. Proceedings of the 18th International Symposium on Space Flight Dynamics (ESA SP-548) p169, German Space Operations Center of DLR and the European Space Operations Centre of ESA 11-15 October 2004, Munich, Germany

Griffiths J, Ray JR (2009) On the precision and accuracy of IGS orbits. Journal of Geodesy 83:277–287, DOI 10.1007/s00190-008-0237-6

Gurtner W, Estey L (2007) RINEX-The Receiver Independent Exchange Format-Version 3.00. Astronomical Institute, University of Bern and UNAVCO, Boulder, Colorado, USA

Hajj GA, Romans LJ (1998) Ionospheric electron density profiles obtained with the Global Positioning System: Results from the GPS/MET experiment. Radio Science 33(1):175–190, DOI 10.1029/97RS03183

Hajj GA, Kursinski ER, Romans LJ, Bertiger WI, Leroy SS (2002) A technical description at atmospheric sounding by GPS occultation. Journal of Atmospheric and Solar-Terrestrial Physics 64:451–469, DOI 10.1016/S1364-6826(01)00114-6

Hilla S (2010) The Extended Standard Product 3 Orbit Format (SP3-c). National Geodetic Survey, National Ocean Service, NOAA, Silver Spring, MD 20910-6233, USA URL `http://igscb.jpl.nasa.gov/igscb/data/format/sp3_docu.txt`

Hofmann-Wellenhof B, Lichtenegger H, Wasle E (2008) GNSS - Global Navigation Satellite Systems: GPS, GLONASS, Galileo, and more. Springer Wien New York, ISBN 978-3-211-73012-6, URL `http://www.springer.com/gp/book/9783211730126`

Hu X, Zeng Z, Zhang XX, Zhang DY, Xiao CY (2005) Atmospheric inversion methods of gps radio occultation. Chinese Journal of Geophysics 48(4):845–853, DOI 10.1002/cjg2.722

Hugentobler U, Ineichen D, Beutler G (2003) GPS satellites: Radiation pressure, attitude and resonance. Advances in Space Research 31(8):1917–1926, DOI 10.1016/S0273-1177(03)00174-1

Hugentobler U, Schaer S, Beutler G, Bock H, Dach R, Jäggi A, Meindl M, Urschl C, Mervart L, Rothacher M, Wild U, Wiget A, Brockmann E, Ineichen D, Weber G, Habrich H, Boucher C (2004) CODE IGS Analysis Center Technical Report 2002. In: IGS 2001-2002 Technical Reports, IGS Central Bureau, pp 43–51, JPL, CA, USA, URL `http://igscb.jpl.nasa.gov/igscb/resource/pubs/0102TR/2-an_ctrs-2.pdf`

Hwang C, Tseng TP, Lin T, Svehla D, Schreiner B (2009) Precise orbit determination for the FORMOSAT-3/COSMIC satellite mission using GPS. Journal of Geodesy 83(5):477–489, DOI 10.1007/s00190-008-0256-3

Jäggi A (2007) Pseudo-Stochastic Orbit Modeling of Low Earth Satellites Using the Global Positioning System. PhD thesis, University Bern - AIUB, Bern, Switzerland, URL `http://www.sgc.ethz.ch/sgc-volumes/sgk-73.pdf`

Jäggi A, Beutler G, Hugentobler U (2005) Efficient Stochastic Orbit Modeling Techniques using Least Squares Estimators. In: Sanso F (ed) A Window on the Future of Geodesy, International Association of Geodesy Symposia, vol 128, Springer Berlin Heidelberg, pp 175–180, DOI 10.1007/3-540-27432-4_31

Jäggi A, Hugentobler U, Beutler G (2006) Pseudo-Stochastic Orbit Modeling Techniques for Low-Earth Orbiters. Journal of Geodesy 80(1):47–60, DOI 10.1007/s00190-006-0029-9

Jäggi A, Dach R, Montenbruck O, Hugentobler U, Bock H, Beutler G (2009) Phase center modeling for LEO GPS receiver antennas and its impact on precise orbit determination. Journal of Geodesy 83(12):1145–1162, DOI 10.1007/s00190-009-0333-2

Jazwinski A (1970) Stochastic Processes and Filtering Theories, vol 1, Academic Press, New York, USA, ISBN 978-0-486-46274-5

Jorgensen JL (1999) In Orbit Performance of a fully Autonomous Star Tracker. In: Spacecraft Guidance, Navigation and Control Systems, Proceedings of the 4th ESA International Conference, held 18-21 October, 1999 in ESTEC, Noordwijk, the Netherlands. Edited by B. Schuermann. ESA SP-425. Paris: European Space Agency, 2000., p.103-110

Kang Z, Tapley B, Ries J, Bettadpur S, Nagel P (2007) Impact of GPS satellite antenna offsets on GPS-based precise orbit determination. Advances in Space Research 39(10):1524–1530, DOI 10.1016/j.asr.2006.11.003

Kirchengast G, Schwärz M, Fritzer J, Schwarz J, Scherllin-Pirscher B, Steiner A (2013) Reference Occultation Processing System (rOPS) for Cal/Val and Climate: Towards SI-tied Atmospheric Profiling with Integrated Uncertainty Propagation. Presentation given at OPAC-IROWG 2013 International Workshop, Seggau Castle, Leibnitz, Austria

Klaes KD, Cohen M, Buhler Y, Schlüssel P, Munro R, Engeln A, Clérigh E, Bonekamp H, Ackermann J, Schmetz J, Luntama JP (2007) An Introduction to the EUMETSAT Polar system. Bulletin of the American Meteorological Society 88:1085–1096, DOI 10.1175/BAMS-88-7-1085

Kroes R (2006) Precise Relative Positioning of Formation Flying Spacecraft using GPS. PhD thesis, University Delft, Delft, Netherlands, URL `http://repository.tudelft.nl`

Kroes R, Montenbruck O, Bertiger W, Visser P (2005) Precise GRACE baseline determination using GPS. GPS Solutions 9:21–31, DOI 10.1007/s10291-004-0123-5

Kuang D, Bar-Sever Y, Bertiger W, Desai S, Haines B, Iijima B, Kruizinga G, Meehan T, Romans L (2001) Precise Orbit Determination for CHAMP Using

GPS Data from BlackJack Receiver. Presented at the ION National Technical Meeting, Session E1: Scientific Applications Timing, and Frequency, Long Beach, CA, USA

Kursinski ER, Hajj GA, Bertiger WI, Leroy SS, Meehan TK, Romans LJ, Schofield JT, McCleese DJ, Melbourne WG, Thornton CL, Yunck TP, Eyre JR, Nagatani RN (1996) Initial Results of Radio Occultation Observations of Earth's Atmosphere Using the Global Positioning System. Science 271:1107–1110, DOI 10.1126/science.271.5252.1107

Kursinski ER, Kursinski ER, Hajj GA, Hajj GA, Schofield JT, Schofield JT, Linfield RP, Hardy KR, Hardy KR (1997) Observing Earth's atmosphere with radio occultation measurements using the Global Positioning System. Journal of Geophysical Research 102:23.429–23.465, DOI 10.1029/97JD01569

Kursinski ER, Hajj GA, Leroy SS, Herman BM (2000) The GPS radio occultation technique. Journal of Terrestrial, Atmospheric and Oceanic Sciences 11(1):53–114, URL `http://tao.cgu.org.tw/pdf/v111p053.pdf`

Lackner B, Steiner AK, Hegerl G, Kirchengast G (2011) Atmospheric Climate Change Detection by Radio Occultation Data Using a Fingerprinting Method. Journal of Climate 24:5275–5291, DOI doi:10.1175/2011JCLI3966.1

Leick A (2003) GPS Satellite Surveying. John Wiley and Sons, 3rd edition, New York, USA, ISBN 978-0471059301

Loiselet M, Stricker N, Menard Y, Luntama J (2000) GRAS-MetOp's GPS-based atmospheric sounder. In: ESA Bulletin, vol 102, pp 38–44

Luo X (2012) GPS Stochastic Modelling - Signal Quality Measures and ARMA Processes. Springer-Verlag Berlin Heidelberg, ISBN 978-3-642-34835-8

Mayer-Gürr T (2006) Gravitationsfeldbestimmung aus der Analyse kurzer Bahnbögen am Beispiel der Satellitenmissionen CHAMP und GRACE. PhD thesis, Universität Bonn, Bonn, Germany, URL `http://hss.ulb.uni-bonn.de/2006/0904/0904.pdf`

Mayer-Gürr T, Kurtenbach E, Eicker A (2012a) Different representations of the time variable gravity field to reduce the aliasing problem in grace data analysis. In: Sneeuw N, Novak P, Crespi M, Sanso F (eds) VII Hotine-Marussi Symposium

on Mathematical Geodesy, International Association of Geodesy Symposia, vol 137, Springer Berlin Heidelberg, pp 285–290, DOI 10.1007/978-3-642-22078-4_43

Mayer-Gürr T, Rieser D, Hoeck E, Brockmann J, Schuh W, Krasbutter I, Kusche J, Maier A, Krauss S, Hausleitner W, Baur O, Jaeggi A, Meyer U, Prange L, Pail R, Fecher T, Gruber T (2012b) The new combined satellite only model GOCO03s. Presentation given at the International Symposium on Gravity, Geoid and Height Systems GGHS 2012, Venice, Italy

McCarthy DD, Petit G (2004) IERS Conventions (2003). IERS Technical Note No. 32, International Earth Rotation and Reference Systems Service, ISBN 3-89888-884-3

Montenbruck O (2003a) GNSS Receivers for Space Applications. Presentation given at: ACES and Future GNSS-Based Earth Observation and Navigation, Munich, Germany URL `http://www.iapg.bgu.tum.de`

Montenbruck O, Gill E (2000) Satellite orbits : models, methods, and applications, 1st edn. Springer Heidelberg New York, ISBN 978-3-540-67280-7

Montenbruck O, Kroes R (2003) In-flight performance analysis of the CHAMP BlackJack GPS Receiver. GPS Solutions 7(2):74–86, DOI 10.1007/s10291-003-0055-5

Montenbruck O, Van Helleputte T, Kroes R, Gill E (2005) Reduced dynamic orbit determination using GPS code and carrier measurements. Aerospace Science and Technology 9:261–271, DOI 10.1016/j.ast.2005.01.003

Montenbruck O, Garcia-Fernandez M, Williams J (2006) Performance comparison of semicodeless GPS receivers for LEO satellites. GPS Solutions 10:249–261, DOI 10.1007/s10291-006-0025-9

Montenbruck O, Andres Y, Bock H, van Helleputte T, van den Ijssel J, Loiselet M, Marquardt C, Silvestrin P, Visser P, Yoon Y (2008) Tracking and orbit determination performance of the GRAS instrument on MetOp-A. GPS Solutions 12(4):289–299, DOI 10.1007/s10291-008-0091-2

Pavlis NK, Holmes SA, Kenyon SC, Factor JK (2008) An Earth Gravitational Model to Degree 2160: EGM2008. Presented at the 2008 General Assembly of the European Geosciences Union, Vienna, Austria, April 13-18

Prange L (2010) Global gravity field determination using the GPS measurements made onboard the low Earth orbiting satellite CHAMP. PhD thesis, University Bern - AIUB, Bern, Switzerland, URL `http://www.sgc.ethz.ch/sgc-volumes/sgk-81.pdf`

Ramos-Bosch P (2008) Improvements in autonomous GPS navigation of Low Earth Satellites. PhD thesis, Universitat Politecnica de Catalunya, Catalunya, Spain, URL `http://global.tesisenred.net/handle/10803/7019`

Ray J, Gurtner W (2010) RINEX Extensions to Handle Clock Information. JPL,Pasadena, CA, USA URL `ftp://igscb.jpl.nasa.gov/igscb/data/format/rinex_clock.txt`

Reigber C, Barthelmes F, Greiner-Mai H, Gruber T, Jochmann H, Wünsch J (1999) Temporal gravity field variations from oceanic, atmospheric and inner core mass redistributions and their sensitivity to new gravity missions CHAMP and GRACE. Bollettino di Geofisica Teorica ed Applicata 40(3-4):329–340, URL `http://www2.ogs.trieste.it/bgta/provapage.php?id_articolo=263`

Reigber C, Lühr H, Schwintzer P (2002) Champ mission status. Advances in Space Research 30(2):129–134, DOI 10.1016/S0273-1177(02)00276-4

Reubelt T (2009) Harmonische Gravitationsfeldanalyse aus GPS-vermessenen kinematischen Bahnen niedrig fliegender Satelliten vom Typ CHAMP, GRACE und GOCE mit einem hoch auflösenden Beschleunigungsansatz. PhD thesis, Universität Stuttgart, Stuttgart, Germany, URL `http://elib.uni-stuttgart.de/opus/volltexte/2009/3925`

Rocken C, Anthes R, Exner M, Hunt D, Sokolovskiy S, Ware R, Gorbunov M, Schreiner W, Feng D, Herman B, Kuo YH, Zou X (1997) Analysis and validation of gps/met data in the neutral atmosphere. Journal of Geophysical Research 102(D25):29,849–29,866, DOI 10.1029/97JD02400

Rocken C, Sokolovskiy A, Schreiner B, Hunt D, Ho B, Kuo B, Foelsche U (2009) Climate Monitoring with Radio Occultation Data: Systematic Error Sources. Workshop on the Application of GPS Radio Occultation to Climate, Boulder, CO, USA

Rockwell IC (1984) GPS Interface Control Document. ICD-GPS-200, Satellite Systems Division, El Segundo, CA, USA

Schreiner B, Rocken C, Sokolovskiy S, Hunt D (2010a) Quality assessment of COSMIC/FORMOSAT-3 GPS radio occultation data derived from single- and double-difference atmospheric excess phase processing. GPS Solutions 14(1):13–22, DOI 10.1007/s10291-009-0132-5

Schreiner B, Rocken C, Sokolovskiy S, Hunt D, Kuo B (2010b) GPS-RO processing from raw phase and amplitude to bending angle. Presentation given at OPAC 2010, Graz, Austria URL `http://www.uni-graz.at/opac2010/pdf_presentation/opac_2010_schreiner_bill_presentation63.pdf`

Schreiner B, Rocken C, Sokolovskiy S, Hunt D, Kuo B (2013) COSMIC Data Analysis and Archive Center (CDAAC) Overview and Status. Presentation given at OPAC-IROWG 2013 International Workshop, Seggau Castle, Leibnitz, Austria

Seeber G (2003) Satellite Geodesy: foundations, methods, and applications. Walter de Gruyter, Berlin, New York, DOI 10.1515/9783110200089

Steiner A, Kirchengast G, Ladreiter H (1999) Inversion, error analysis, and validation of GPS/MET occultation data. Annales Geophysicae 17(1):122–138, DOI 10.1007/s00585-999-0122-5

Steiner AK, Lackner BC, Ladstädter F, Scherllin-Pirscher B, Foelsche U, Kirchengast G (2011) GPS radio occultation for climate monitoring and change detection. Radio Science 46(6), DOI 10.1029/2010RS004614

Steiner AK, Hunt D, Ho SP, Kirchengast G, Mannucci AJ, Scherllin-Pirscher B, Gleisner H, von Engeln A, Schmidt T, Ao C, Leroy SS, Kursinski ER, Foelsche U, Gorbunov M, Heise S, Kuo YH, Lauritsen KB, Marquardt C, Rocken C, Schreiner W, Sokolovskiy S, Syndergaard S, Wickert J (2013) Quantification of structural uncertainty in climate data records from GPS radio occultation. Atmospheric Chemistry and Physics 13(3):1469–1484, DOI 10.5194/acp-13-1469-2013

Svehla D, Rothacher M (2005) Kinematic precise orbit determination for gravity field determination. In: Window on the Future of Geodesy, vol 128, pp 181–188, DOI 10.1007/3-540-27432-4_32

Swatschina P (2012) Dynamic and Reduced-Dynamic Precise Orbit Determination of Satellites in Low Earth Orbits. PhD thesis, Vienna University of Technology,

Vienna, Austria, URL `http://publik.tuwien.ac.at/files/PubDat_219297.pdf`

Syndergaard S (1998) Modeling the impact of the Earth's oblateness on the retrieval of temperature and pressure profiles from limb sounding. Journal of Atmospheric and Solar-Terrestrial Physics 60(2):171–180, DOI http://dx.doi.org/10.1016/S1364-6826(97)00056-4

Tapley BD (2004) The gravity recovery and climate experiment: Mission overview and early results. Geophysical Research Letters 31(9), DOI 10.1029/2004GL019920

Tapley BD, Reigber C (2001) The GRACE Mission: Status and future plans. EOS Transactions 82(47), AGU Fall Meeting , G41 C-02, University of Texas at Austin Center for Space Research, Austin, TX, USA

Vallado DA (2007) Fundamentals of Astrodynamics and Applications. Space Technology Library, Springer, NY, USA, ISBN 0-387-71831-1

Ware R, Rocken C, Solheim F, Exner M, Schreiner W, Anthes R, Feng D, Herman B, Gorbunov M, Sokolovskiy S, Hardy K, Kuo Y, Zou X, Trenberth K, Meehan T, Melbourne W, Businger S (1996) GPS Sounding of the Atmosphere from Low Earth Orbit: Preliminary Results. Bulletin of the American Meteorological Society 77:19–40, DOI 10.1175/1520-0477(1996)077<0019:GSOTAF>2.0.CO;2

Wickert J, Beyerle G, König R, Heise S, Grunwaldt L, Michalak G, Reigber C, Schmidt T (2005) GPS radio occultation with CHAMP and GRACE: A first look at a new and promising satellite configuration for global atmospheric sounding. Annales Geophysicae 23:653–658, DOI 10.5194/angeo-23-653-2005

Woo KT (1999) Optimum Semi-Codeless Carrier Phase Tracking of L2. Journal of the Institute of Navigation, Institute of Navigation, 47:82–99, URL `http://www.bmotion.com/navcom/images/tech_archiv/L2_Phase_Tracking.pdf`

Wu BH, Chu V, Chen P, Ting T (2005) FORMOSAT-3/COSMIC science mission update. GPS solutions 9(2):111–121, DOI 10.1007/s10291-005-0140-z

Wu JT, Yunck TP, Thornton CL (1991) Reduced-dynamic technique for precise orbit determination of low earth satellites. Journal of Guidance, Control, and Dynamics 14:24–30, DOI 10.2514/3.20600

Wu JT, Wu SC, Hajj GA, Bertiger WI, Lichten SM (1993) Effects of antenna orientation on GPS carrier phase. Manuscripta Geodaetica 18:91–98, JPL, Pasadena, CA, USA

Wübbena G, Schmitz M, Menge F, Seeber G, Völksen C (1996) A new approach for field calibration of absolute gps antenna phase center variations. Navigation, Journal of the Institute of Navigation 44(2):247–255, DOI 10.1002/j.2161-4296.1997.tb02346.x

Zehentner N, Mayer-Gürr T (2013) Kinematic orbits for GRACE and GOCE based on raw GPS observations. In: Poster presented at the IAG Scientific Assembly 2013, Potsdam, Germany

Zhang K, Zhang S, LeMarshall J, Kirchengast G, Norman R, Li Y, Liu C, Carter B (2013) A new Australian GNSS radio occultation data processing platform. In: in A. Kealy (ed.) International Symposium on Global Navigation Satellite Systems 2013, Tweed Heads, Australia, 16-18 July 2013, pp 1–12, URL `http://researchbank.rmit.edu.au/view/rmit:23742`